THE UNIVERSITY OF OKLAHOMA

GRADUATE COLLEGE

EFFECTS OF ELECTROSTATIC FIELD ON MIXED CONVECTION IN VERTICAL CHANNEL FLOWS

A THESIS

SUBMITTED TO THE GRADUATE FACULTY

in partial fulfillment of the requirements for the degree
of

MASTER OF SCIENCE

By

SATISH S. KULKARNI

Norman, Oklahoma

1994

UNIVERSITY OF OKLAHOMA
LIBRARIES

OU
THESIS
KUL
cop. 2

EFFECTS OF ELECTROSTATIC FIELD ON MIXED CONVECTION IN VERTICAL CHANNEL FLOWS

A THESIS

APPROVED FOR

THE SCHOOL OF AEROSPACE AND MECHANICAL ENGINEERING

© Copyright by Satish S. Kulkarni 1994

All Rights Reserved

ACKNOWLEDGEMENTS

I would like to thank my advisor, Dr. Feng-Chyuan Lai, for his valuable guidance throughout my Master's program. His incessant help, numerous suggestions and discussions were the major factor for the successful completion of this thesis. I am indebted and have deep appreciation to him. I am thankful to Dr. Cengiz M. Altan, for his contribution to this research work, and Dr. William H. Sutton for the suggestions and discussions towards this thesis as committee members.

I am also thankful to Mr. Michael D. Tuttle, Cray Research Inc., though I have not had an opportunity to talk to him, without whose help and Cray machines this work would have been incomplete. Special thanks to my friends for being constant source of encouragement and help during my masters program. Thank you all.

Finally, all the motivation for this work and the program comes from my parents, brothers and sisters. Their constant support and encouragement throughout my life have been a source of inspiration in taking up this program and making my stay memorable at the University of Oklahoma. I also take this opportunity to thank my brother, Subhash, for his concern and affection shown at all moments of my life. I am grateful to my family forever.

TABLE OF CONTENTS

LIST OF FIGURES

LIST OF TABLES

NOMENCLATURE

A	plate area, [m^2]
b	ion mobility of the fluid, [$m^2/V \cdot s$]
d	distance between wire and plate, [m]
D_h	hydraulic diameter, [m]
E	electric field, [V/m]
E_x	electric field strength in x-direction, [V/m]
E_y	electric field strength in y-direction, [V/m]
Gr	Grashoff number, $g\beta(T_i - T_w)d^3 / \nu^2$
h	convective heat transfer coefficient, [$W/m^2 \cdot s$]
I	total electric current, [A]
J	current density, [A/m^2]
k	thermal conductivity of fluid, [$W/m \cdot s$]
L	length of channel, [m]
L^*	dimensionless length of channel
L_w	length of wire, [m]
Nu	local Nusselt number, hD_h/k

$\overline{Nu}$	average Nusselt number, $\bar{h}D_h$ / k
p	pressure, [Pa]
Pe	Peclet number, u_e d / α
Pr	Prandtl number, ν / α
r_o	radius of wire, [m]
Re	flow Reynolds number, u_o d / ν
Re_{ehd}	EHD Reynolds number, u_e d / ν
S_x	distance between wire and end of channel, [m]
S_y	distance between wire and plate, [m]
t	time, [s]
$\bar{t}$	dimensionless time, $u_e t$ / d
T	temperature, [K]
T_i	inlet gas temperature, [K]
T_w	wall temperature, [K]
u	velocity in x-direction, [m/s]
u_e	characteristic velocity of ionic wind, [m/s]
uo	uniform velocity at the inlet, [m/s]
v	velocity in y-direction, [m/s]
V	electric potential, [V]

$\overline{V}$	normalized electrical potential, V/V_o
V_o	electric potential at the wire, [V]
x,y	Cartesian coordinates, [m]
$\overline{x},\overline{y}$	dimensionless Cartesian coordinates
α	thermal diffussivity, [m^2/s]
β	coefficient of thermal expansion, [1/K]
ϵ_o	permitivity of free space, [F/m]
ν	kinematic viscosity of fluid, [m^2/s]
ρ	fluid density, [kg/m^3]
ρ_c	ionic space charge density, [C/m^3]
$\overline{\rho}_c$	dimensionless space charge density, ρ_c / ρ_{co}
ρ_{co}	ionic space charge density at the wire, [C/m^3]
ψ	stream function, [1/s]
$\overline{\psi}$	dimensionless stream function, $\psi / u_e d$
ω	vorticity, [1/s]
$\overline{\omega}$	dimensionless vorticity, $d \omega / u_e$

θ	dimensionless temperature, $(T - T_w) / (T_i - T_w)$
θ_i	dimensionless mean inlet gas temperature
θ_w	dimensionless wall temperature
θ_o	dimensionless mean outlet gas temperature

ABSTRACT

In recent years, the application of electrostatic field to enhance the heat transfer has been one of the areas of interest. In this thesis, an attempt has been made to study laminar mixed convection under the influence of electrostatic field in a wire-plate vertical channel.

The electrostatic field and space charge density distribution are obtained by solving Maxwells equation, current continuity equation and Ohm's law simultaneously. The numerical models by Yamamoto and Kallio for calculating the electric field and space charge distribution are evaluated. Comparisons of the outputs from both models for one-wire and two-wire channels show good agreement. For Kallio's model, lack of symmetry in the distribution of electric field is the main reason for not being adopted in the analysis of fluid flow and heat transfer. The electric field and space charge density distribution are thus based on Yamamoto's model. The results are then used in the calculation of electric body forces which, along with the thermal buoyancy, are included in the Navier-Stokes equations. The numerical solution for mixed convection involves computation of vorticity transport and energy equations. Studies are performed for the simultaneously developing flows in a vertical channel. The flow Reynolds numbers considered are 600, 1200 and 1800 with Grashoff numbers varying from 10^4 to 10^6 for both aiding and

opposing flows.

It is observed that due to the existence of secondary flows, a combined effect from the electric field and thermal buoyancy, there is an improvement in the heat transfer for Grashoff number up to 10^5 in the case of aiding flow. For opposing flows, the heat transfer increases in all the cases of Reynolds and Grashoff numbers. Oscillation in the flow field has been observed for aiding flows at Re = 600 and 1200 due to the interaction of electric, inertial and buoyancy forces in the channel. The flow field tends to stabilize if the Reynolds or Grashoff number are increased. Due to the domination of the flow inertia at Re = 1800, no oscillation has been observed.

CHAPTER 1

INTRODUCTION

1.1 Applications of Electrohydrodynamics in Industries

Electrohydrodynamics (EHD) refers to the coupling of an electric field and flow field in a dielectric fluid. Applications of EHD in industries have been followed since long to improve the process involved. Two major areas of interest are the enhancement of heat transfer and electrostatic precipitation. The principles underlined in these two major applications are discussed in the next section, followed by the literature review in each specific area.

1.1.1 Enhancement of Heat Transfer

Various studies show that the application of an electrostatic potential to a dielectric fluid flowing in a duct can improve the rate of heat exchange between the duct wall and the fluid. The subject of enhanced heat transfer is of serious interest for heat exchanger application since this provides increased process efficiency and yields a saving of operating costs. Enhancement techniques utilizing an electric field, which are based on the electrostatic forces due to space-charge and/or polarization of a dielectric fluid, are one of the most promising methods because of quick response to the control of the flow, increased heat transfer rates and small consumption of electric power.

In rectangular channels, corona discharge from longitudinal or transverse wire electrodes is spatially nonuniform due to the geometry of the electrode configuration. A uniform discharge along the wire results in an electrically induced flow modification. Past experimental and theoretical studies in this geometry have centered on the hydrodynamic process which results from the presence of the discharge in an otherwise well-understood flow field. The corona-discharge interaction with the bulk flow can result in circulation zones in the vicinity of the discharge wires and substantially increases the free-stream turbulence and diffusivity levels. The enhancement of heat transfer is directly related to the circulatory secondary flow thus generated. This kind of phenomenon also finds its application in industrial electrostatic precipitators (ESP).

1.1.2 Electrostatic Precipitation

Electrostatic precipitation is a process of removing the suspended particles in the form of dust, fumes and smoke from a gas stream. This process is widely used in building electrostatic precipitators, which play a major role in pollution control in industrial applications such as coal fired power generation plants, steel production, cement production and chemical processing, etc. Among the widely used ESP design is the wire-plate model.

A wire-plate precipitator generally consists of a series of grounded parallel plates with equally spaced wire electrodes at high potential located at the center-line. The basic process of electrostatic precipitation involves local ionization of gas known

as corona, which is observed as a glow around the wire electrode due to the application of a high DC voltage. The unipolar ions generated in the corona tend to drift away from the wire electrode in the direction of decreasing field strength. The particles in the hot gas flowing through the ESP channel acquire charge due to the collision with the drifting unipolar ions. The charged particles migrate towards the grounded collecting plates under the influence of applied electrostatic field force known as the coulomb force. In the process of collection in an ESP, the motion of the particulate is affected by both electrostatic field and fluid forces. The corona generated ions that collide at high velocity with neutral gas molecules residing in the space between the discharge electrode and collecting plate result in a secondary flow known as electric wind (ionic wind or corona wind). After deposited on the plates, the particles are further collected in a hopper at the bottom of the ESP by mechanical rapping of the plates.

1.2 Literature Review

Most studies in the field of EHD have been focused on the interaction of the electric field, flow field and temperature field for a dielectric fluid flow. Although literature emphasized on different applications e.g., enhancement of heat transfer with applications to the heat exchanger design and effects of corona wind on the performance of electrostatic precipitators, are available, it is important to note that no generalized correlations of heat transfer and fluid flow for forced and free convection with electric fields are available [3]. The intricate interactions of electric

field, flow field and heat transfer together have imposed limitations on both experimental and mathematical studies.

1.2.1 Enhancement of Heat Transfer using Electric Field

Studies in the area of enhancement of convection heat transfer have been conducted with a goal to improve the performance of a heat exchanger for more efficient utilization of energy, possible reduction of power consumption.

Velkoff and Miller [27] conducted experimental study in their single wire-plate setup on the effects of heat transfer by the application of electrostatic field. They used Freon as the working fluid and condensation of the Freon vapor was produced on a cooled vertical copper plate enclosed in a chamber. A significant increase in the mean heat transfer coefficient in the condensation process was observed.

Franke [6] was able to double the free convection heat transfer rate from a vertical flat plate by means of corona discharge from properly spaced vertical wire electrodes. It was observed that an increase in the heat transfer rate is accompanied by the production of columnar vortices in the boundary layer.

Sadek et al. [23] investigated the EHD augmentation of drying under forced convection over a horizontal flat plate. The electric forces were applied by placing a high-voltage electrode above the horizontal sponge which was maintained at ground potential. It was concluded from the experimental observations that the augmentation of heat and mass transfer rates is due to ion-drag forces.

Fernandez and Poulter [5] performed experimental studies on an electrohydrodynamically-enhanced oil heater of annular cross-section by application of high DC voltage across the annular gap. The electric field induced a very strong radial motion of the fluid resulting in a heat transfer increase of more than 20 folds over the fully developed laminar flow.

Fujino et al. [7] conducted experiments to study the effect of a uniform DC electric field on laminar forced convective heat transfer with a weakly conducting fluorocarbon refrigerant flowing in a channel confined by parallel plate electrodes. They observed enhancement in heat transfer for low Reynolds number flows. It was concluded that the degree of enhancement can be significantly extended by appreciably adjusting the conductivity of the liquid.

Takimoto et al. [26] conducted theoretical and experimental studies to investigate a forced convective flow interacted with an ionic wind generated by a corona discharge in a wire-plate channel. It was observed that the generation of ionic wind, which disturbs the primary flow at the interval of wire spacing in the flow direction, resembles turbulence promoter. In the theoretical analysis, they considered a two-dimensional horizontal channel consisting of two heated flat plates and a series of wire electrodes with high electric potential equally spaced along the center-line of the channel. The analysis of the electric field with a space charge, and the flow field under the coulomb forces, was performed by using the EHD model presented by Yamamoto and Velkoff [31]. In the vorticity transport equation, the authors did not include thermal buoyancy in the body force terms. The streamlines

obtained for low Reynolds number flows by the numerical calculations were compared to the Schlieren photographs taken in the experimental study. It was seen from the Schlieren photographs that when the flow velocity was under 0.3 m/s, a fluctuating flow was observed upstream of the wire, which was referred to as the hydrodynamically unstable flow induced by the secondary flow. The flow stabilized as the velocity increased. It was concluded that the rate of heat transfer enhancement with increasing total pumping power was larger in the laminar flow region as seen from the experimental results for Re = 1290, and it decreased gradually with an increase in the Reynolds number. This indicated that, the ionic wind enhances heat transfer most efficiently in the laminar flow region from the standpoint of power consumption.

1.2.2 Electrostatic Precipitation

The principle of electrostatic precipitation was adopted for building commercial electrostatic precipitators as early as 1906 as a necessity for separating the particles from the flue gas. Since then electrostatic precipitators have been playing a major role in controlling the industrial pollution.

The Deutsch-Anderson equation has been widely used to predict the precipitator performance, hence for designing the ESPs. The basic assumption in the formulation of Deutsch equation is that the particles are distributed uniformly in any cross-section of the ESP. Empirical corrections to the Deutsch theory have been incorporated to account for non-Deutscian phenomenon such as re-entrainment, gas

sneakage and finite particle mixing. Robinson [22] modified the Deutsch equation by taking into account the non-uniformity of dust concentration.

Chattock [2] was the first to give a qualitative analysis of the electric wind phenomenon. He also presented a relationship between electric wind pressure and corona current. In the early studies no complete analytical solution of the electric wind velocity as found. The reasons were due to the difficulty in establishing the nature of space charge density distribution and the boundary condition at the discharge wire.

Ramadan and Soo [20] numerically solved the laminar, two-dimensional Navier-Stokes equation with electric body force for a constant space charge distribution to yield estimates of the electric wind pattern. Their model predicted the existence of a secondary flow issuing from the corona wire towards the collecting plate in the absence of any inlet flow for positive corona discharge.

Yabe, Mori and Hijikata [29] have experimentally and theoretically analyzed the electric wind for single-wire, single-plate in an open channel geometry for positive corona charge. It was quantitatively made clear that the corona wind is produced by the coulomb force acting on ions. The numerically calculated electric potential distributions were experimentally verified. No fluid flow through the channel was considered but still a circulatory fluid field was observed due to the corona wind in the plane perpendicular to the electrode.

Stock and Crowe [25] numerically predicted the gas flow in a wire-pipe precipitator, including the effects of particle-gas and ion-gas (electric wind)

momentum coupling. Owing to the symmetry of their geometry, the resulting velocity profile was unaffected by the electric wind. They concluded that electric wind effects only arise when there exists asymmetry about the corona wire as in case of wire-plate precipitators.

The interaction of the electric wind with a superimposed inlet velocity was experimentally and theoretically investigated by Yamamoto and Velkoff [31], who used a two-dimensional, laminar flow model for both one-wire and two-wire configurations. The flow interactions of the particle free secondary flow with positive corona discharge were visualized by a Schlieren system and by mist-injected smoke. Theoretical study involved, first, determination of space charge density and the electric field distribution by numerically solving the current continuity and Poisson's equations. In the second part of the numerical calculations, the Navier-Stokes equations expressed in terms of the vorticity and stream function were solved using finite difference method. In their study energy equation was not considered since the effects of heat convection were neglected. It was observed that the existence of the secondary flow was apparent for inlet velocities less than 1.2 m/s at typical corona current densities. The recirculating cells existing at no flow condition disappeared to form a single circulatory cell at location opposite to the wire at a velocity of about 0.6 m/s. Their numerical results were qualitatively consistent with Schlieren flow visualization. In the analysis they used steady-state convergence criterion (i.e., the percentage difference between two consecutive iterations) being 0.0005 for the velocities and stream functions.

Recently, for the laminar electrohydrodynamic flow with a homogeneous positive polarity corona discharge along the wire, an oscillatory flow has been observed in certain situations [12]. This is in contradiction to a steady-state solution which was originally reported for such flows [31]. It is said that the oscillatory flow was overlooked in the analysis because of the convergence criterion adopted earlier.

The experimental work of Yabe et al. [29] and that of Yamamoto and Velkoff [31] were performed using a positive corona discharge. Because a positive corona is inherently more stable and uniform than a negative corona. However, a negative corona is used in most precipitators because it is advantageous in obtaining higher sparkover currents. Since a negative corona depends upon the availability of electrons on the electrode surface, the discharge is spotty and appears as tufts. Neverthless, dust, corrosion and other electrode surface imperfections may cause a non-uniform discharge in either the negative or the positive configuration.

A number of experimental studies have shown that the negative corona results in an increase in the turbulence level of the gas flow and/or secondary flows within an ESP. Leonard, Mitchner and Self [14] , employed Schlieren visualization and laser-anemometry techniques to study the secondary flow turbulence levels for positive and negative corona discharge. They observed that two-dimensional positive corona discharge interacts with the flow of a wire-plate ESP to produce a non-turbulent secondary flow in a plane perpendicular to the discharge wires. The smoke-wire visualization and hot-wire anemometry were employed to show that negative corona discharge non-uniformities are responsible for producing both

secondary flow in a plane parallel to the discharge wire and turbulence. The experiments were performed for single-wire and multi-wire plate precipitators. They concluded that for negative corona the total turbulent energy increased for inlet velocities less than 2 m/s, but appeared to simply smooth the turbulence profile for higher velocities. Positive corona had little effect on the turbulence energy production for inlet velocities greater than 2 m/s but its presence inexplicably decreased the turbulence level at lower velocities. The distinct effects of positive and negative corona were attributed to the irregular, tuft like structure of the negative discharge in contrast to the uniformity of the positive corona discharge.

Kallio and Stock [10] characterized the complex flow field in a three-wire precipitator by flow visualization, numerical simulation and Laser-Doppler anemometry (LDA). A combined finite element, finite difference electrostatic model was developed to yield ion density and electric field distributions within the precipitator. These predictions were then used to calculate the electric body force in a two-dimensional, turbulent model based upon κ-ε formulation. The model predicted recirculating mean flow and turbulent diffusivities that were consistent with the smoke flow visualizations and LDA measurements. Velocity of seeded smoke was measured by two-component LDA. It was observed that inlet velocities above 0.7 m/s exhibited negligible mean flow perturbation by the electric wind. For precipitator inlet velocities less than the threshold value, gas recirculation prevailed for both polarities of corona where the extent of recirculation was roughly proportional to the current. Strong evidence of turbulent dispersion and large scale

mixing was presented for these low inlet velocity situations.

McKinney [17] conducted experiments to study the large scale secondary flows and turbulence induced by the negative corona discharge in the case of plate-plate precipitators with a barbed plate discharge electrode. Electrical characteristics were studied via current-voltage relationships for each electrodes and fluid dynamic properties were studied via hot film anemometry and laser light sheet flow visualization. The barbed planar discharge electrode did provide uniform current density reducing gas sneakage and hence increase in the efficiency as compared to the wire-plate geometry. As for fluid dynamics part, turbulence generation by the planar electrode was as much as double that of the wire-plate precipitator.

1.3 Objective of the Present Study

Despite that many studies have been centered on the interaction of the fluid dynamics and electrostatic field, fluid dynamics involved in EHD flows is very difficult to perceive completely. From the previous studies it is also noticed that no importance is given to thermal buoyancy term which couples the energy equation and flow equations. It is presumed that along with the electrical body forces, thermal buoyancy also plays an important role in the creation of secondary flows, especially in a vertical channel. This in turn may affect the heat transfer through the channel walls in the presence of oscillatory flow. The occurrence of oscillatory flow along with the mixed convection makes understanding of the flow and temperature fields even more difficult. From the construction of ESPs it is evident that heat

convection is prominent in the peripheral channels. In these channels the inner plates remain at a higher temperature due to the hot gas flow, but the outer plates experience a temperature gradient since they are exposed to atmosphere on the outside and hot gas from the inside.

In the present study, a mathematical model of EHD flows in a vertical channel is considered. Attempt is made to understand the origin of the oscillatory flow and its effects on the heat transfer results. A two-dimensional, particle-free electrohydrodynamic laminar flow is considered. The primary objective is to establish relationship of the parameters governing the occurrence of oscillatory flow along with augmentation of heat transfer in the vertical channel flow so as to study its repercussion in the operation of ESPs and enhancement of heat transfer in heat exchangers. Studies are carried out for the case of single-wire plate geometry. Both aiding and opposing flows are considered. Two different numerical methods of determining the electric field and charge density distributions are discussed. The two methods, developed separately by Yamamoto [30] and Kallio [11], generally follow the same iterative procedure to solve the electric field equations for steady-state conditions in absence of magnetic effects. The body forces due to the space charge are included in the Navier-Stokes equations. The computation of the two-dimensional momentum equations in the vorticity-stream function form and the energy equation are performed using finite difference method. Based upon the flow and the temperature obtained, the interaction between the primary and secondary flow and the convective heat transfer are studied and presented in this report.

CHAPTER 2

ELECTROSTATIC FIELDS

The first step in the analysis of electrohydrodynamic flow is to obtain the distribution of electric field and space charge density, as accurate as possible. This chapter discusses two methods used for obtaining the electrical field distribution in a channel. These schemes are used to determine the electrical potential, electric field and charge density in wire-plate precipitators. A comparison of the results obtained from these two methods is presented and the method which is more suitable for the present study is adopted. The space charge density and electric field thus obtained are used in the calculation of the electric body force in the flow simulation.

2.1 Governing Equations of Electrostatic Field

The electrical conditions inside a wire-plate channel are determined by the strongly coupled electric field and corona-generated space charge. This corona discharge occurs over a wide range of applied voltage, from a minimum threshold called corona onset to an eventual spark breakdown. The current densities within this range are relatively small and they increase proportional to the voltage applied. The governing equations for the electrostatic field and space charge density at the steady-state condition are derived under the following assumptions:

1. The corona discharge is steady, two-dimensional, and the diffusion effect of the ions is negligible.
2. The corona discharge occurs only in the vicinity around the wire electrode, and only neutral molecules and ions which have the same polarity as the wire electrodes exist in the field.
3. Forces due to the change of dielectric constant and the electrostrictive forces are negligible as compared to the coulomb forces due to the space charge.
4. During the migrations in the electric field, the ions give their momentum to the neutral gas molecules by collisions.
5. Heat generation due to corona discharge is negligible.
6. The magnetic field due to the corona current is negligibly small.
7. Wire radius is negligible.

With these assumptions, the simplified governing equations for electrostatic field are

$$\nabla \cdot \boldsymbol{E} = \frac{\rho_c}{\epsilon_o} \tag{2.1}$$

$$\nabla \cdot \boldsymbol{J} = 0 \tag{2.2}$$

$$\boldsymbol{J} = \rho_c \, b \, \boldsymbol{E} \tag{2.3}$$

$$\boldsymbol{E} = -\nabla V \tag{2.4}$$

Equation (2.1) is the Maxwell equation, Eqn. (2.2) represents the current

continuity, Eqn. (2.3) is the point form of Ohm's law, assuming isotropic conduction and Eqn. (2.4) is derived from the definition of electric field.

Combining Eqns. (2.1) and (2.4) we obtain the Poisson's equation.

$$\nabla^2 V = -\frac{\rho_c}{\epsilon_o} \tag{2.5}$$

Combining Eqns. (2.3) and (2.4) and utilizing the Maxwells relation, Eqn. (2.1), the current density equation in terms of charge density and electric potential, is given by

$$\rho_c^2 = \epsilon_o \nabla V \cdot \nabla \rho_c \tag{2.6}$$

In order to determine the electrical characteristics of a wire-plate channel, it is necessary to solve Eqns. (2.5) and (2.6) simultaneously subject to the specified boundary conditions. In solving the equations, the corona zone surrounding the discharge wire is considered only as a source of ions and high electric fields existing in this region are not treated in the calculation. The region outside the corona zone, where the electric field strengths are relatively low, is referred to as the space-charge zone and is assumed to contain unipolar ions.

2.2 Formulation of the Numerical Solution

2.2.1 Numerical Approach by Yamamoto and Velkoff

Yamamoto and Velkoff [31] adopted Leutert and Bohlen's technique [15] to obtain solution of the electric field and space charge density distribution for a two-dimensional wire-plate type precipitator. They assumed the mobility of air as

constant while solving the Eqns. (3.5) and (3.6) simultaneously. The computational domains for the one-wire and two-wire channels are shown as shaded areas in Fig. 2.1. A very high DC positive potential is applied at the wires. For the calculation of potential and field strength, the distance between the wire and the outer boundary is considered to be 3.5 times the distance between wire and plate to avoid interference.

The two Eqns. (2.5) and (2.6) are solved simultaneously with the following boundary conditions.

$V(0,0) = V_o$, at the wire

$V(x,d) = 0$, along the plate

$E_y(x,0) = 0$, along the center line

$E_x(0,y) = 0$, along the symmetry line

$E_x(s,y) = 0$, along the symmetry line between the wires

$$I_{exp} = I_{cal} = \int_0^s \rho_c(x,d)\ E_y(x,d)\ b\ L_w\ dx \qquad (2.7)$$

where I_{exp} is the total current measured from the experiments.

L_w is the length of the corona wire.

A finite-difference method is used to solve the partial differential equations. The computational area is divided into uniform grids. The calculation begins with the solution of the charge-free Laplace equation. Since the space charge density distribution is not known initially, the space charge density at the wire is assumed.

The entire charge density distribution is calculated from the finite-difference approximation for Eqn. (2.6) and then the Poisson equation, Eqn. (2.5), is solved by using the value of the space charge density distribution. The total current is calculated at the plate and compared with the experimentally determined total current. If they are different, a new charge density at the wire is assumed and the procedure is repeated until the calculated total current at the collecting plate becomes equal to that measured for the given wire voltage.

It should be noted here that the V-I characteristics curve cannot be obtained directly from the numerical computation since the experimental value of the total current is required for finding the space charge density. This is the limitation of the model as compared to that of McDonald et al. [16].

2.2.2 Numerical Approach by Kallio and Stock

Kallio and Stock [10] developed a numerical scheme based on the approach proposed by McDonald et al. [16]. A Galerkin finite-element method with quadratic interpolation is employed in solving Poisson's equation to obtain the electric potential solution. The continuity equation is solved by using a first-order difference method to yield the space charge density distribution. Since the charge density solution normally does not posses large gradient in precipitator geometries, a comparatively coarse finite-difference grid is adequate for the analysis. Aside from the finite-element solution technique, the solution generally follows the iterative procedure of the SRI (Southern Research Institute) precipitator model [16].

In this model the ion mobility is determined by the polarity of the corona discharge, in addition to the ambient gas conditions. The solution domains for a single-wire and a two-wire channel are shown in Fig. 2.2. Due to the symmetry of the wire-plate geometry, only one quadrant needs to be considered for the two-wire case. In the one-wire case, half of the channel is assumed and analyzed as an end wire condition. The other part of the channel is assumed to experience identical electrical conditions. Following boundary conditions are considered for solving electrostatic equations for one and two-wire cases.

$E_x = 0$ along AF, FD, CD

$E_y = 0$ along AC

$V = 0$ along FD

$V = V_o$ at the wire surface

These boundary conditions are illustrated in Fig. 2.2 for one and two-wire plate channels.

The computation of the electrical conditions inside a channel using the Kallio's FE-FD model involves the execution of four FORTRAN 77 computer codes. First, the finite-element mesh for electric field computation and finite-difference grid for charge density computation are generated with user-specified geometric inputs, e.g., wire-plate spacing, wire-wire spacing and wire radius. The FE mesh near the wire bears high nodal density to accommodate high field gradients. The electrical quantities between the FE mesh nodes and FD grid points are converted through a FE-FD conversion program.

The solution procedure begins with the specification of a total corona current (per unit wire length) and a corresponding estimate (a guess value) of the applied voltage. The electric field at the FD grid points is initially estimated by using Cooperman's space charge-free analytic solution [16]. Charge density at the wire is computed using the following empirical formula,

$$\rho_{co} = \frac{I_{lo}}{2 \pi r_o b E_{co}} \tag{2.8}$$

where E_{co} is the corona onset electric field at the wire-surface given by the semi-empirical relation of Peek [19] and is further modified based on the measurements by Lawless and Sparks [13] for positive and negative corona discharge.

$$E_{co}^{+} = 3.126 \times 10^6 f \rho (1 + 0.0266 r_o^{-1/2}) \tag{2.9}$$

$$E_{co}^{-} = 3.126 \times 10^6 f \rho (1 + 0.0301 r_o^{-1/2}) \tag{2.10}$$

where f is the wire roughness factor ($f = 1$ for polished wires) and ρ is the gas density relative to its value at 25°C and 760 mm Hg.

Charge density at all other points is computed from Eqn. (2.6). The values of ρ_c at the FE nodes are then interpolated from the FD point values using a bilinear approximation over each grid rectangle. This allows the FE computation of potential at all nodes from Poisson's equation. Next, charge density is recomputed from the FD equations using the new values of electric field. Likewise, potential is recomputed using the new values of interpolated charge density. This computation

cycle is repeated until changes in potential values become less than 0.01%. Total current per unit length at the plates is then determined using the computed charge density and electric field values,

$$I_{lp} = 2\, b \sum_{n=1}^{N_x} \rho_{cn}\, E_{yn} a_{yn} \qquad (2.11)$$

where N_x is the total number of FD grid points in the x-direction along the plate, a_y is the distance between consecutive grid points in y-direction. The value of I_{lp} calculated from the above equation is compared with the specified wire value. If they do not agree to within 1%, the value of V_o is adjusted and the entire procedure is repeated until I_{lp} converges. The applied voltage is adjusted according to a power law relationship in order to speed up convergence [15]. This algorithm is effective in minimizing time required for convergence, typically requiring only three iterations to satisfy the current criterion.

During the numerical solution, the nodal connectivity data for the frame nodes in the wire-plate model was generated which formed the input for generation of FE mesh. The ESPMOD.F program of Kallio [11] was modified to accept more widely used IMSL library functions instead of LINPACK library functions for solving the matrices.

2.3 Analysis of Numerical Solution

The main shortcoming of Yamamoto's model [30] is that it needs experimentally determined total current in the analysis. This handicaps the usage of the model for the calculation of V-I characteristics curves for wire-plate precipitators. Kallio's model [11], on the other hand, has no such restriction. It also takes care of high field gradients near the wire by using finite element mesh for solving the Poisson's equation. To evaluate these two numerical approaches, single and two-wire precipitators are considered (Figs. 2.1 and 2.2). These models bear the same dimensions as that of Yamamoto's experimental stetup [30] (r_o = 100 μm, d = 0.03m, S_x = 0.105m).

A comparison of V-I characteristics obtained from Kallio's numerical model with Yamamoto's experimental results for one-wire and two-wire has been shown in Figs. 2.3 and 2.4 respectively. It is observed that the numerical solution of Kallio gives good results for non-uniform grids. Attempts to use uniform grids show digression of the curve from the experimental data.

To evaluate E_x, E_y and charge density distribution, the electrical values obtained using non-uniform grid from Kallio's numerical solution were converted into those for the uniform grid (as considered by Yamamoto) using quadratic interpolation. It is observed that the results of Yamamoto's and Kallio's numerical model, in general, agree very well for E_x, E_y and space charge density distributions for single-wire and two-wire configurations (Figs. 2.5 - 2.8).

A close examination on the output of Kallio's numerical model for E_x and E_y, especially for the one-wire case, it is observed that the boundary conditions $E_x = E_y = 0$ at the wire as considered by Yamamoto are omitted. Further the boundary condition $E_x = 0$ along BE is not considered in Kallio's numerical model. This has, to some extent, affected the symmetry of E_x and E_y distribution in both quadrants for the case of one-wire plate. The effects of non-symmetry of E_x and E_y distribution are realized during the study of secondary flow in the channel. Yamamoto instead solved the equations for only one quadrant and then applied the results to the other quadrant forcing the symmetrical condition on the electrical distribution.

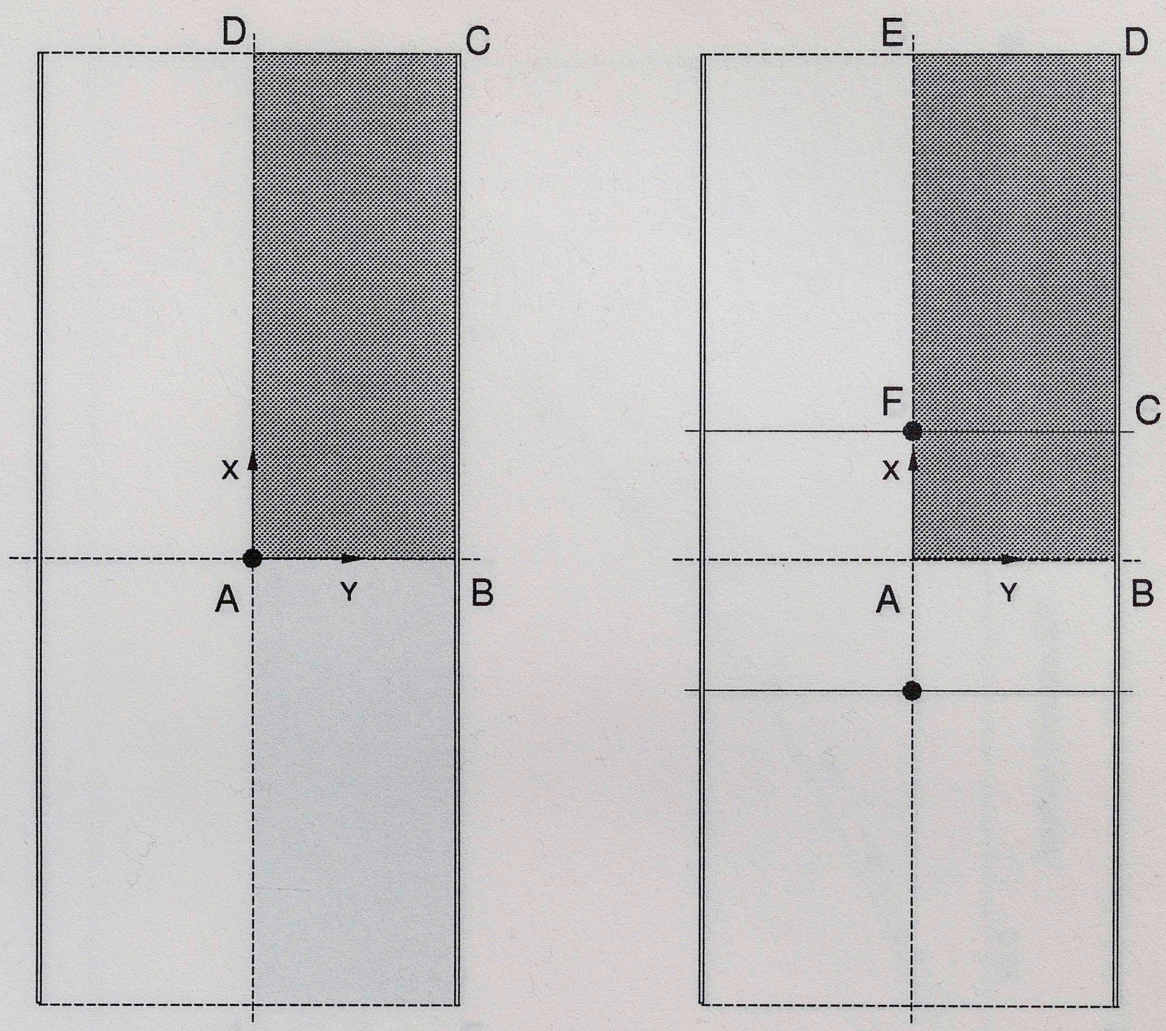

ONE-WIRE CHANNEL

TWO-WIRE CHANNEL

Figiure : 2.1 Computational Domain of Yamamoto's Model for One-Wire and Two-Wire Chanel.

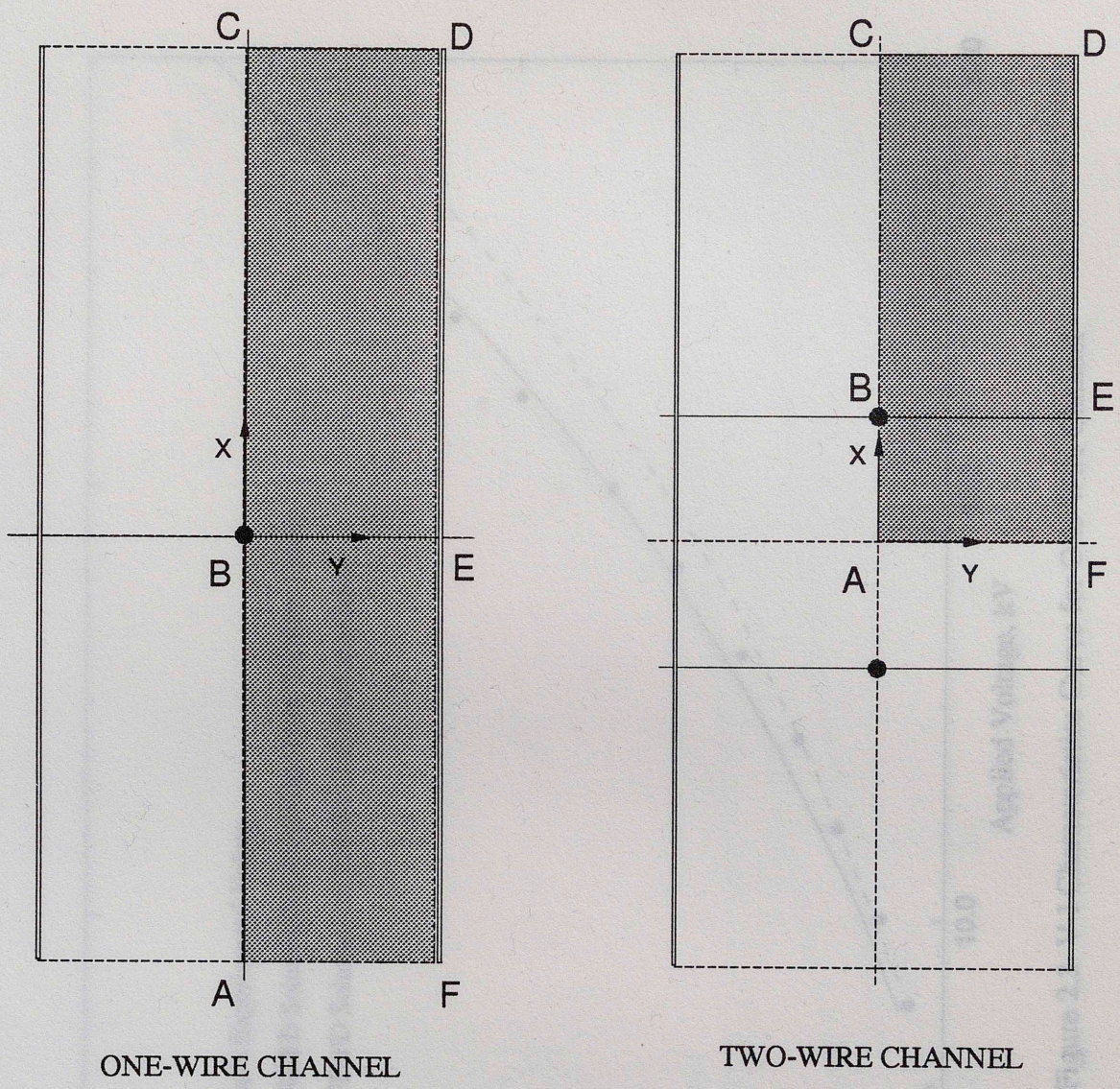

Figiure : 2.2 Computational Domain of Kallio's Model for One-Wire and Two-Wire Chanel.

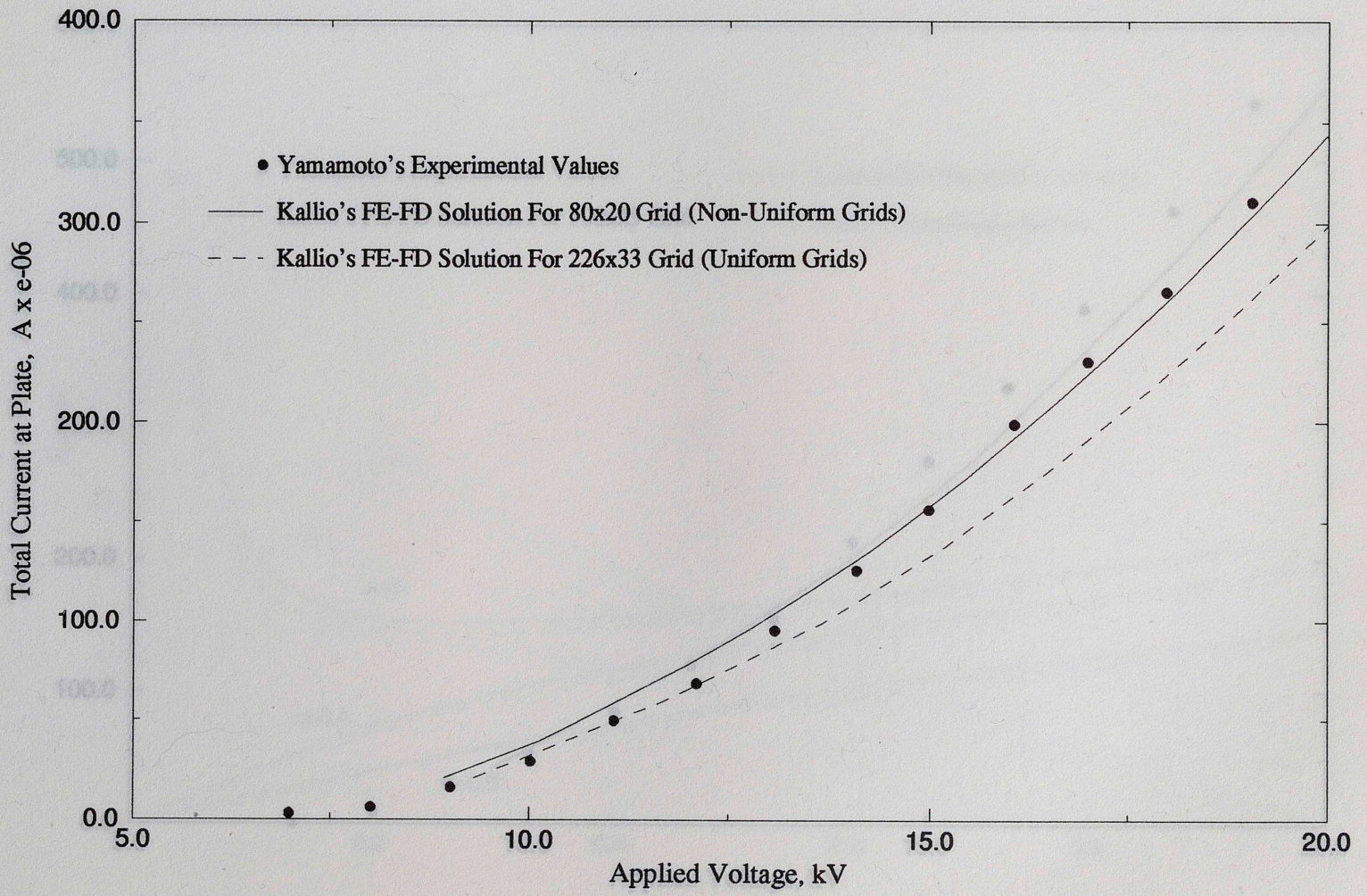

Figure 2.3 V-I Characteristics Curve for One-Wire Channel

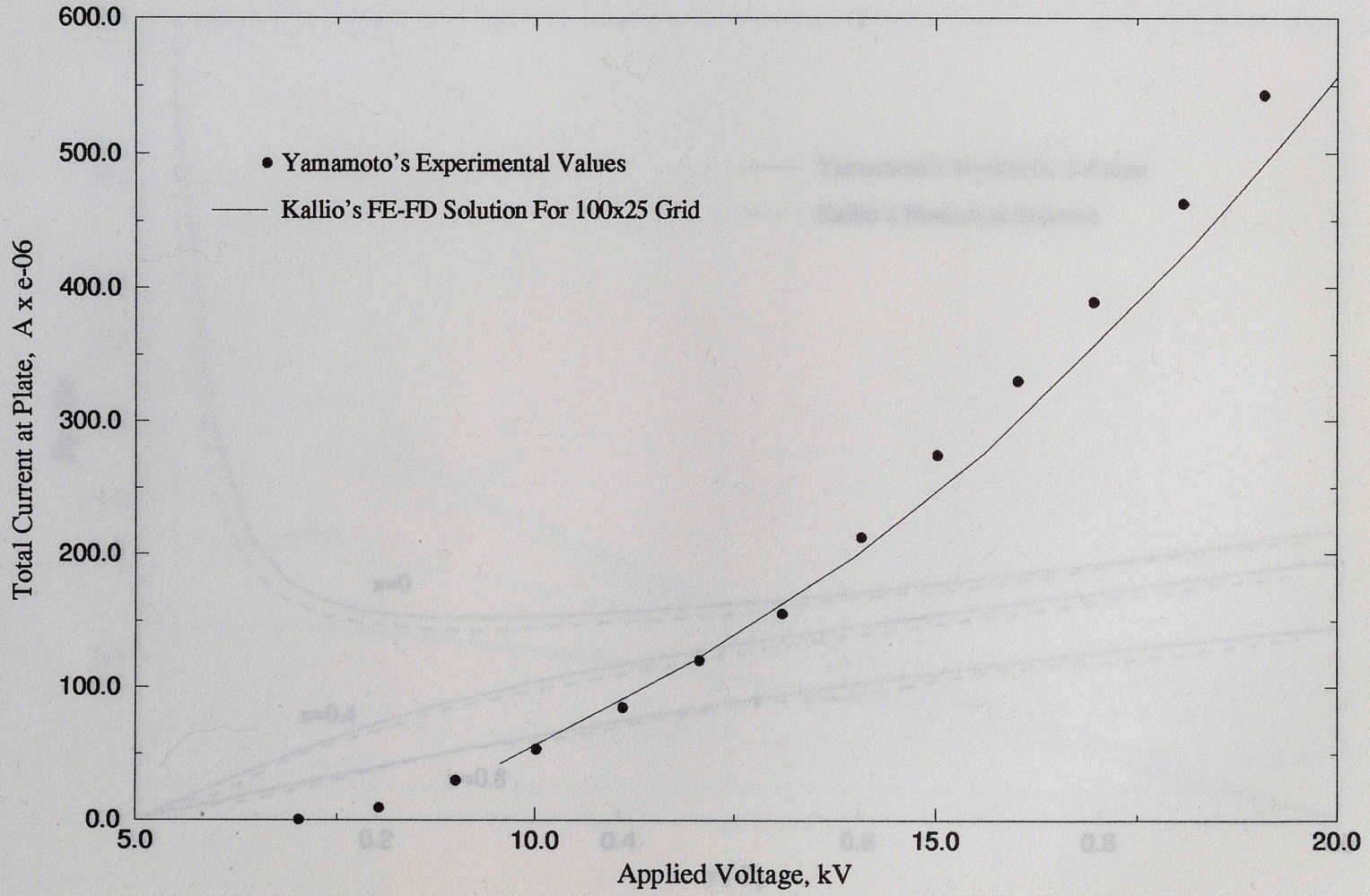

Figure 2.4 V-I Characteristics Curve for Two-Wire Channel

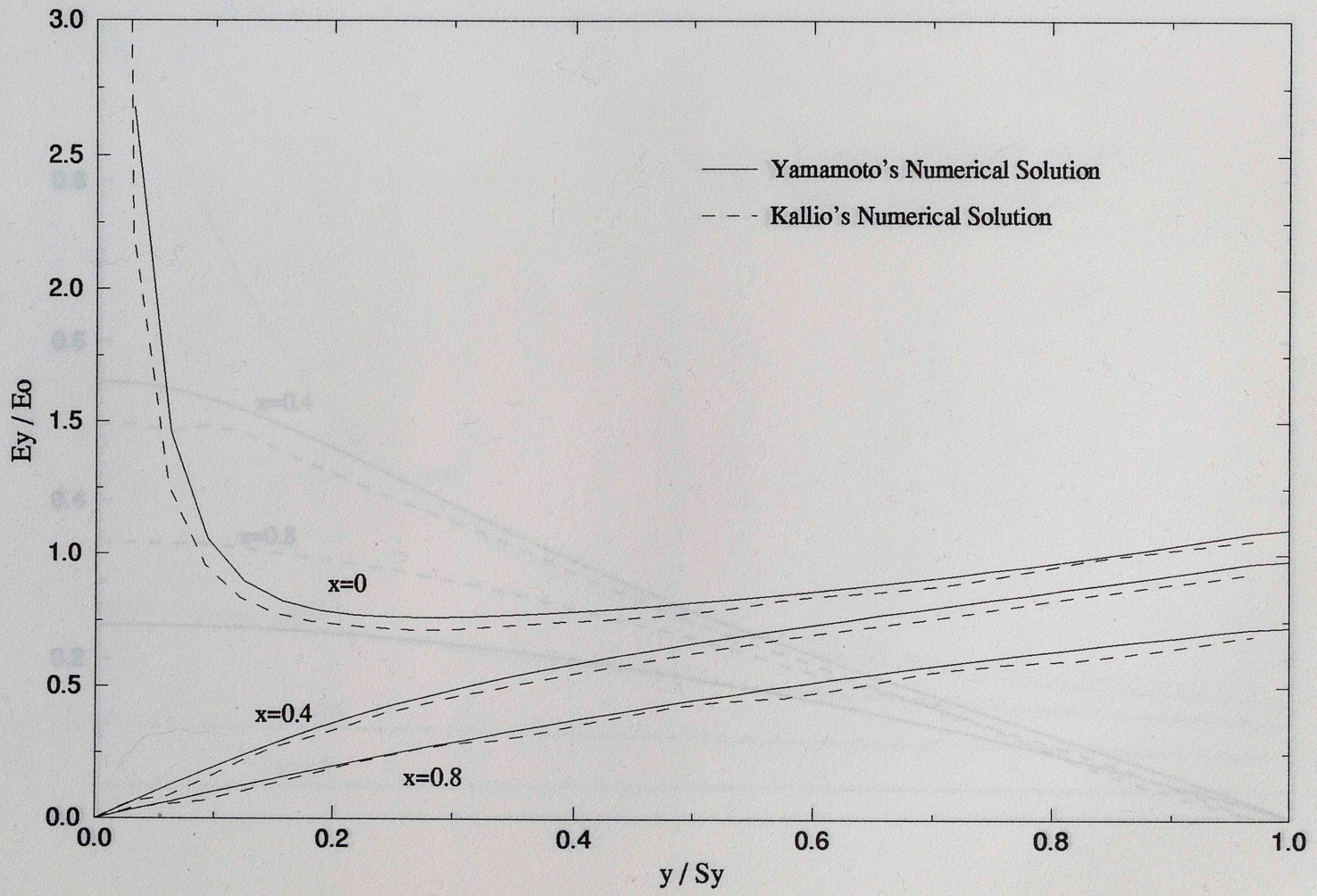

Figure 2.5 Normalized Ey Distribution for One-Wire Channel

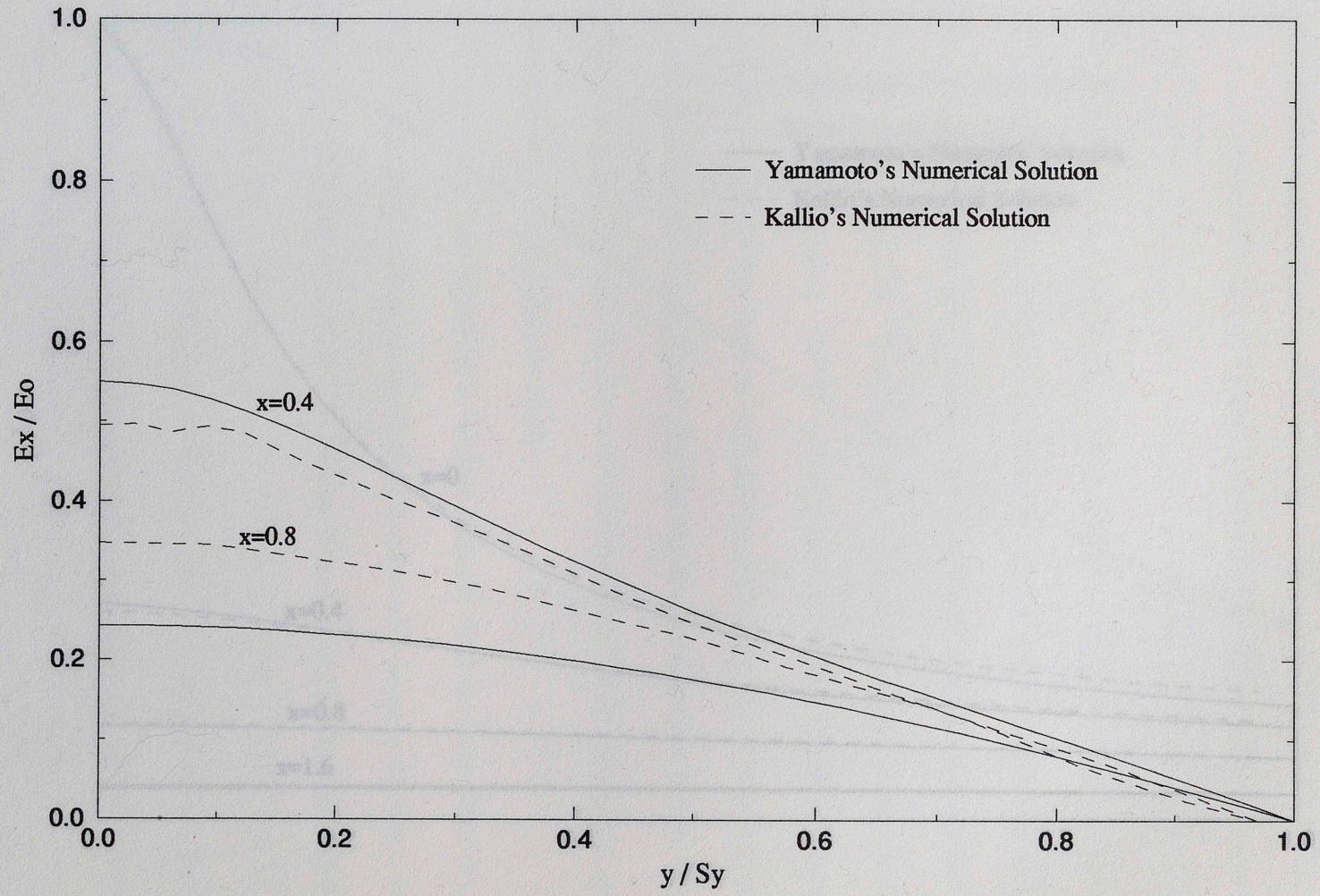

Figure 2.6 Normalized Ex Distribution for One-Wire Channel

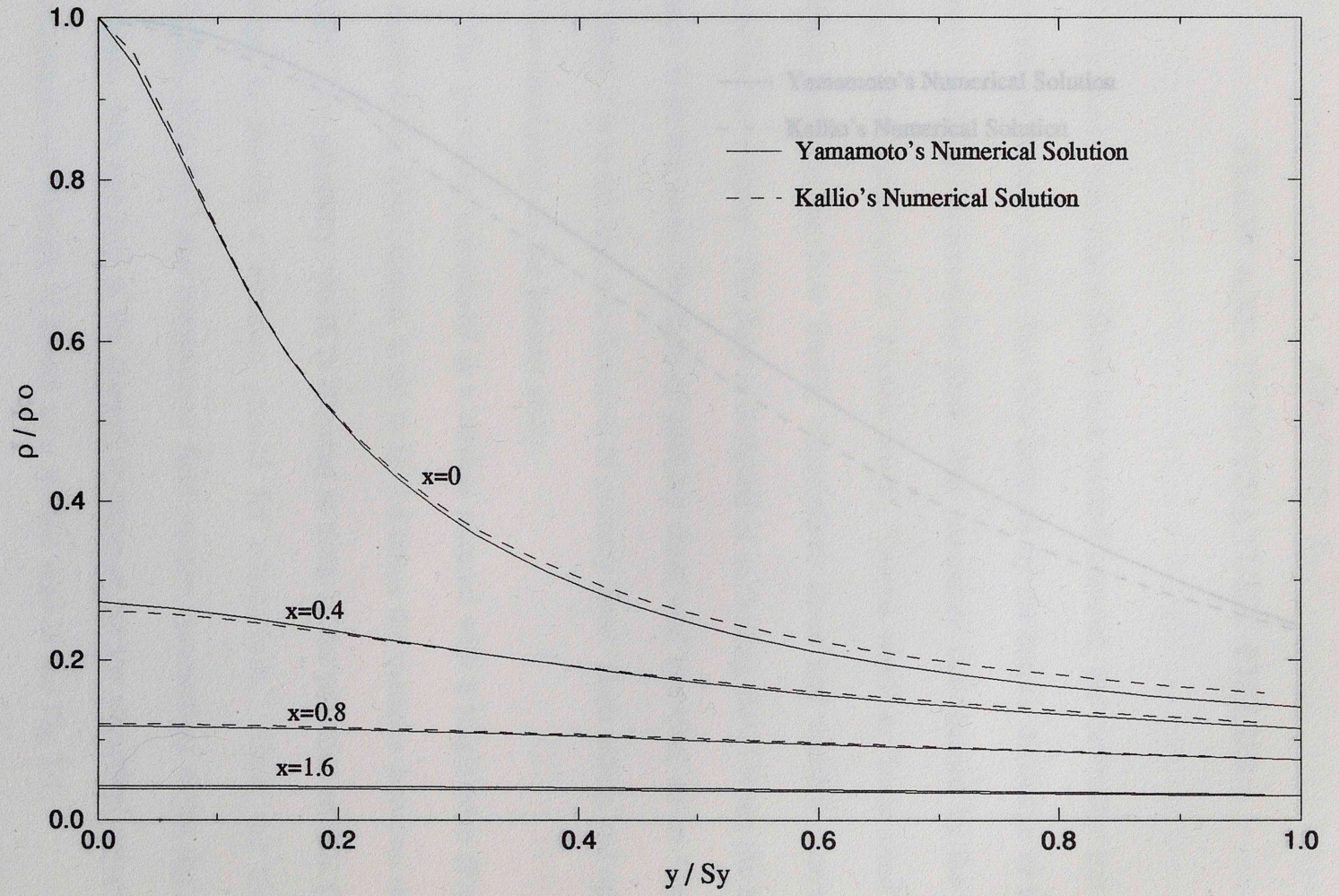

Figure 2.7 Normalized Charge Density Distribution for One-Wire Channel

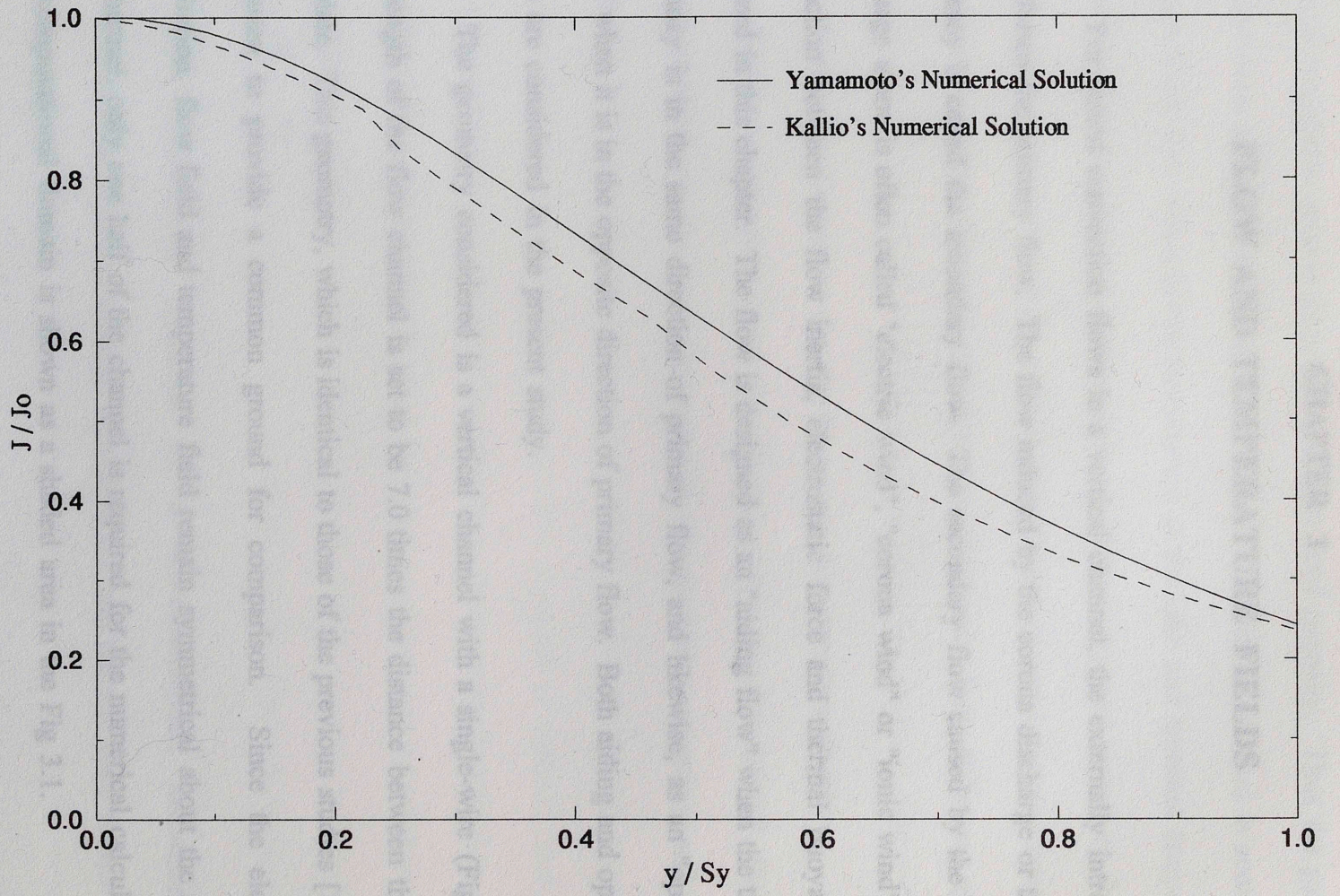

Figure 2.8 Normalized Current Density Distribution for One-Wire Channel

CHAPTER 3

FLOW AND TEMPERATURE FIELDS

For mixed convection flows in a vertical channel, the externally introduced flow forms the primary flow. The flow induced by the corona discharge or thermal buoyancy is called the secondary flow. The secondary flow caused by the corona discharge alone is often called "electric wind", "corona wind" or "ionic wind". The interaction between the flow inertia, electrostatic force and thermal buoyancy is analyzed in this chapter. The flow is designed as an "aiding flow" when the thermal buoyancy is in the same direction of primary flow, and likewise, as an "opposing flow" when it is in the opposite direction of primary flow. Both aiding and opposing flows are considered in the present study.

The geometry considered is a vertical channel with a single-wire (Fig. 3.1). The length of the flow channel is set to be 7.0 times the distance between the wire and plate. This geometry, which is identical to those of the previous studies [12,30], is chosen to provide a common ground for comparison. Since the electrical distribution, flow field and temperature field remain symmetrical about the axis of the channel, only one half of the channel is required for the numerical calculations. The computational domain is shown as a shaded area in the Fig 3.1.

It is assumed that the external body force due to the space charge and field strength is not affected by the gas flow since the ion velocity is approximately two orders of magnitude greater than the secondary flow intensity. Thus the gas flow will have little effect on the motion of the ions. A transient problem is considered with a uniform flow and uniform temperature at the inlet and constant temperature at the channel walls. The interactions between the primary, and secondary flow are analyzed with respect to time for various inlet conditions and buoyancy intensities. The governing partial differential equations are solved using finite difference method.

3.1 Governing Equations for the Flow and Temperature Fields

The basic equations used for obtaining the two-dimensional flow and temperature fields are the continuity equation, Navier-Stokes equations and energy equation.

3.1.1 Flow Field

The continuity equation is given by

$$\frac{\partial u}{\partial x} + \frac{\partial v}{\partial y} = 0 \qquad (3.1)$$

The Navier-Stokes equations for a two-dimensional, incompressible, Newtonian fluid in a vertical channel with electrical and thermal body forces can be written as [21],

$$\frac{\partial u}{\partial t} + u\frac{\partial u}{\partial x} + v\frac{\partial u}{\partial y} = -\frac{1}{\rho}\frac{\partial P}{\partial x} + \nu\left(\frac{\partial^2 u}{\partial x^2} + \frac{\partial^2 u}{\partial y^2}\right)$$

$$+ \frac{\rho_c}{\rho}E_x \pm g\beta(T-T_w) \qquad (3.2)$$

$$\frac{\partial v}{\partial t} + u\frac{\partial v}{\partial x} + v\frac{\partial v}{\partial y} = -\frac{1}{\rho}\frac{\partial P}{\partial y} + \nu\left(\frac{\partial^2 v}{\partial x^2} + \frac{\partial^2 v}{\partial y^2}\right) + \frac{\rho_c}{\rho}E_y \qquad (3.3)$$

Here $\frac{\rho_c}{\rho}E_x$ and $\frac{\rho_c}{\rho}E_y$ are the body force terms due to the electrical field. The plus sign in front of the thermal buoyancy term, the last term in Eqn. (3.2), represents aiding flows while the minus sign is for opposing flows.

The flow calculation can be simplified by re-writing the two momentum equations, with the help of continuity equation, in terms of vorticity and stream function. This eliminates the need for calculating the pressure distribution, making the calculations simple by dealing with only two equations instead of three if they were written in primitive variable form.

Pressure terms in Eqns. (3.2) and (3.3) are eliminated by cross differentiation of Eqns. (3.2) and (3.3) and subtracting one from the other. Further, using the definitions of stream function and vorticity, as

$$u = \frac{\partial \psi}{\partial y}, \qquad v = -\frac{\partial \psi}{\partial x} \qquad (3.4)$$

$$\omega = \frac{\partial u}{\partial y} - \frac{\partial v}{\partial x} \tag{3.5}$$

Vorticity transport equation and the elliptic Poisson's equation take the following form

$$\frac{\partial^2 \psi}{\partial x^2} + \frac{\partial^2 \psi}{\partial y^2} = \omega \tag{3.6}$$

$$\frac{\partial \omega}{\partial t} = -\frac{\partial \psi}{\partial y}\frac{\partial \omega}{\partial x} - \frac{\partial \psi}{\partial x}\frac{\partial \omega}{\partial y} + \nu\left(\frac{\partial^2 \omega}{\partial x^2} + \frac{\partial^2 \omega}{\partial y^2}\right)$$

$$\pm g\beta\frac{\partial T}{\partial y} + \frac{1}{\rho}\left(\frac{\partial(\rho_c E_x)}{\partial y} - \frac{\partial(\rho_c E_y)}{\partial x}\right) \tag{3.7}$$

Eqns. (3.6) and (3.7) can be non-dimensionalized using the following expressions

$$\bar{x} = \frac{x}{d}, \qquad \bar{y} = \frac{y}{d}, \qquad \bar{t} = \frac{u_e t}{d} \tag{3.8a}$$

$$\bar{u} = \frac{u_o}{u_e} \qquad \overline{\rho_c} = \frac{\rho_c}{\rho_{co}}, \qquad \bar{V} = \frac{V}{V_0} \tag{3.8b}$$

$$\overline{\psi} = \frac{\psi}{u_e d}, \qquad \overline{\omega} = \frac{d\omega}{u_e}, \qquad \theta = \frac{T - T_w}{T_i - T_w} \tag{3.9}$$

$$u_e = \sqrt{\frac{\rho_{co} V_o}{\rho}}, \qquad Re_{ehd} = \frac{u_e d}{\nu}, \qquad Gr = \frac{g\beta(T_i - T_w)d^3}{\nu^2} \tag{3.10}$$

The non-dimensional equation for vorticity, Eqn. (3.6), becomes

$$\frac{\partial^2\overline{\psi}}{\partial\overline{x}^2} + \frac{\partial^2\overline{\psi}}{\partial\overline{y}^2} = \overline{\omega} \tag{3.11}$$

The non-dimensional vorticity transport equation, Eqn. (3.7), can be written as

$$\frac{\partial\overline{\omega}}{\partial\tau} = -\frac{\partial\overline{\psi}}{\partial\overline{y}}\frac{\partial\overline{\omega}}{\partial\overline{x}} + \frac{\partial\overline{\psi}}{\partial\overline{x}}\frac{\partial\overline{\omega}}{\partial\overline{y}} + \frac{1}{Re_{ehd}}\left(\frac{\partial^2\overline{\omega}}{\partial\overline{x}^2} + \frac{\partial^2\overline{\omega}}{\partial\overline{y}^2}\right)$$

$$\pm \frac{Gr}{Re_{ehd}^2}\frac{\partial\theta}{\partial\overline{y}} + \left(\frac{\partial\overline{V}}{\partial\overline{y}}\frac{\partial\overline{\rho}_c}{\partial\overline{x}} - \frac{\partial\overline{V}}{\partial\overline{x}}\frac{\partial\overline{\rho}_c}{\partial\overline{y}}\right) \tag{3.12}$$

3.1.2 Temperature Field

The transient energy equation for incompressible flow with constant properties and negligible viscous dissipation can be written in primitive variable form as

$$\frac{\partial T}{\partial t} + u\frac{\partial T}{\partial x} + v\frac{\partial T}{\partial y} = \alpha\left(\frac{\partial^2 T}{\partial x^2} + \frac{\partial^2 T}{\partial y^2}\right) \tag{3.13}$$

By using the vorticity and stream function definition as in equations (3.4) and (3.5) and the non-dimensional parameters defined in Eqn. (3.8, 3.9 and 3.10), the non-dimensional form of energy equation will be

$$\frac{\partial\theta}{\partial\tau} = \frac{\partial\overline{\psi}}{\partial\overline{x}}\frac{\partial\theta}{\partial\overline{y}} - \frac{\partial\overline{\psi}}{\partial\overline{y}}\frac{\partial\theta}{\partial\overline{x}} + \frac{1}{Pe}\left(\frac{\partial^2\theta}{\partial\overline{x}^2} + \frac{\partial^2\theta}{\partial\overline{y}^2}\right) \tag{3.14}$$

The initial and boundary conditions considered for solving Eqns. (3.11), (3.12) and (3.14) are

$$\bar{x} = 0, \qquad \bar{\omega} = 0, \qquad \bar{\psi} = \bar{u}_o \bar{y}, \qquad \theta = 1 \tag{3.15}$$

$$\bar{x} = L, \qquad \frac{\partial \bar{\psi}}{\partial \bar{x}} = 0, \qquad \frac{\partial \bar{\omega}}{\partial \bar{x}} = 0, \qquad \frac{\partial \theta}{\partial \bar{x}} = 0 \tag{3.16}$$

$$\bar{y} = 0, \qquad \bar{\psi} = 0, \qquad \bar{\omega} = 0, \qquad \frac{\partial \theta}{\partial \bar{y}} = 0 \tag{3.17}$$

$$\bar{y} = 1, \qquad \bar{\psi} = \bar{u}_o, \qquad \bar{\omega} = \frac{\partial^2 \bar{\psi}}{\partial \bar{y}^2}, \qquad \theta = 0 \tag{3.18}$$

At the channel exit, gradients of stream function, vorticity and temperature are set to zero. These boundary conditions are less restrictive and are widely accepted.

3.2 Finite Difference Formulation

The vorticity-stream function equations and the energy equation are solved using the finite difference method. A uniform mesh is considered over the computational domain. The finite difference approximation of the Eqns. (3.11), (3.12) and (3.14) are obtained by discretizing the equations using the control volume approach [8, 18]. The basic idea of the control-volume formulation is easily understood and lends itself to direct physical interpretation. The computational domain is divided into a number of non-overlapping control volumes such that there

is one control volume surrounding each grid point. The differential equations are integrated over such a control volume.

The most attractive feature of the control volume formulation is that the resulting solution would imply that, the integral conservation of quantities such as mass, momentum and energy is exactly satisfied over any group of control volumes and, of course, over the entire computational domain. This characteristic exists for any number of grid points, not just in a limiting sense when the number of grid points becomes large. Thus, even the coarse-grid solution exhibits exact integral balances.

The control volume discretization of the convective, diffusive and body force terms in the vorticity transport and energy equation is on similar lines. For clear understanding, the finite difference formulation for the convective terms in the vorticity transport equation, Eqn. (3.12), is described in detail here.

Figure 3.2 shows the area of interest surrounding a grid point P, along with the adjacent nodes N, S, E and W. The finite difference equations are primarily expressed in terms of the values of the variables at these nodes, and to a lesser extent in terms of the values on the nodes labeled NE, NW, SE and SW. The integration is performed over the control volume shown by the dotted lines, which encloses the point P. The convective terms in Eqn. (3.12) can be integrated to give,

$$I_C = \int_s^n \int_w^e \left[\frac{\partial \bar{\psi}}{\partial \bar{x}} \frac{\partial \bar{\omega}}{\partial \bar{y}} - \frac{\partial \bar{\psi}}{\partial \bar{y}} \frac{\partial \bar{\omega}}{\partial \bar{x}} \right] d\bar{x}\, d\bar{y} \qquad (3.19)$$

The above equation can be expanded to give

$$I_C = \int_s^n \overline{\omega}_w \left[\frac{\partial \overline{\psi}}{\partial \bar{y}}\right] d\bar{y} - \int_s^n \overline{\omega}_e \left[\frac{\partial \overline{\psi}}{\partial \bar{y}}\right] d\bar{y} + \int_w^e \overline{\omega}_n \left[\frac{\partial \overline{\psi}}{\partial \bar{x}}\right] d\bar{x} - \int_w^e \overline{\omega}_s \left[\frac{\partial \overline{\psi}}{\partial \bar{x}}\right] d\bar{x} \qquad (3.20)$$

Considering the second term, there exists a value $(\overline{\omega}_e)_m$ lying between the maximum and minimum values of $\overline{\omega}_e$ on the integration interval, such that

$$(\overline{\omega}_e)_m = \frac{\int_s^n \overline{\omega}_e \left[\frac{\partial \overline{\psi}}{\partial \bar{y}}\right] d\bar{y}}{\int_s^n \left[\frac{\partial \overline{\psi}}{\partial \bar{y}}\right] d\bar{y}} = \frac{I_1}{\overline{\psi}_{ne} - \overline{\psi}_{se}} \qquad (3.21)$$

Thus, the expression for I_1 can be obtained as

$$I_1 = (\overline{\omega})_{em} [\overline{\psi}_{ne} - \overline{\psi}_{se}] \qquad (3.22)$$

Using the upwind difference approximation, $(\overline{\omega}_e)_m$ can be expressed as

$$(\overline{\omega}_e)_m = \overline{\omega}_P , \quad if \quad \overline{\psi}_{ne} - \overline{\psi}_{se} > 0 \qquad (3.23)$$

$$(\overline{\omega}_e)_m = \overline{\omega}_E , \quad if \quad \overline{\psi}_{ne} - \overline{\psi}_{se} < 0 \qquad (3.24)$$

In terms of mathematical expression, I_1 can be written as

$$I_1 = \overline{\omega}_E \frac{(\overline{\psi}_{ne} - \overline{\psi}_{se}) + |\overline{\psi}_{ne} - \overline{\psi}_{se}|}{2} + \overline{\omega}_P \frac{(\overline{\psi}_{ne} - \overline{\psi}_{se}) - |\overline{\psi}_{ne} - \overline{\psi}_{se}|}{2} \qquad (3.25)$$

In Eqn. (3.25), the expression of difference in $\overline{\psi}$, first within the bracket, and then within an absolute value sign ensures that one of the terms is zero, and the term which remains will represent the contribution from the node upstream of the *e*-face of the rectangle. It is in this way that "upwind scheme" is introduced to the finite-difference formulation. Further, substituting Eqn. (3.25) into Eqn. (3.20) we obtain the overall integral as

$$I_C = A_E(\overline{\omega}_P - \overline{\omega}_E) + A_W(\overline{\omega}_P - \overline{\omega}_W) + A_N(\overline{\omega}_P - \overline{\omega}_N) + A_S(\overline{\omega}_P - \overline{\omega}_S) \tag{3.26}$$

where

$$A_E = \frac{1}{2}\left[(\overline{\psi}_{se} - \overline{\psi}_{ne}) + | \overline{\psi}_{se} - \overline{\psi}_{ne} |\right] \tag{3.27}$$

$$A_W = \frac{1}{2}\left[(\overline{\psi}_{nw} - \overline{\psi}_{sw}) + | \overline{\psi}_{nw} - \overline{\psi}_{sw} |\right] \tag{3.28}$$

$$A_N = \frac{1}{2}\left[(\overline{\psi}_{ne} - \overline{\psi}_{nw}) + | \overline{\psi}_{ne} - \overline{\psi}_{nw} |\right] \tag{3.29}$$

$$A_S = \frac{1}{2}\left[(\overline{\psi}_{sw} - \overline{\psi}_{se}) + | \overline{\psi}_{sw} - \overline{\psi}_{se} |\right] \tag{3.30}$$

The value of the stream function at a particular corner of the dotted rectangle (Fig. 3.2) is expressed as the average of the values on the four neighboring nodes. This can be expressed as

$$\overline{\psi}_{ne} = \frac{\overline{\psi}_{NE} + \overline{\psi}_E + \overline{\psi}_P + \overline{\psi}_N}{4} \tag{3.31}$$

$$\overline{\psi}_{nw} = \frac{\overline{\psi}_{NW} + \overline{\psi}_{N} + \overline{\psi}_{P} + \overline{\psi}_{W}}{4} \tag{3.32}$$

$$\overline{\psi}_{sw} = \frac{\overline{\psi}_{SW} + \overline{\psi}_{S} + \overline{\psi}_{P} + \overline{\psi}_{W}}{4} \tag{3.33}$$

$$\overline{\psi}_{se} = \frac{\overline{\psi}_{SE} + \overline{\psi}_{S} + \overline{\psi}_{P} + \overline{\psi}_{E}}{4} \tag{3.34}$$

Substituting Eqns. (3.31)-(3.34) into Eqns. (3.27)-(3.30), we get

$$A_E = \frac{1}{8}\left[(\overline{\psi}_{SE}+\overline{\psi}_{S}-\overline{\psi}_{NE}-\overline{\psi}_{N}) + |\ \overline{\psi}_{SE}+\overline{\psi}_{S}-\overline{\psi}_{NE}-\overline{\psi}_{N}\ |\right] \tag{3.35}$$

$$A_W = \frac{1}{8}\left[(\overline{\psi}_{NW}+\overline{\psi}_{N}-\overline{\psi}_{SW}-\overline{\psi}_{S}) + |\ \overline{\psi}_{NW}+\overline{\psi}_{N}-\overline{\psi}_{SW}-\overline{\psi}_{S}\ |\right] \tag{3.36}$$

$$A_N = \frac{1}{8}\left[(\overline{\psi}_{NE}+\overline{\psi}_{E}-\overline{\psi}_{NW}-\overline{\psi}_{W}) + |\ \overline{\psi}_{NE}+\overline{\psi}_{E}-\overline{\psi}_{NW}-\overline{\psi}_{W}\ |\right] \tag{3.37}$$

$$A_S = \frac{1}{8}\left[(\overline{\psi}_{SW}+\overline{\psi}_{W}-\overline{\psi}_{SE}-\overline{\psi}_{E}) + |\ \overline{\psi}_{SW}+\overline{\psi}_{W}-\overline{\psi}_{SE}-\overline{\psi}_{E}\ |\right] \tag{3.38}$$

The finite difference formulation for the diffusion terms in Eqn. (3.12) can be obtained in the same manner. This can be expressed as

$$I_D = \frac{1}{Re_{ehd}}\left[\frac{\overline{\omega}_{E}-2\overline{\omega}_{P}+\overline{\omega}_{W}}{(\Delta\bar{x})^2} + \frac{\overline{\omega}_{N}-2\overline{\omega}_{P}+\overline{\omega}_{E}}{(\Delta\bar{y})^2}\right] \tag{3.39}$$

The finite difference formulation for the buoyancy terms in Eqn. (3.12) can be written as

$$I_{BF} = \frac{Gr}{Re_{ehd}^{\,2}} \frac{(\theta_N - \theta_S)}{2\Delta\bar{y}} \tag{3.40}$$

The electric body force terms in Eqn. (3.12) can be re-written in terms of the electric field. From the definition,

$$\bar{E}_x = - \frac{\partial \bar{V}}{\partial \bar{x}} \tag{3.41}$$

$$\bar{E}_y = - \frac{\partial \bar{V}}{\partial \bar{y}} \tag{3.42}$$

we have,

$$I_E = \frac{\bar{E}_x(\bar{\rho}_{c_N} - \bar{\rho}_{c_S})}{2\ \Delta\bar{x}} - \frac{\bar{E}_y(\bar{\rho}_{c_E} - \bar{\rho}_{c_W})}{2\ \Delta\bar{y}} \tag{3.43}$$

The overall finite difference formulation for the vorticity transport equation is obtained by summing the individual expressions for the convection, diffusion and body force terms given by Eqns. (3.26), (3.39), (3.40) and (3.41). Thus, the value of $\bar{\omega}_p$ at a time level (n+1) can be expressed in terms of previous time level n as

$$\bar{\omega}_p^{\,n+1} = \bar{\omega}_p^{\,n} + \left[\frac{I_C}{\Delta\bar{x}\ \Delta\bar{y}} + \frac{I_D}{\Delta\bar{x}\ \Delta\bar{y}} + I_E + I_{BF} \right] \Delta\bar{t} \tag{3.44}$$

The elliptic Poisson equation given by Eqn. (3.11) can be solved by using the Gauss-Seidel technique with SOR (Successive Over Relaxation) to accelerate the convergence. The finite difference formulation for the elliptic equation is given by

$$\overline{\omega}_P = \left[\frac{\overline{\psi}_E - 2\overline{\psi}_P + \overline{\psi}_W}{(\Delta\bar{x})^2} + \frac{\overline{\psi}_N - 2\overline{\psi}_P + \overline{\psi}_E}{(\Delta\bar{y})^2} \right] \tag{3.45}$$

The correction of the Gauss-Seidal iteration when applied to the above equation can be expressed [1] as

$$\overline{\psi}_p^{\,i+1'} = \overline{\psi}_p^{\,i'} + F\left[\overline{\psi}_p^{\,i+1} - \overline{\psi}_p^{\,i'}\right] \tag{3.46}$$

where i represents the iteration level and $\overline{\psi}_p^{\,i+1}$ is the most recent value of $\overline{\psi}_p$ obtained by the Gauss-Seidal procedure, $\overline{\psi}_p^{\,i'}$ is the value from the previous iteration after the correction, and $\overline{\psi}_p^{\,i+1'}$ is the newly corrected or "better guess" for $\overline{\psi}_p$ at (i+1) iteration level. F is the relaxation parameter, and when $1 < F < 2$ over-relaxation is employed. In the present study, value of F as 1.8 gives better and faster results.

The finite-difference formulation for the energy equation can be expressed in a way similar to that of the vorticity transport equation. The value of θ_p at (n+1) time level can be expressed in terms of n time level as

$$\theta_p^{n+1} = \theta_p^n + \left[I_C + I_D\right] \frac{\Delta\bar{t}}{\Delta\bar{x}\,\Delta\bar{y}} \tag{3.47}$$

where the terms I_C and I_D are derived by replacing the $\overline{\omega}$ with θ and Re_{ehd} with Pe in Eqns. (3.26) and (3.39).

The finite difference formulation of the no-slip boundary condition at the wall which is defined in Eqn. (3.18) is obtained by application of the Taylor series expansion. The wall vorticity is obtained by expanding the second-order partial derivative of stream function using a three-point approximation with first order truncation error [1],

$$\overline{\omega}_{i,j} = \frac{2\left(\overline{\Psi}_{i+1,j} - \overline{\Psi}_{i,j}\right)}{(\Delta\overline{x})^2} \tag{3.48}$$

3.3 Calculation of Nusselt Number

The heat transfer taking place from the hot fluid to the plate in the wire-plate vertical channel is treated as a simultaneously hydrodynamical and thermal developing flow between parallel plates. The convective heat transfer coefficient is generally expressed in terms of the Nusselt number. The ratio of the convective conductance h to the pure molecular thermal conductance k/D_h is defined as the Nusselt number. At a local peripheral point on the duct boundary, the local Nusselt number is defined as

$$Nu_x = \frac{h_x D_h}{k} = \frac{q''_x D_h}{k(T_w - T_0)} = \frac{D_h\left(\frac{\partial T}{\partial y}\right)_x}{(T_w - T_m)} \tag{3.49}$$

D_h is the hydraulic diameter which is four times the duct cross-section area divided by the perimeter. Here θ_m is the fluid bulk mean temperature at an arbitrary channel cross-section which is defined as

$$\theta_m = \frac{1}{A_c\, u_m} \int_{A_c} u\, \theta\, dA_c \tag{3.50}$$

where u_m is the mean velocity at the cross-section of the channel.

The mean (flow length average) Nusselt number is given by

$$\overline{Nu} = \frac{\bar{h}\, D_h}{k} \tag{3.51}$$

The flow length average heat transfer coefficient h is given by

$$\bar{h} = -\frac{k\,(T_i - T_w)}{L\,(LMTD)} \int_0^{L^*} \frac{\partial \theta}{\partial \bar{y}}\Big|_{\bar{y}=1} d\bar{x} \tag{3.52}$$

Expressing LMTD in terms of the inlet and outlet mean temperatures, and using Eqn. (3.52), Eqn. (3.51) can be rewritten as

$$\overline{Nu} = \frac{4}{L^*} \frac{\log(1/\theta_0)}{1-\theta_0} \int_0^{L^*} \frac{\partial \theta}{\partial \bar{y}}\Big|_{\bar{y}=1} d\bar{x} \tag{3.53}$$

In the above equation the temperature gradients at the channel plate are obtained by applying 3-point finite difference approximation and further these are integrated over the flow length by applying the trapezoidal rule.

3.4 Numerical Solution

The finite difference equations for vorticity-stream function and energy equations are solved iteratively within each increment of time step. For the given dimension of the half channel, the flow Reynolds number, Grashoff number and the applied voltage form the basic input to the program. The computational time or the maximum number of iterations are fixed for each run. The computation is continued based on the behavior of the average Nusselt number with respect to time. Thus the heat transfer, either oscillatory or steady state is closely monitored. The computation is terminated when the $\overline{Nu}$ reaches steady-state or becomes steady-periodic.

The vorticity and temperature are initialized to zero before the computation, except at the inlet of the channel where non-dimensional temperature is set to unity. The stream function through out the channel is initialized to uniform flow by setting the value of stream function as linearly varying along the width of the channel, similar to that used by Yamamoto [30] and Lai et al. [12]. In each time step, first, temperature and vorticity are calculated then the stream function value at each grid point is calculated from vorticity function using Gauss-Seidel iterative technique. The convergence tolerance considered for stream function is 0.0001, with the successive over-relaxation parameter as 1.8. At the exit of the channel, the partial derivative of ψ, ω and θ with respect to the flow direction are equated to zero. $\overline{Nu}$ is computed at equal time intervals. The values of ψ and θ at all the grid points are stored at a user specified constant time interval.

The dimensionless time step chosen is 5×10^{-4} so as to guarantee numerical stability and accuracy. The stability criterion for the numerical scheme used is given by Jaluria and Torrance [9],

$$\Delta\bar{t} \le \frac{1}{2\nu\left[\frac{1}{(\Delta\bar{x})^2} + \frac{1}{(\Delta\bar{y})^2}\right] + \frac{|u|}{\Delta\bar{x}} + \frac{|v|}{\Delta\bar{y}}} \tag{3.54}$$

To verify that the observed oscillations are not due to numerical instability, the computation is repeated with a reduced time step ($\Delta\bar{t} = 1\times10^{-4}$). The results obtained are identical with $\Delta\bar{t} = 5\times10^{-4}$ time step.

Uniform grids (225x33) are used for the half-channel which is the same as the previous analyses performed by Yamamoto [30] and Lai et al. [12] for the same channel configuration. The test of grid dependence has been performed by Yamamoto [30] and is omitted here for brevity.

Most of the computations are performed on the super computer CRAY YMP which takes about 29,000 CPU seconds for 500 dimensionless time period. Some calculations taken on SUN SPARC 10 Workstation which requires 180,000 CPU seconds for the same amount of time period. The stream function and temperature contours have been plotted using TECPLOT software. In the calculation of $\overline{Nu}$ for steady-periodic cases, trapezoidal rule is used.

To investigate the origin of the oscillatory flows, the flow pattern and isotherm contours are presented for different Reynolds and Grashoff numbers at the

selected time intervals. For each case, the flow pattern is plotted using a constant $\Delta\psi$ for easy reference. The temperature contours are plotted at an increment of 0.1. The variation of $\overline{Nu}$ with respect to time are presented for both aiding and opposing flows.

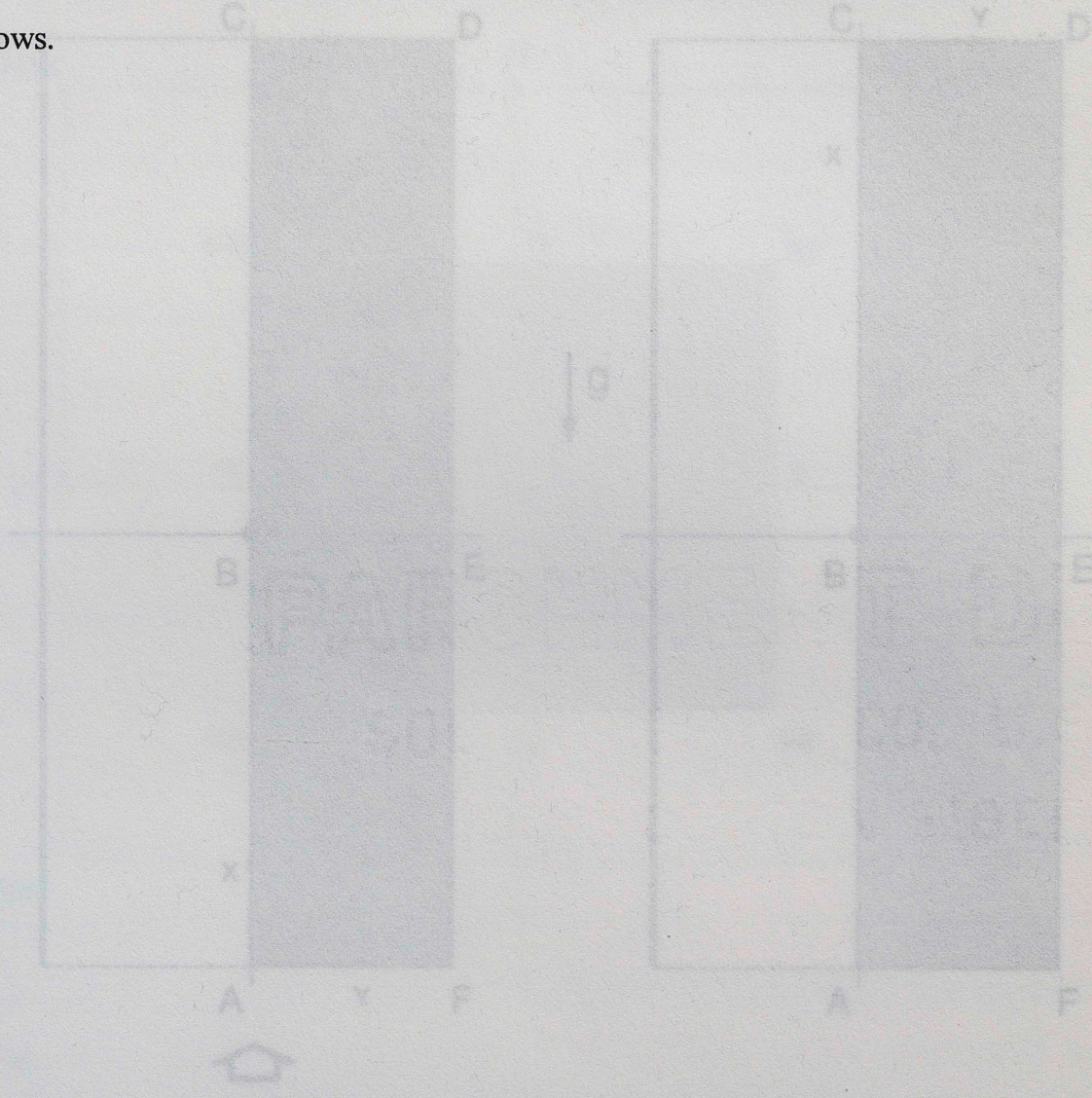

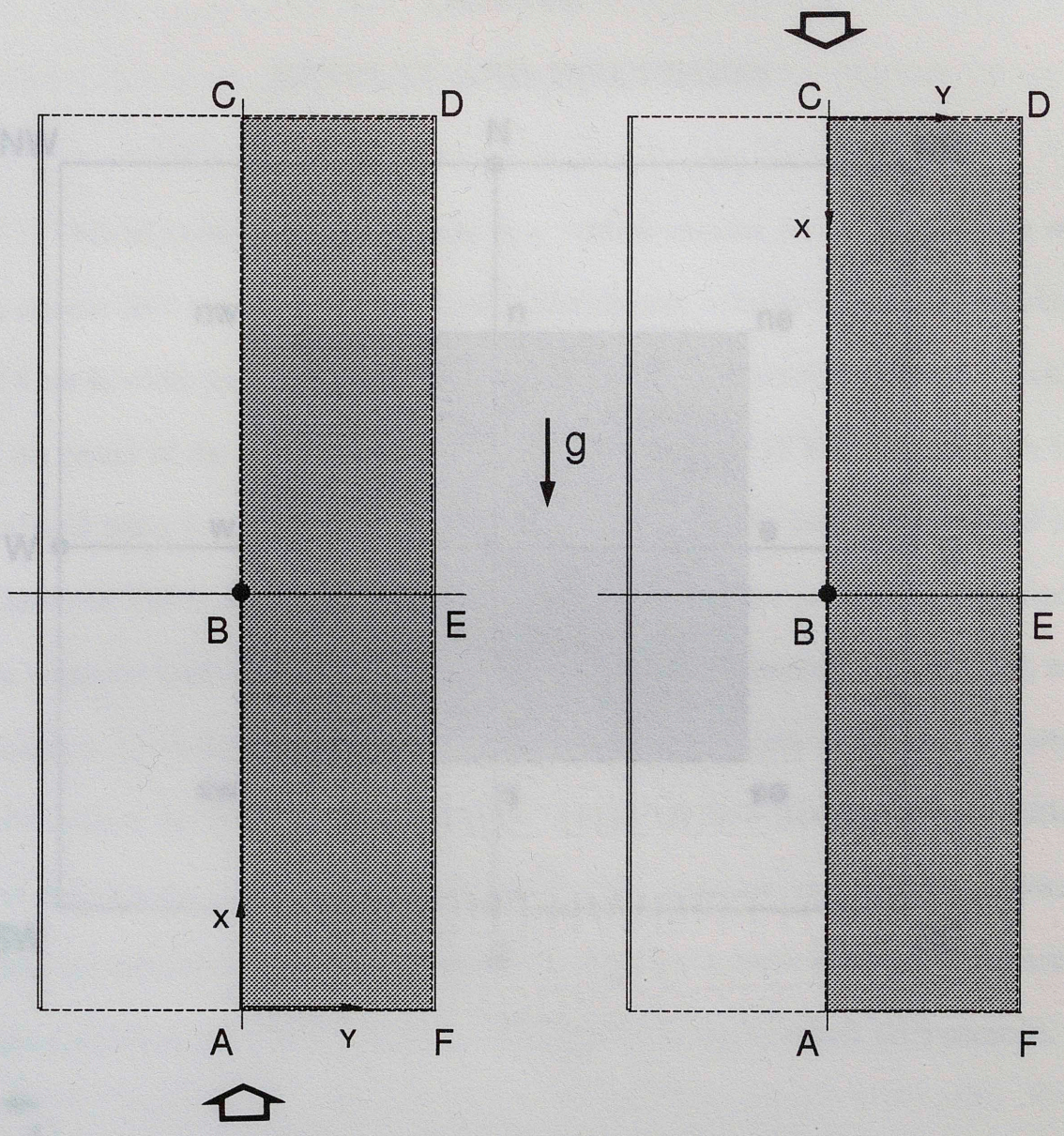

Figure 3.1 Computational Domain of One-Wire Vertical Channel

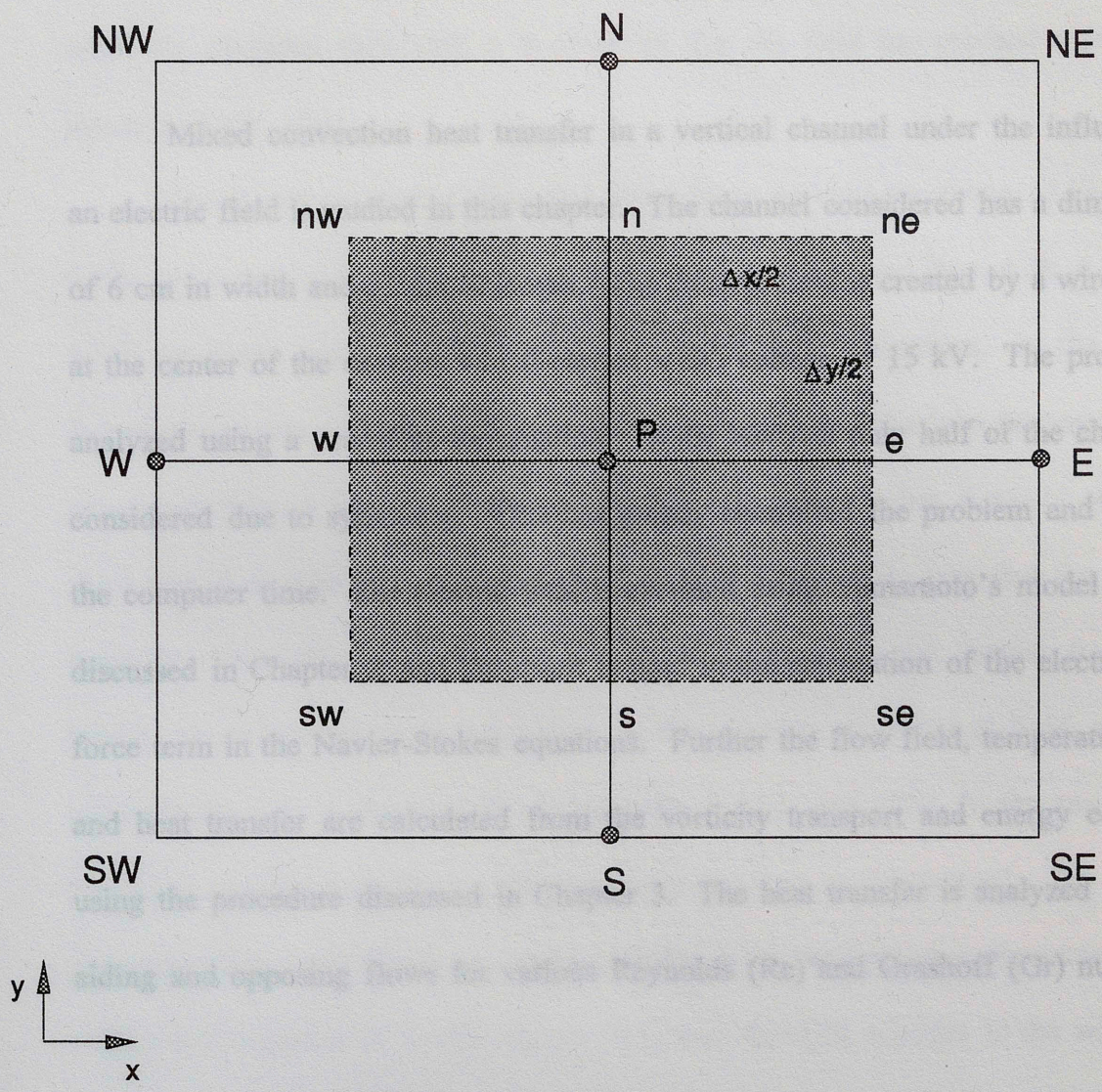

Figiure : 3.2 A Control Volume in the Computational Domain.

CHAPTER 4

RESULTS AND DISCUSSION

Mixed convection heat transfer in a vertical channel under the influence of an electric field is studied in this chapter. The channel considered has a dimensions of 6 cm in width and 21 cm in length. The electric field is created by a wire placed at the center of the channel which carries a DC voltage of 15 kV. The problem is analyzed using a transient formulation. In the analysis only half of the channel is considered due to symmetry. This has greatly simplified the problem and reduced the computer time. The electric field is obtained using Yamamoto's model [30], as discussed in Chapter 2, and the result is used in the calculation of the electric body force term in the Navier-Stokes equations. Further the flow field, temperature field and heat transfer are calculated from the vorticity transport and energy equations using the procedure discussed in Chapter 3. The heat transfer is analyzed for both aiding and opposing flows for various Reynolds (Re) and Grashoff (Gr) numbers.

4.1 Forced Convection

Flow studies based on Yamamoto's model [30] and later extended by Lai et al. [12] show that for a finite EHD Reynolds number, the flow transition can lead to either a steady-state or a periodic oscillation. In general it is observed that at least

one recirculatory cell appears near the wall opposite to the wire. This can also be observed from the flow patterns shown in Figs. 4.2b, 4.13b and 4.24b. This recirculation or secondary flow in the channel is attributed to the presence of electrical field [3, 11, 12, 26, 29, 31]. In the present study, the computer runs are taken for extended time until it is observed that the field has reached a steady or steady-periodic state.

The forced convection flow and temperature patterns are shown in Figs. 4.2a, 4.13a and 4.24a for flows in the absence of electrical field and Figs. 4.2b, 4.13b and 4.24b for flows with electrical field of various Reynolds numbers. In the case of forced convection with no electrical field, a uniform flow at the inlet becomes a fully developed flow at the outlet of the channel. The flow reaches a steady state in a short period of time for higher Reynolds number flows. It is seen that the thermal boundary layer thickness diminishes with an increase in the inertial force thus leading to an increase in heat transfer. In the presence of electrical field, only one recirculatory cell is observed for flows at Re = 1200 and 1800. In the case of low Reynolds number flow (Re = 600), two cells are seen in the channel. The thermal boundary layer, at a steady or steady-periodic state, extends over the recirculatory region and is perturbed by the electric field near the wall opposite to the wire. The thermal boundary layer is stabilized past the wire when it approaches a steady state, a phenomenon similar to that prevailing in the forced convection without an electrical field. The oscillatory temperature field in the presence of an electric field is distinguished by a wave-like appearance of the thermal boundary layer at the

downstream of the wire.

The heat transfer of forced convection is evaluated and used as a reference in the assessment of heat transfer augmentation. The results obtained for the average or mean Nusselt number ($\overline{Nu}$) for various Reynolds numbers in general agree with those reported by Shah and London [24]. The differences observed in $\overline{Nu}$ obtained in this analysis and those tabulated by Shah and London [24] is due to the boundary layer approximation used in the latter analysis. The enhancement in heat transfer in the presence of electric field are compared with the forced convection in the channel without electric field.

The increase in the flow inertia (i.e., the Reynolds number), in the presence of electric field, results in a declination in the percentage of heat transfer enhancement. For example, the increase in heat transfer for Re = 600 is 168% and it is 135% for Re = 1800. This is due to the suppression of the secondary flow. With the inception of thermal buoyancy, the behavior is very different for aiding and opposing flows as will be elaborated in the next section.

4.2 Mixed Convection

4.2.1 Flows at Re = 1800

For flows at Re = 1800, the flow pattern shows only one recirculatory cell near the wall opposite the wire. This is shown in figures 4.4 through 4.11. As observed the flow fields do not show any oscillation and they all reach a steady state. With an increase in the buoyancy strength (i.e., an increase in the Grashoff

number), the flow field reaches steady state earlier for opposing flows as compared to that of aiding flows. This can be clearly seen from Fig. 4.9.

Figures 4.3, 4.6 and 4.9 show the variation of $\overline{Nu}$ with time. It is observed that heat transfer increases in the case of opposing flows as compared to that of aiding flows. The enhancement in heat transfer being 120% to 140% for Grashoff number less than 10^5. At Gr = 10^6, aiding flow experiences a drastic drop in the heat transfer, on the other hand, a steep increase in heat transfer of about 170% is observed for opposing flows. The reasoning can be justified from the flow pattern and temperature distribution for various cases of Grashoff numbers. In the case of opposing flows the recirculatory region is suppressed due to the interaction of primary flow and the buoyancy force. In the case of aiding flows the recirculatory cell is seen elongated with an increase in the buoyancy strength. This phenomenon is most prominent in the case of Gr = 10^6 as seen from the streamline patterns (Figs. 4.10a and 4.11a). The elongated recirculatory cell actually resembles a flow reversal, hence affecting the heat transfer by the primary flow. From the flow patterns, it is observed that an increase in the thermal buoyancy causes the primary flow to channelize towards the center of the flow passage due to expansion of the secondary flow. The temperature contours show an increase in the boundary layer thickness due to the separation of the primary flow from the wall which clearly is responsible for the drop in heat transfer. In the case of opposing flows, with an increase in thermal buoyancy, the primary flow shows a developed flow pattern due to the suppression of the secondary flow region. This helps to keep the thermal

boundary layer close to the wall hence aiding the increase in heat transfer. The enhancement in heat transfer under different intensities of buoyancy force for aiding and opposing flows is summarized in Table 4.1. As seen from the table the percentage increase in the heat transfer increases with the Grashoff number for opposing flows. Besides higher thermal buoyancy causing an increase in the heat transfer, the contribution from the presence of electric field is also prominent as seen from Gr = 10^6 case. The drastic drop in the heat transfer for aiding flow with an increase in the Grashoff number is also evident from the summarized results in the table. Contribution from thermal buoyancy is exceedingly high as compared to that from the electrical field, for the drop in the heat transfer for aiding flows.

4.2.2 Flows at Re = 1200

While the flow patterns and isotherm contours for Gr = 10^4, 10^5, and 10^6 are presented in Figs. 4.15 through 4.22, the variation of $\overline{Nu}$ with time at the corresponding conditions are shown in Figs. 4.14, 4.17 and 4.20 for aiding and opposing flows. For flows at Gr = 10^4, it is observed that the flow field oscillates with the same frequency as that of the forced convection. Since the buoyancy is weak, it is also observed that the flow patterns for aiding and opposing flows are similar to that of forced convection. Because of this, the change in the $\overline{Nu}$ is not noticeable for aiding and opposing flows as compared to that for Gr = 0.

As the Grashoff number is increased to 10^5, little change in the oscillatory period is noticed but the amplitude of oscillation for $\overline{Nu}$ is reduced indicating that the transition from oscillation to steady-state is strongly dependent on the Grashoff number. For opposing flow, the flow field first exhibits an oscillatory nature but reaches a steady-state finally. This is shown in Fig. 4.17 for both aiding and opposing flows. In both cases of Gr = 10^4 and 10^5, the wave-like thermal boundary layer at the downstream of the recirculatory cell propagates towards the exit of the channel (Figs. 4.15d, 4.16d and 4.18d).

It is seen that due to high buoyancy intensity in the case of Gr = 10^6, the flow field reaches a steady state for both aiding and opposing cases (refer to Fig. 4.20). It is apparent from the streamline profiles (Fig. 4.21a) that the recirculatory region for aiding flow is extended over almost the entire channel. The case of flow reversal as explained earlier is observed in Fig. 4.12b. Because of the blockage between the primary flow and the wall, the secondary flow causes a drastic decrease in $\overline{Nu}$. In opposing flow this recirculation region is effectively suppressed (Fig. 4.22a) and the flow field reaches a steady state in a rather short time. The thin thermal boundary layer as seen in Fig. 4.22b is the reason for the improvement in the heat transfer as compared to that of the aiding flow (Fig. 4.21b).

For the case of Re = 1200, following observations are made,

1. $\overline{Nu}$ decreases with an increase in the buoyancy intensity in the case of aiding flows.

2. An increase in the Grashoff number leads the flow transition from an oscillatory state to a steady state.

3. For opposing flows, $\overline{Nu}$ increases with the Grashoff number.

4. A steady-state is reached for opposing flow at Gr = 10^5 while aiding flow still remains oscillatory.

4.2.3 Flows at Re = 600

The flow pattern for Gr = 10^4 is very similar to that obtained by Lai et al. [12] for the same flow condition without the thermal effect. In addition, little difference is found in the flow pattern for aiding and opposing flows for this case. This has led to a speculation that the variation of $\overline{Nu}$ should also be similar. The variation of $\overline{Nu}$ with respect to time is shown in Fig 4.25. Although the inertial force is weak, due to the existence of a weak buoyant force (Gr = 10^4), there is a marginal increase in $\overline{Nu}$.

For aiding flows at Gr = 10^5, there is an increase in the recirculation velocities (ψ_{max} and ψ_{min} are higher than those of Gr = 10^4). As a result, it leads to an increase in $\overline{Nu}$ over that at Gr = 10^4 is observed (Fig. 4.28). The increase in the amplitude of $\overline{Nu}$ is also a result of the increase in the minimum and maximum velocities. For the opposing flow case, the flow field goes through several transitions and finally reaches a steady state despite that a recirculation still remains

in the channel near the wire. Although the stream function attains a very large value (as compared to that in aiding flow), the recirculatory cell is mainly confined to the center of the channel and it does not improve the heat transfer significantly.

For the case of Gr = 10^6, opposing flow reaches steady state with only one recirculatory cell. This is again due to the inertial forces suppressing the secondary flow and hence resulting in an increase in the heat transfer. Aiding flow in this case shows oscillations in the flow and temperature fields but does not reach a steady-periodic state. A drop in the heat transfer is observed as compared to those at lower Grashoff numbers.

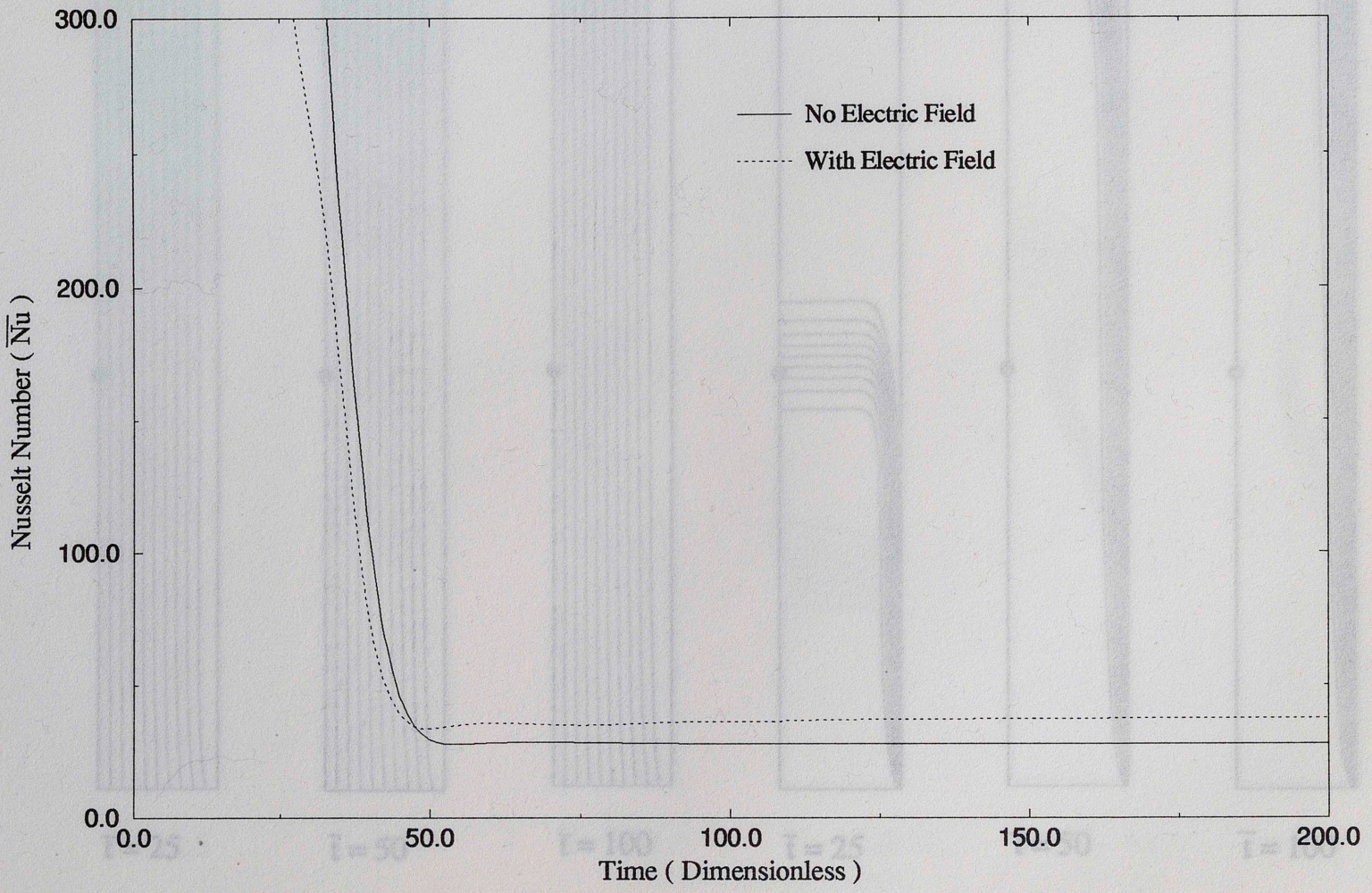

Figure 4.1 Variation of Average Nusselt Number with Time for Forced Convection (Re=1800)

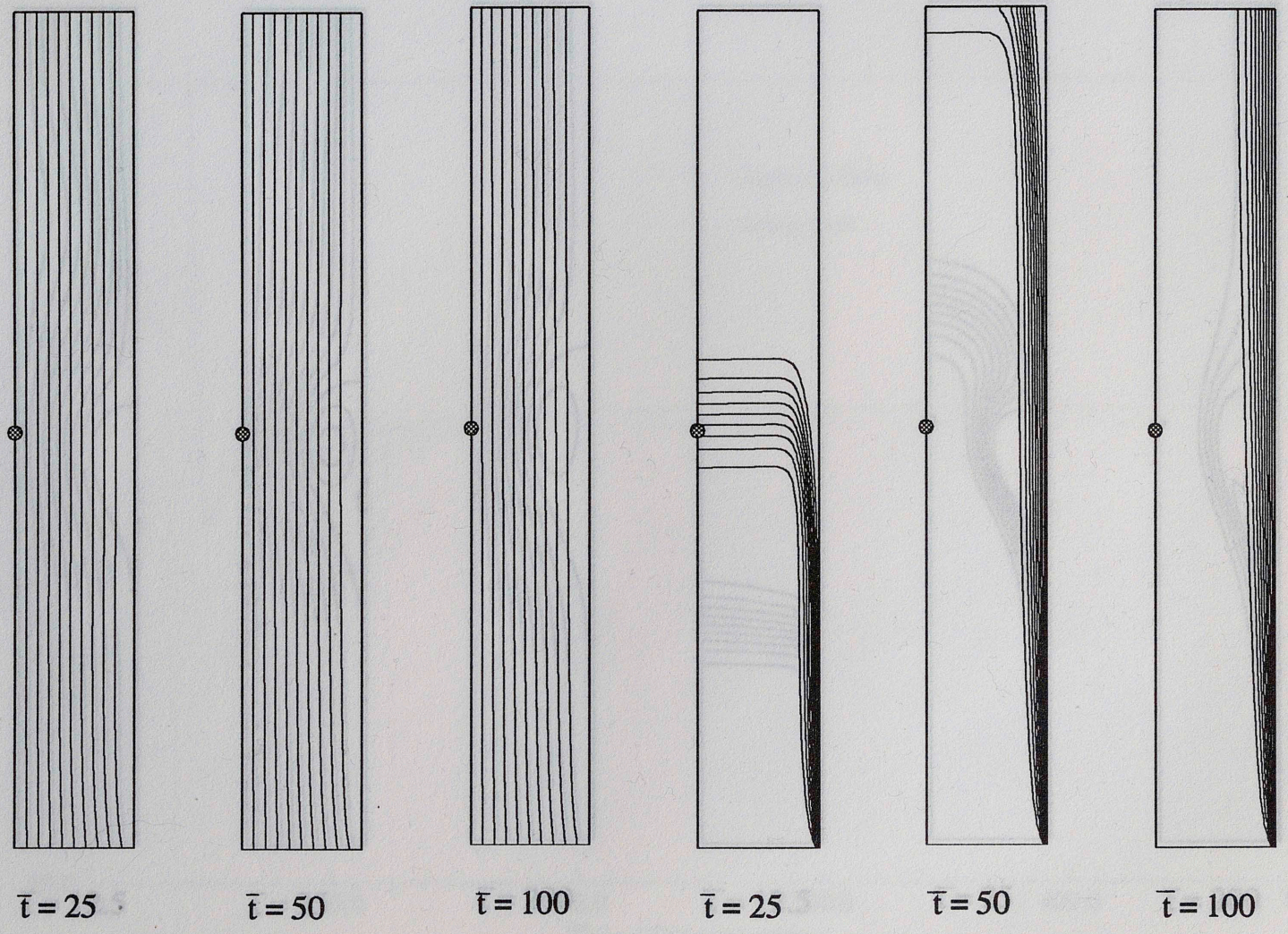

Figure 4.2a Development of Flow and Temperature Field for Forced Convection
(Without Electric Field Re = 1800)

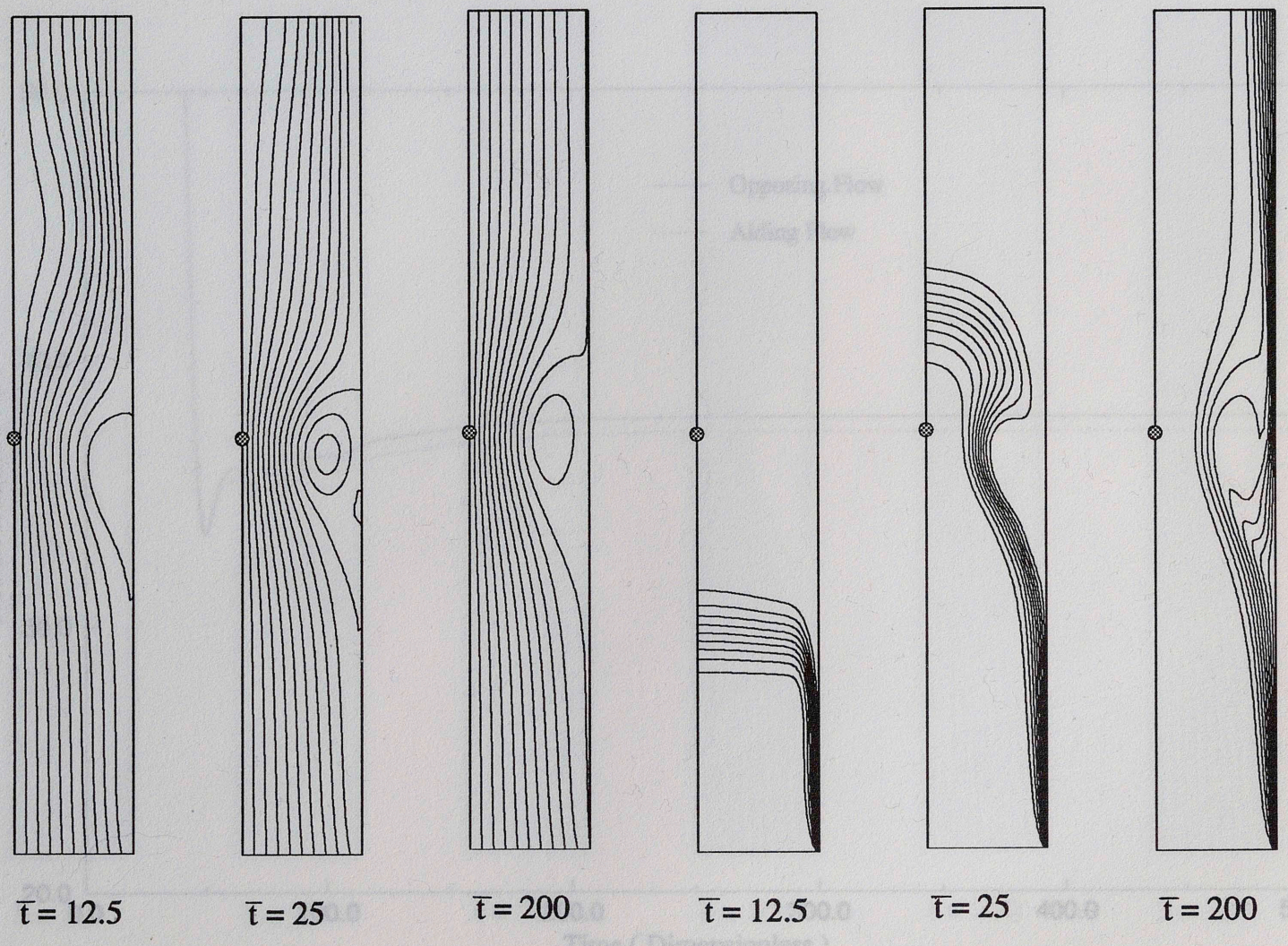

Figure 4.2b Development of Flow and Temperature Field for Forced Convection
(With Electric Field Re = 1800)

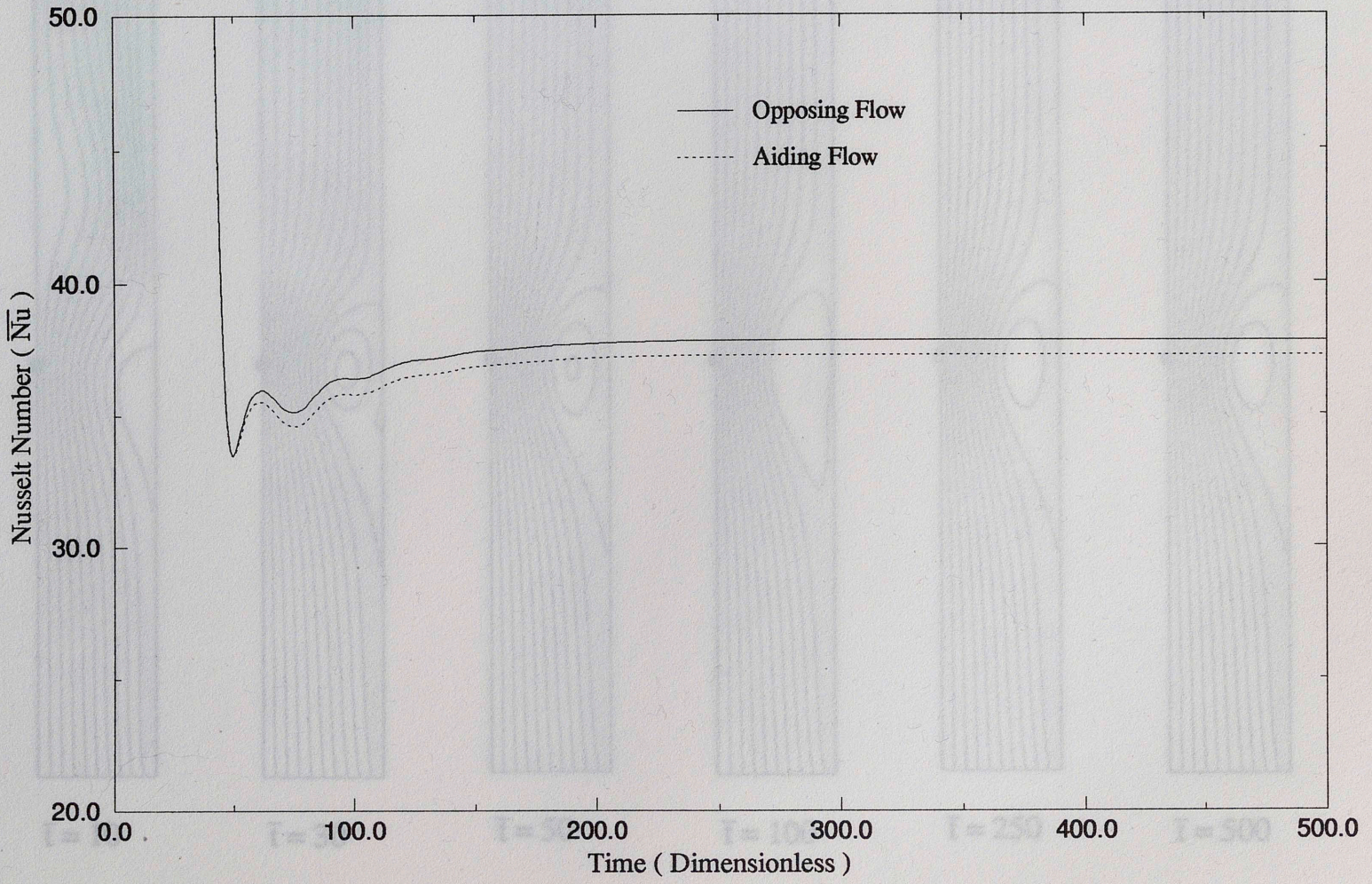

Figure 4.3 Variation of Average Nusselt Number with Time (Re=1800, Gr=10^4)

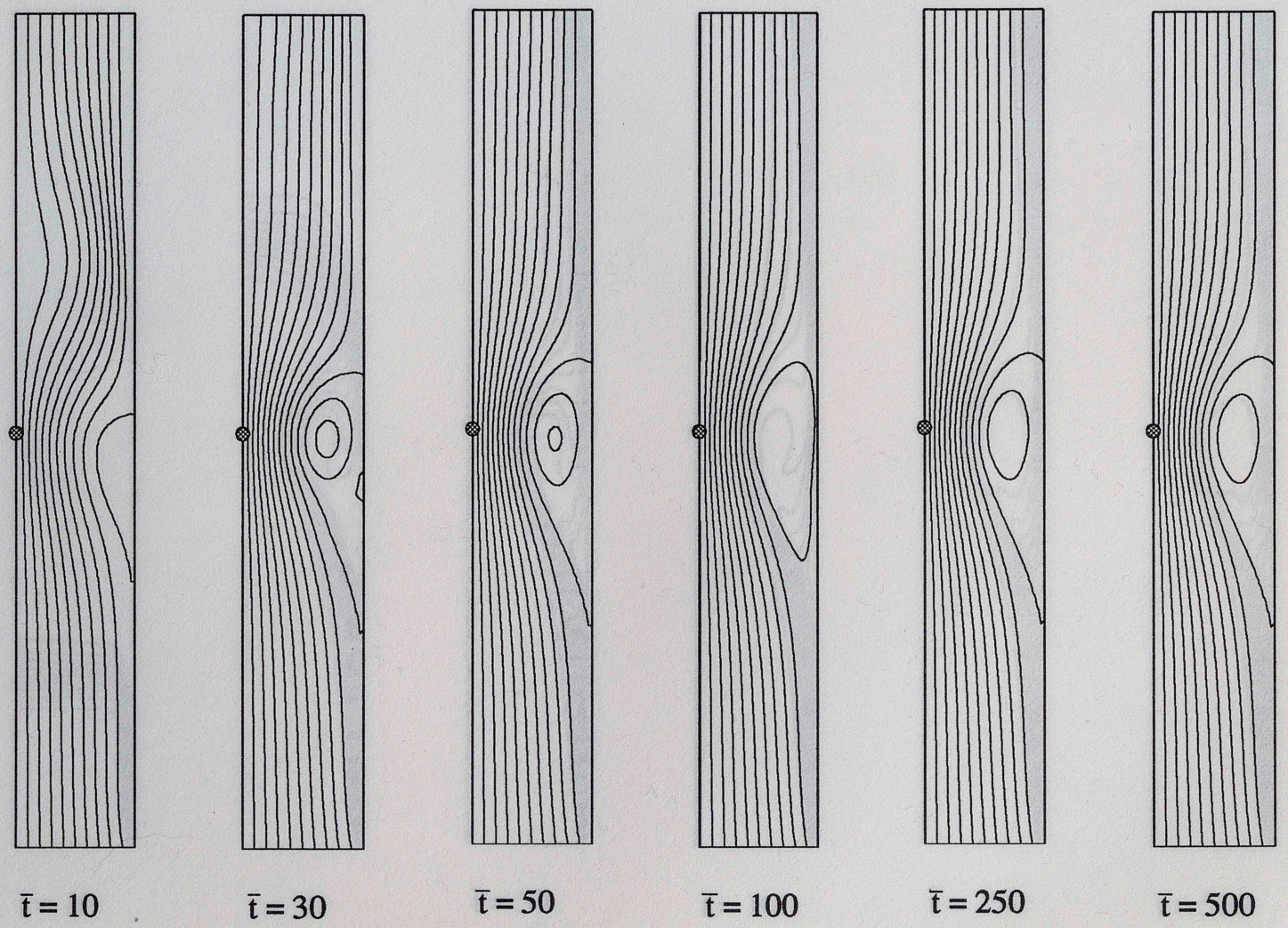

Figure 4.4a Development of Flow Field - Aiding Flow
Re=1800 Gr=10^4 $\Delta\psi = 0.01384$

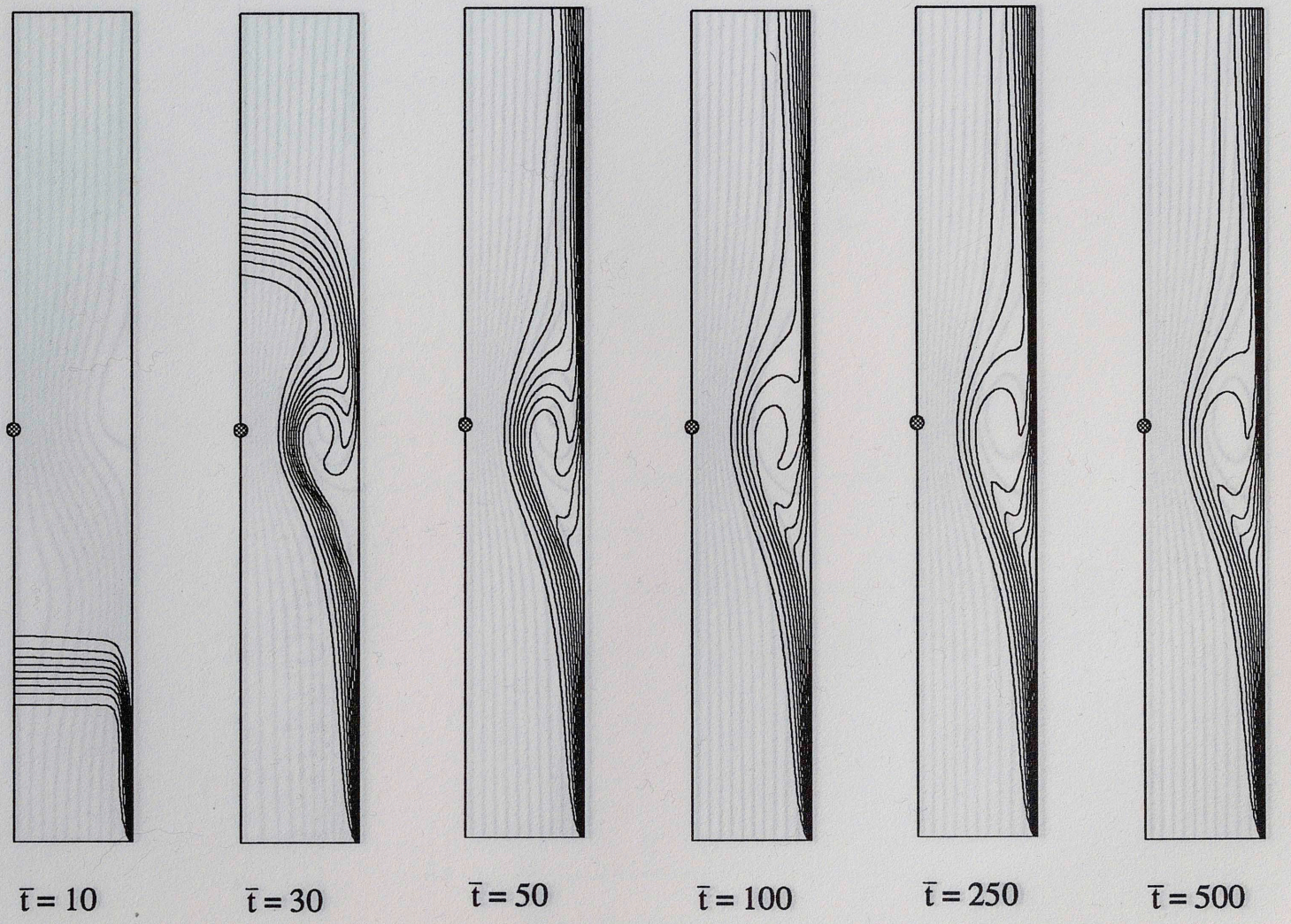

Figure 4.4b Development of Temperature Field - Aiding Flow
Re=1800 Gr=10^4

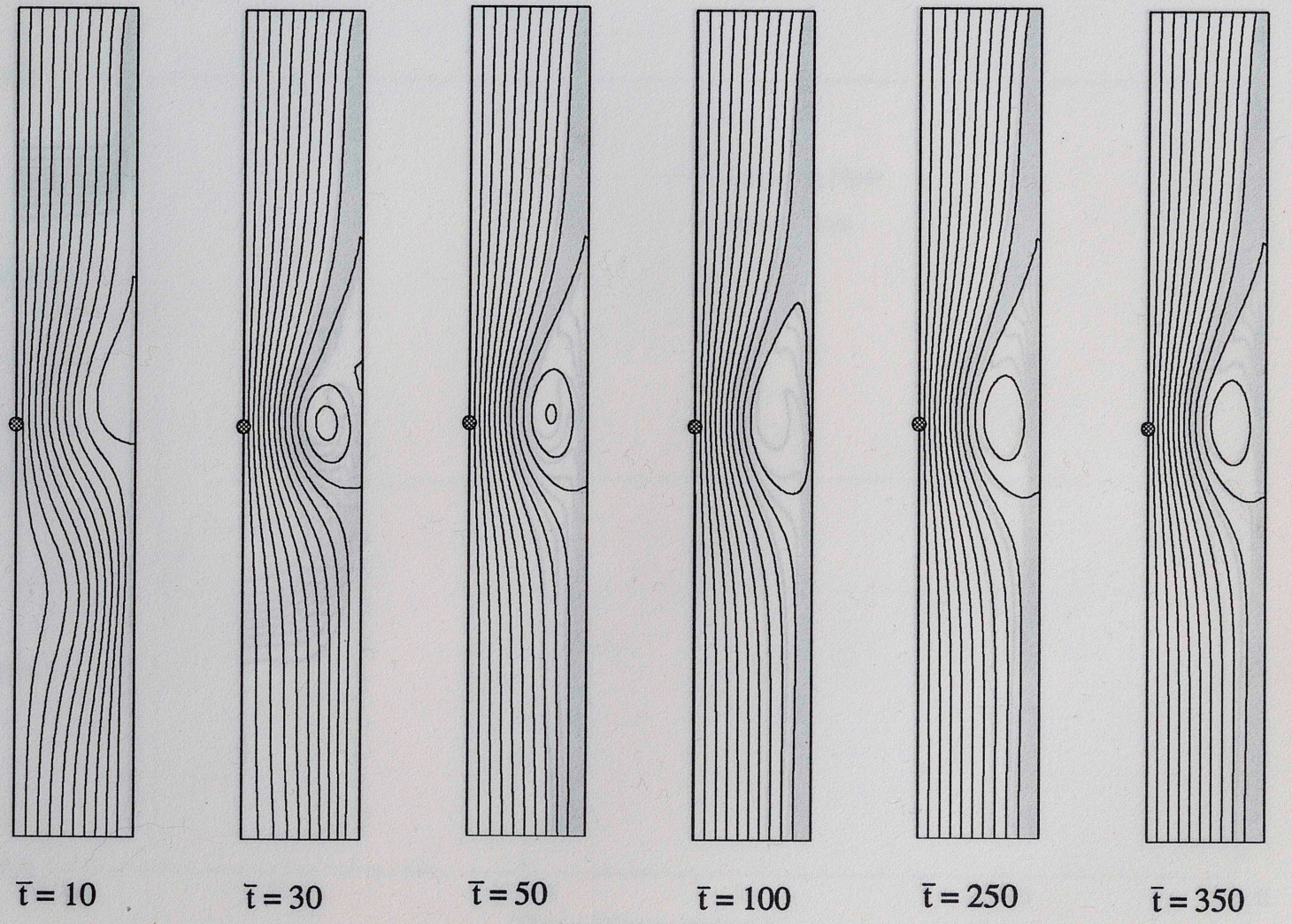

Figure 4.5a Development of Flow Field - Opposing Flow
Re=1800 Gr=10^4 $\Delta\psi = 0.01384$

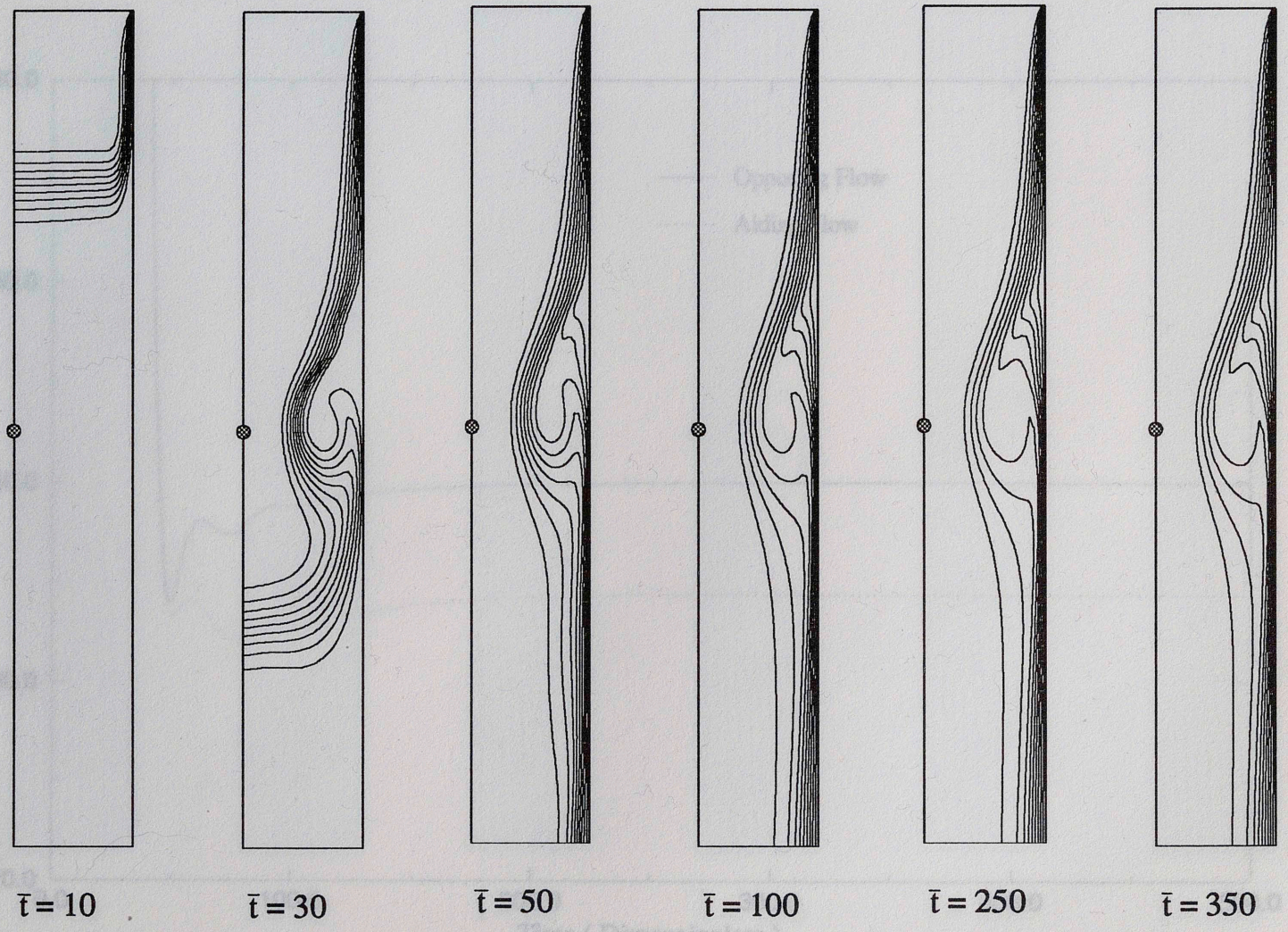

Figure 4.5b Development of Temperature Field - Opposing Flow
Re=1800 Gr=10^4

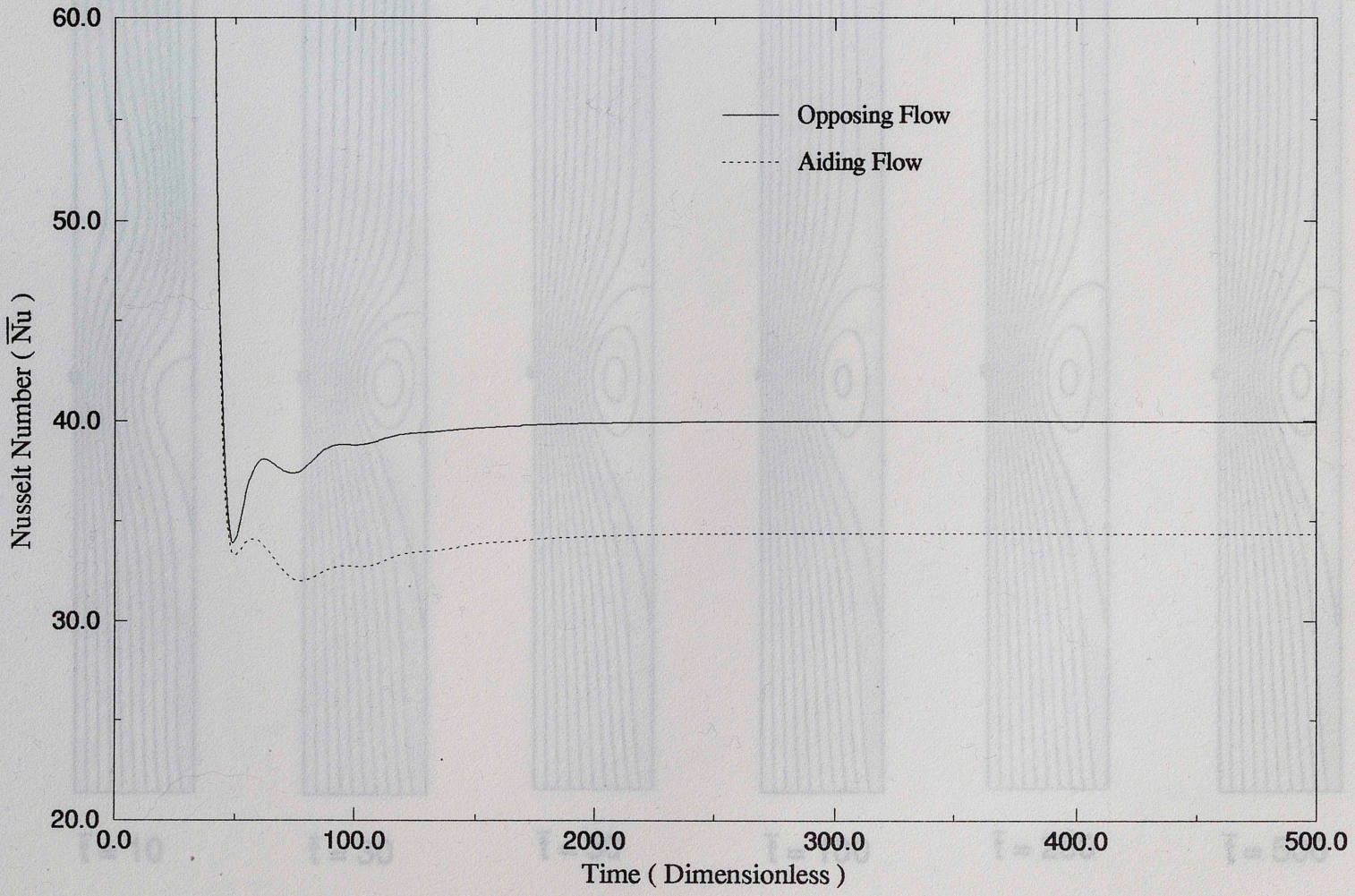

Figure 4.6 Variation of Average Nusselt Number with Time (Re=1800, $Gr=10^5$)

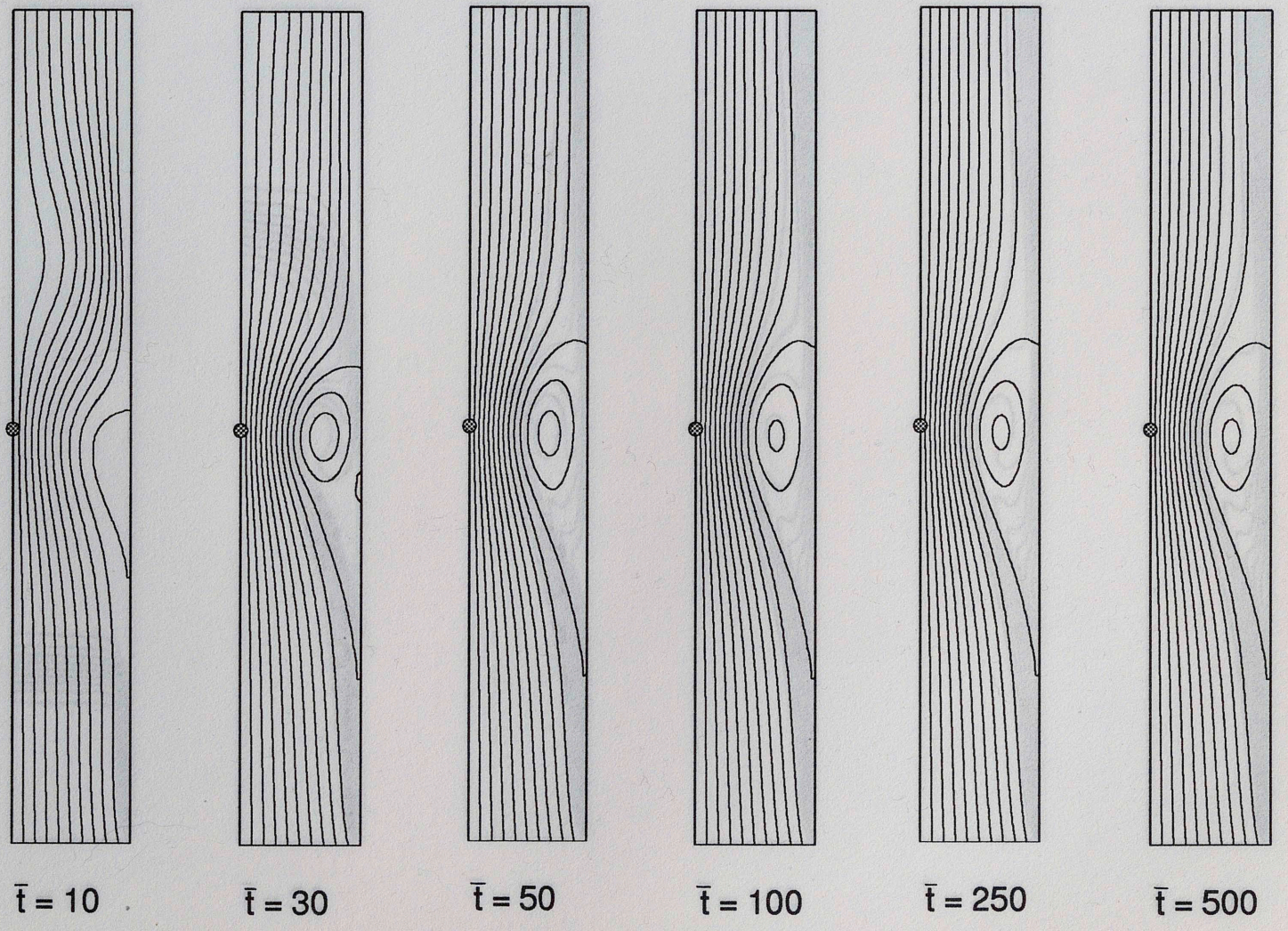

Figure 4.7a Development of Flow Field - Aiding Flow
Re=1800 Gr=10^5 $\Delta\psi$ = 0.01384

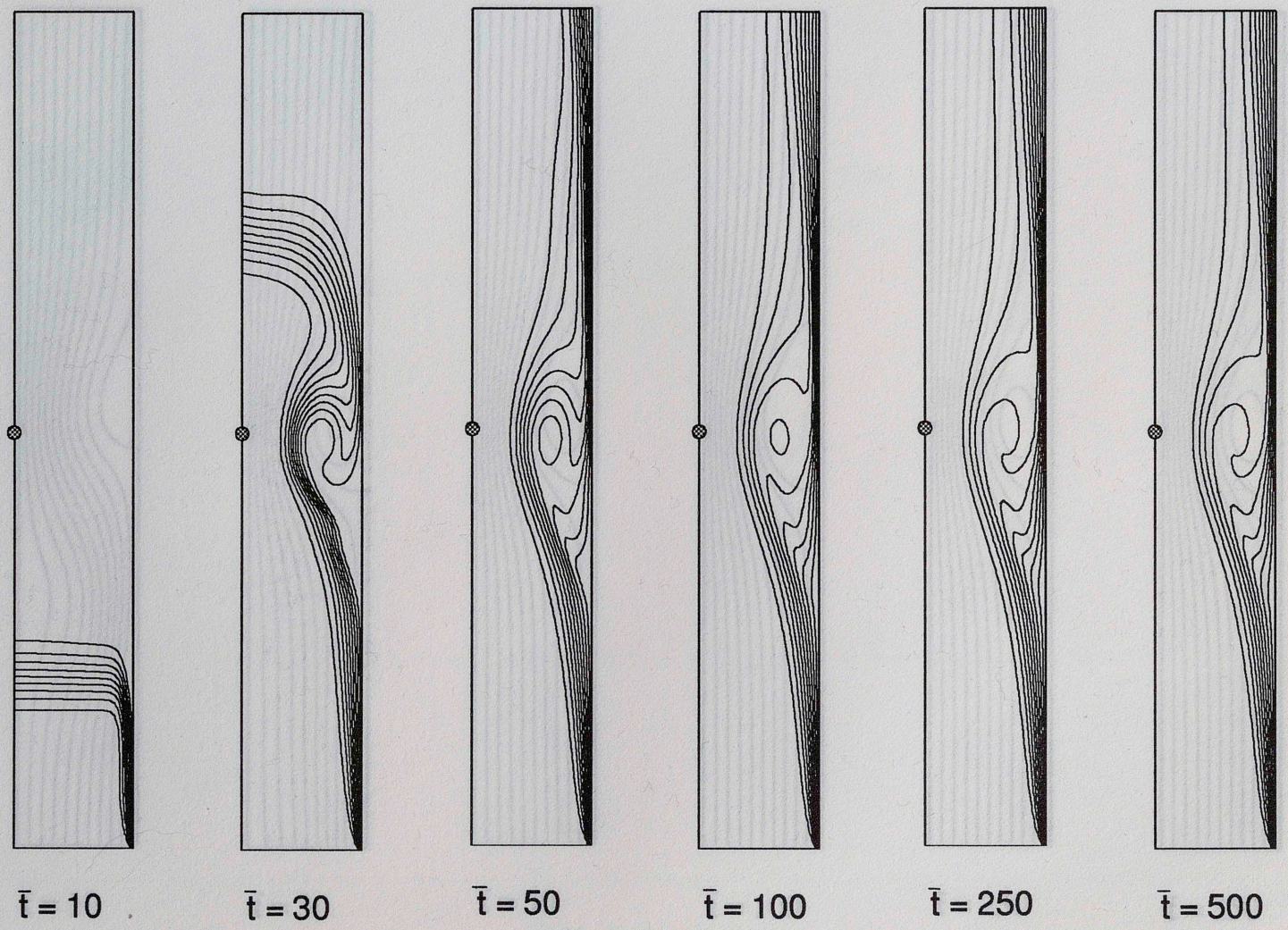

Figure 4.7b Development of Temeprature Field - Aiding Flow
Re=1800 Gr=10^5

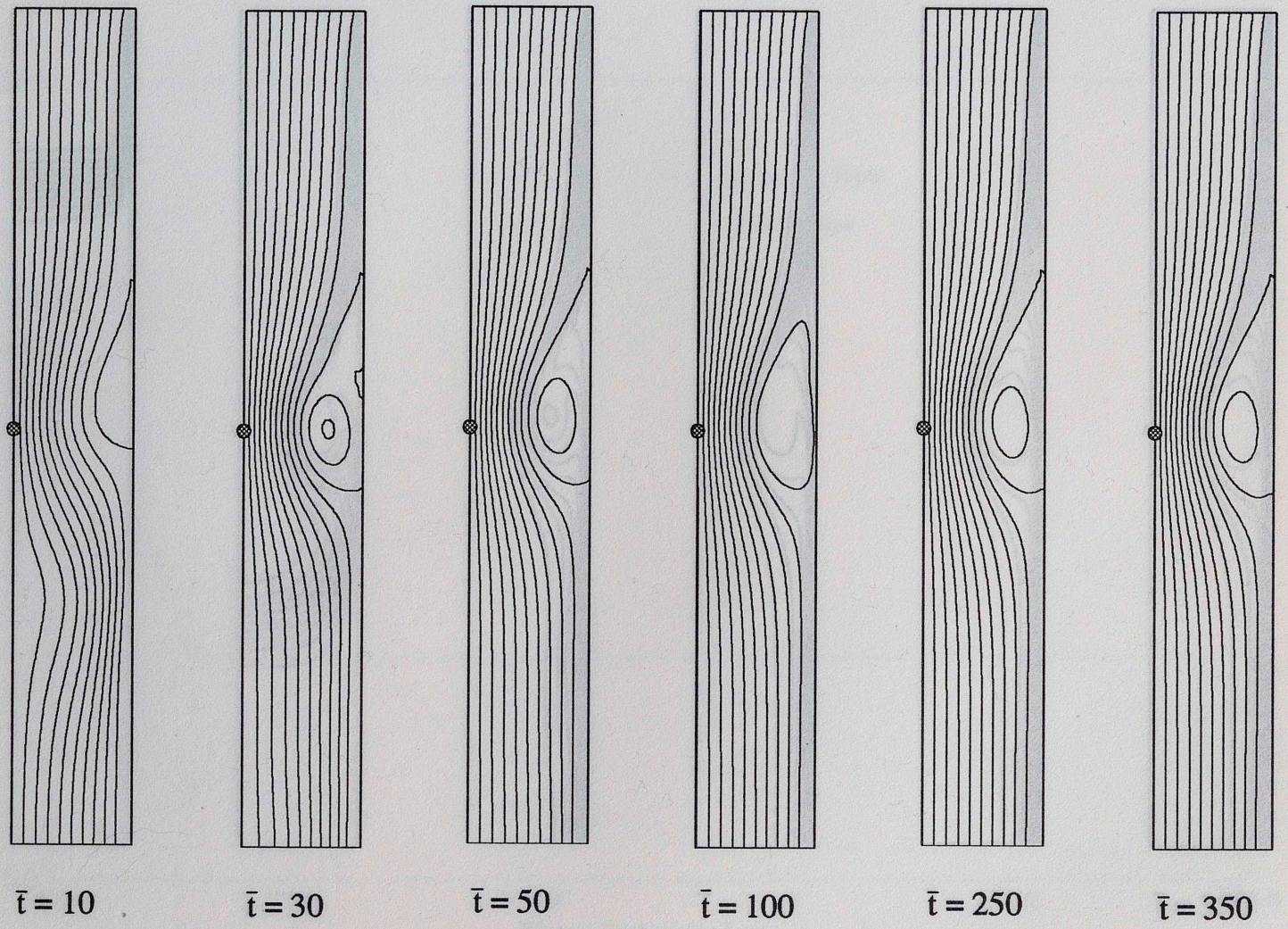

Figure 4.8a Development of Flow Field - Opposing Flow
Re=1800 Gr=10^5 $\Delta\psi = 0.01384$

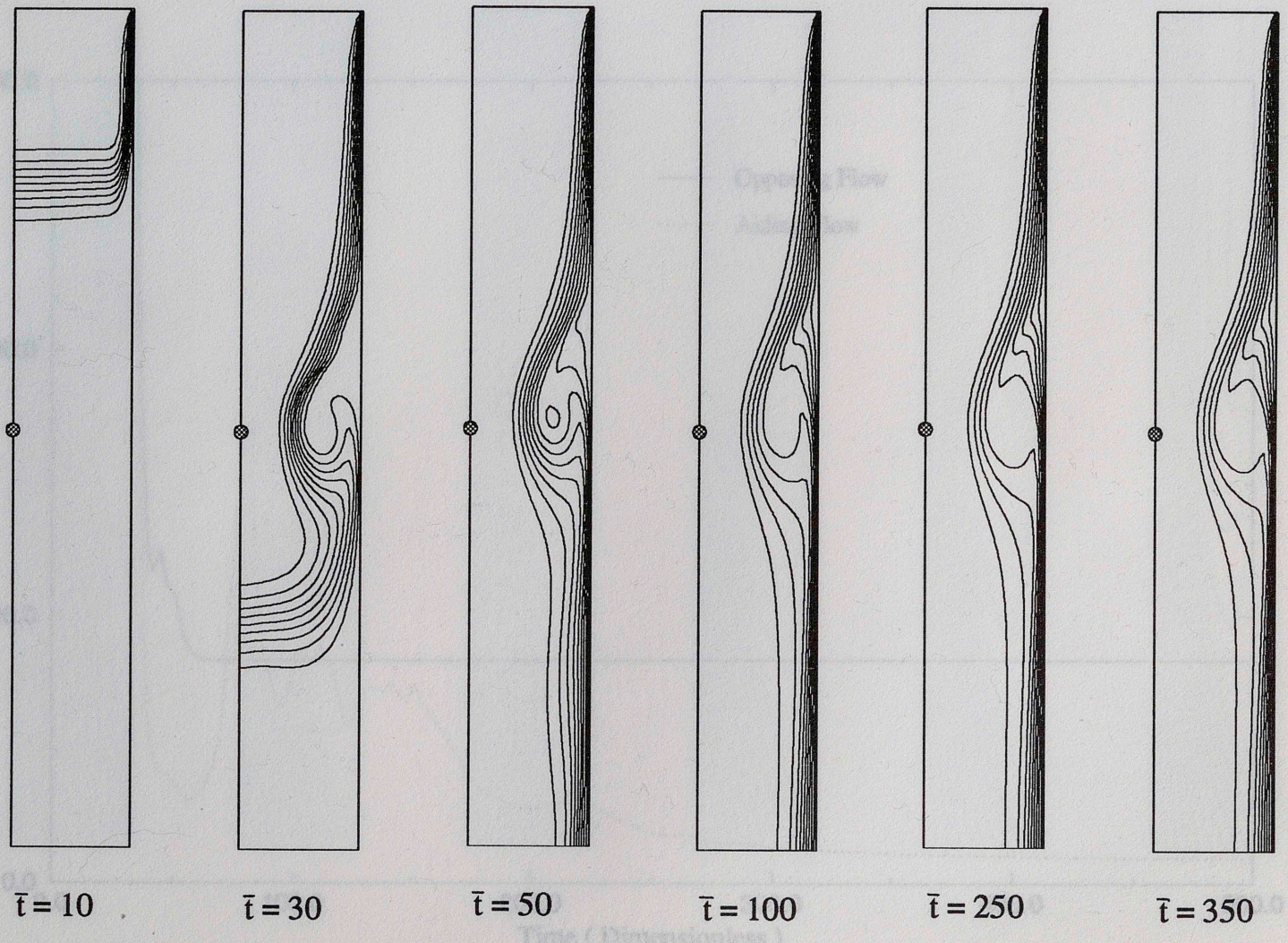

Figure 4.8b Development of Temperature Field - Opposing Flow
Re=1800 Gr=10^5

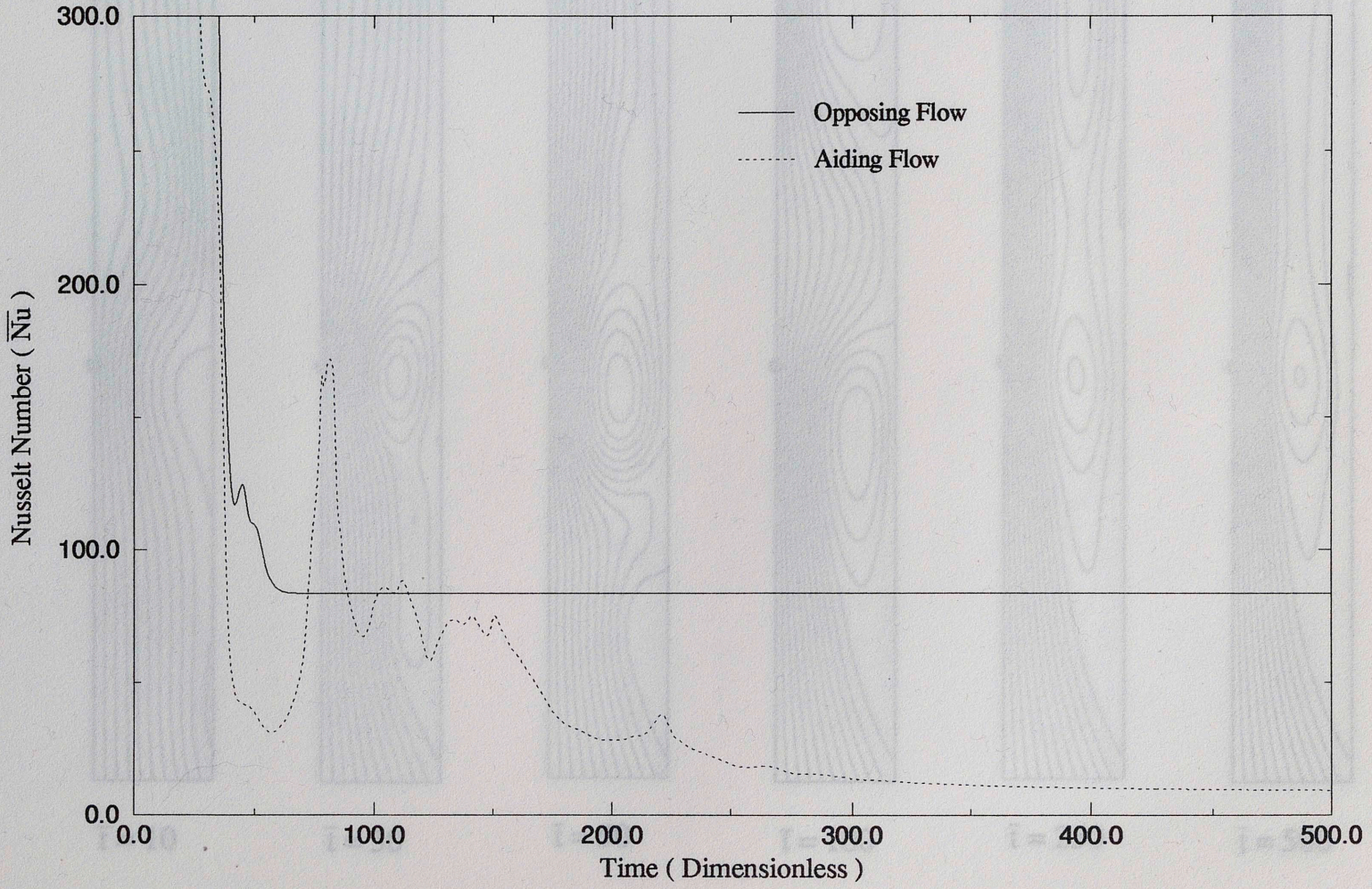

Figure 4.9 Variation of Nusselt Number with Time (Re=1800, Gr=10^6)

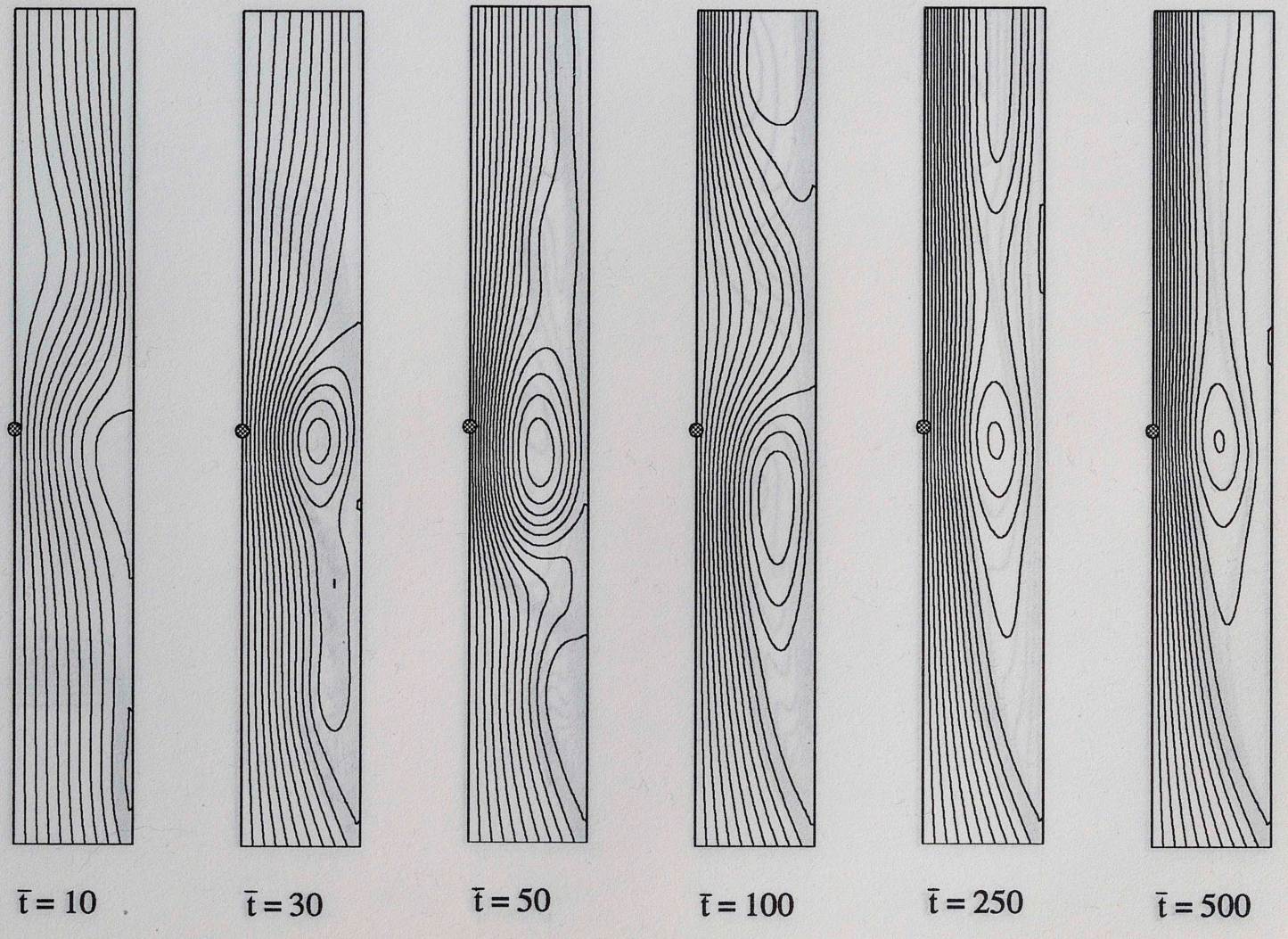

Figure 4.10a Development of Flow Field - Aiding Flow
Re=1800 Gr=10^6 $\Delta\psi = 0.01384$

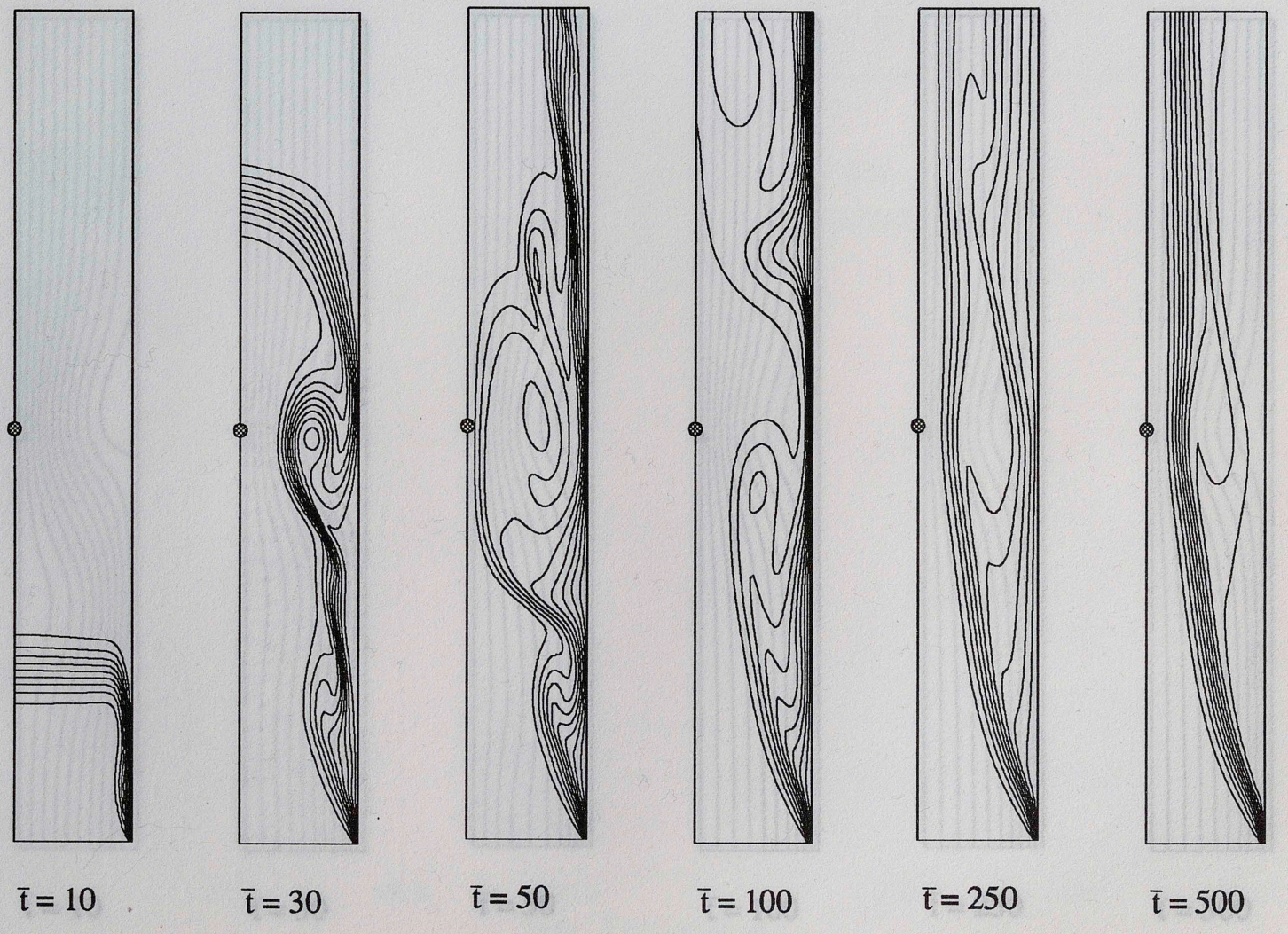

Figure 4.10b Development of Temperature Field - Aiding Flow
Re=1800 Gr=10^6

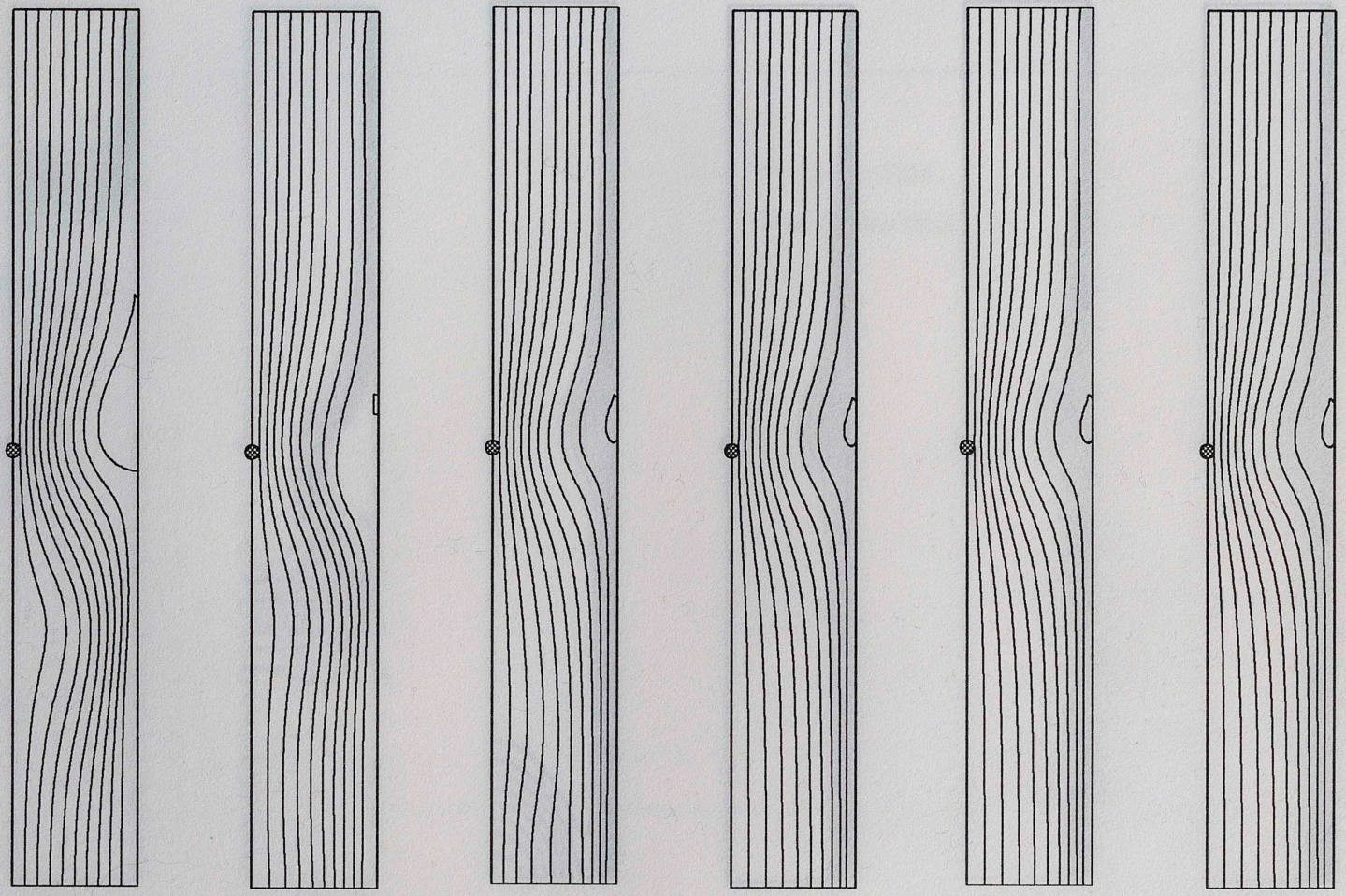

Figure 4.11a Development of Flow Field - Opposing Flow
Re=1800 Gr=10^6 $\Delta\psi = 0.01384$

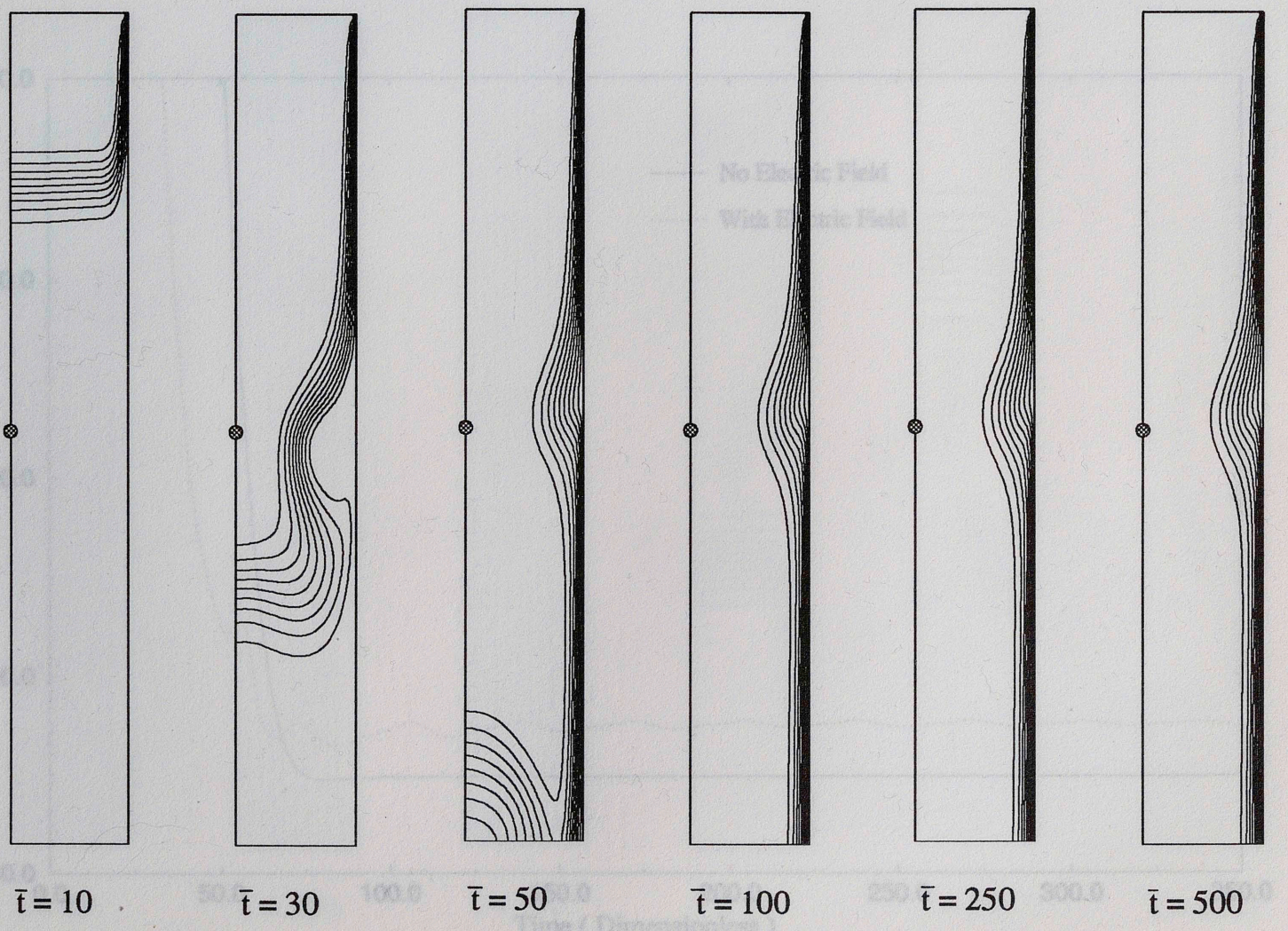

Figure 4.11b Development of Temperature Field - Opposing Flow
Re=1800 Gr=10^6

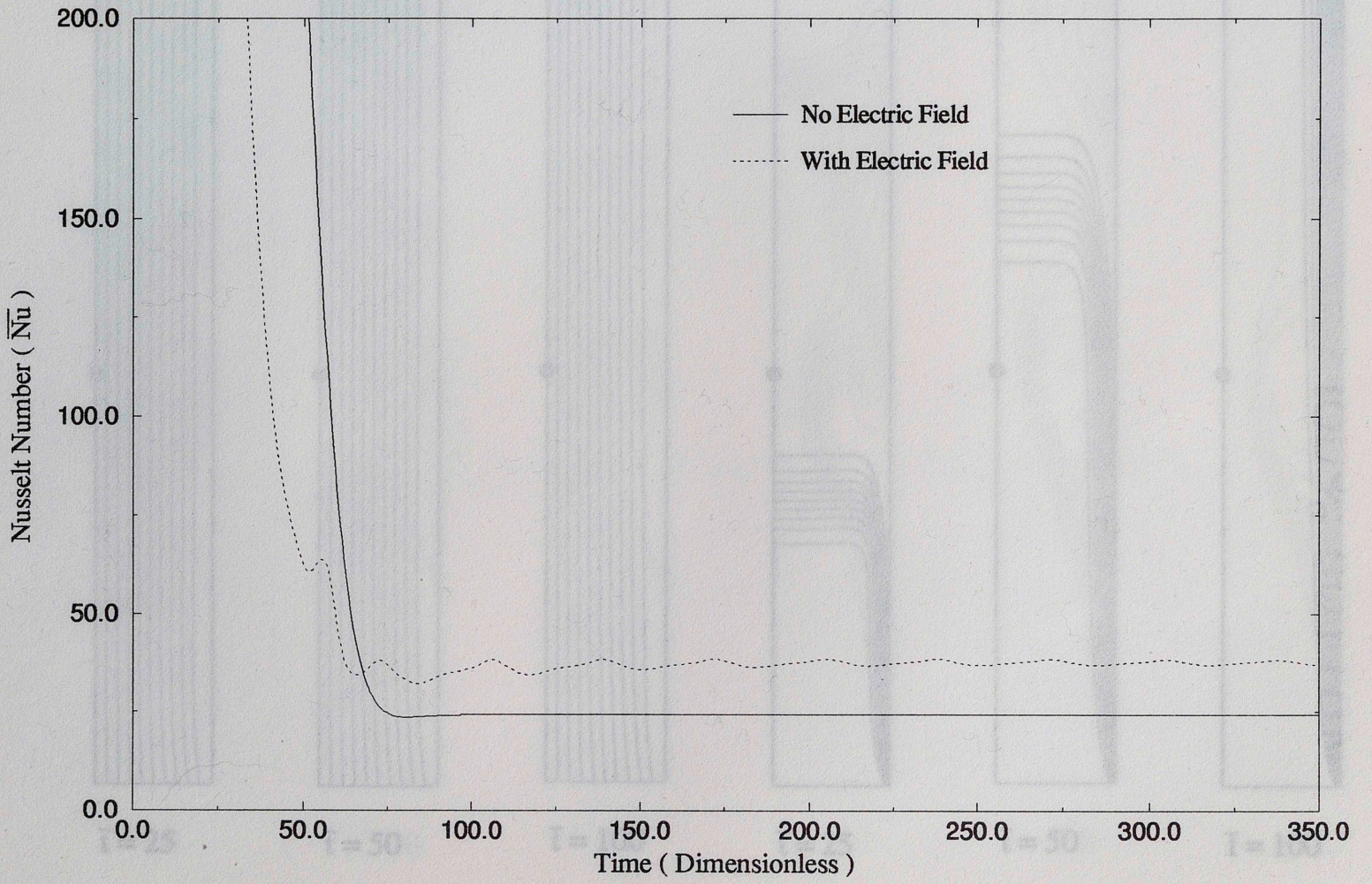

Figure 4.12 Variation of Average Nusselt Number with Time for Forced Convection (Re=1200)

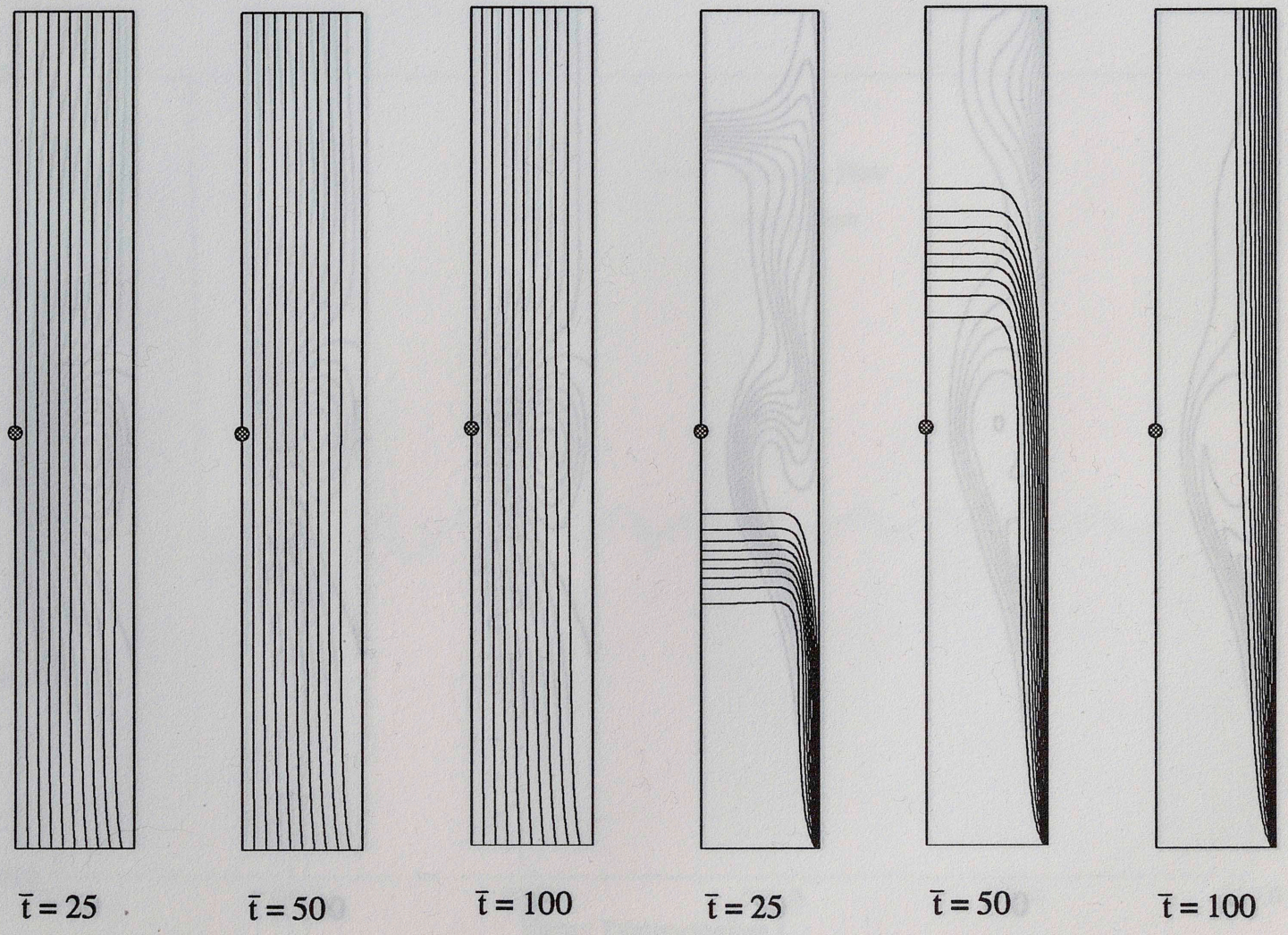

Figure 4.13a Development of Flow and Temperature Field for Forced Convection
(Without Electric Field Re =1200)

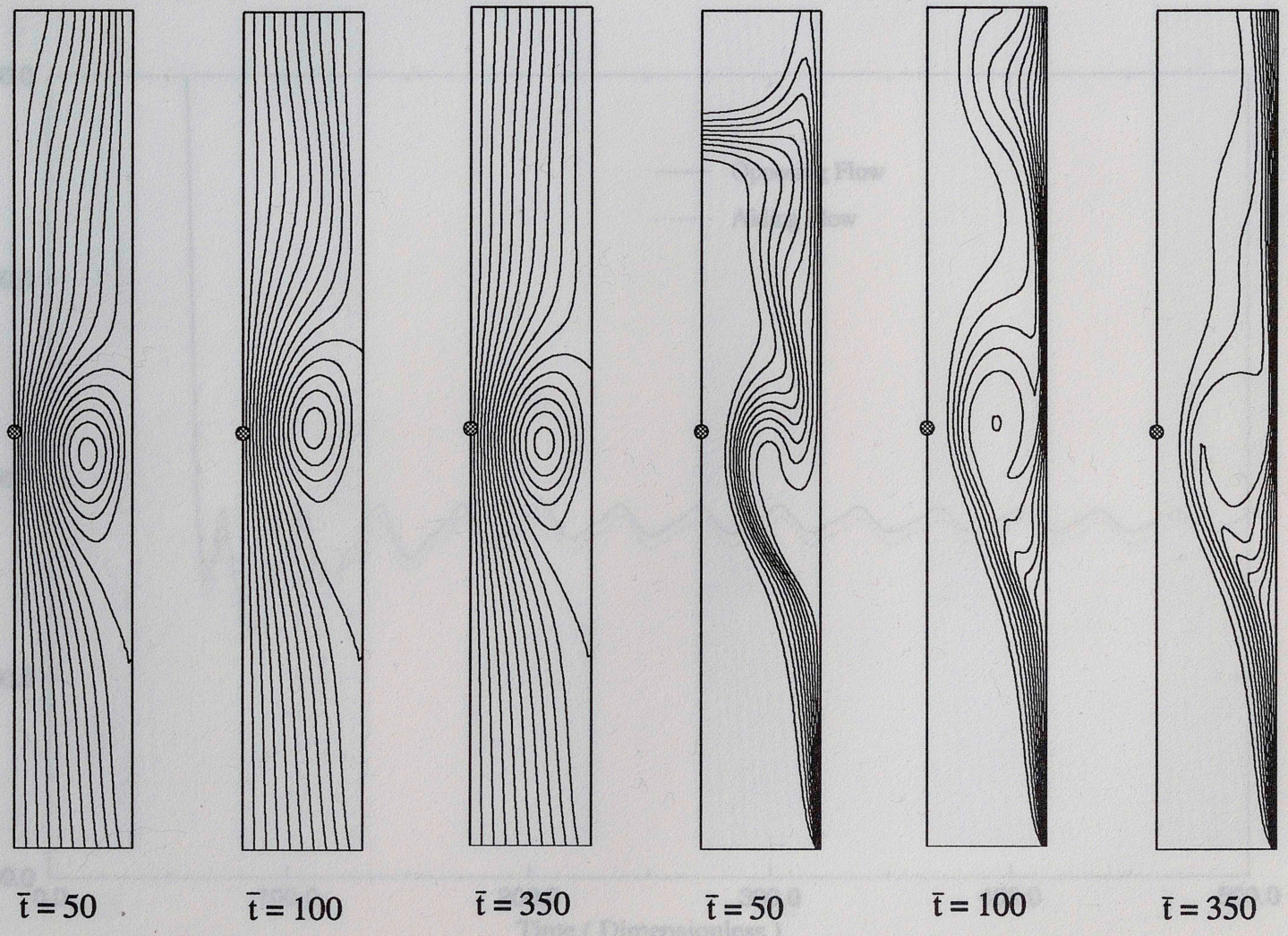

Figure 4.13b Development of Flow and Temperature Field for Forced Convection
(With Electric Field Re = 1200)

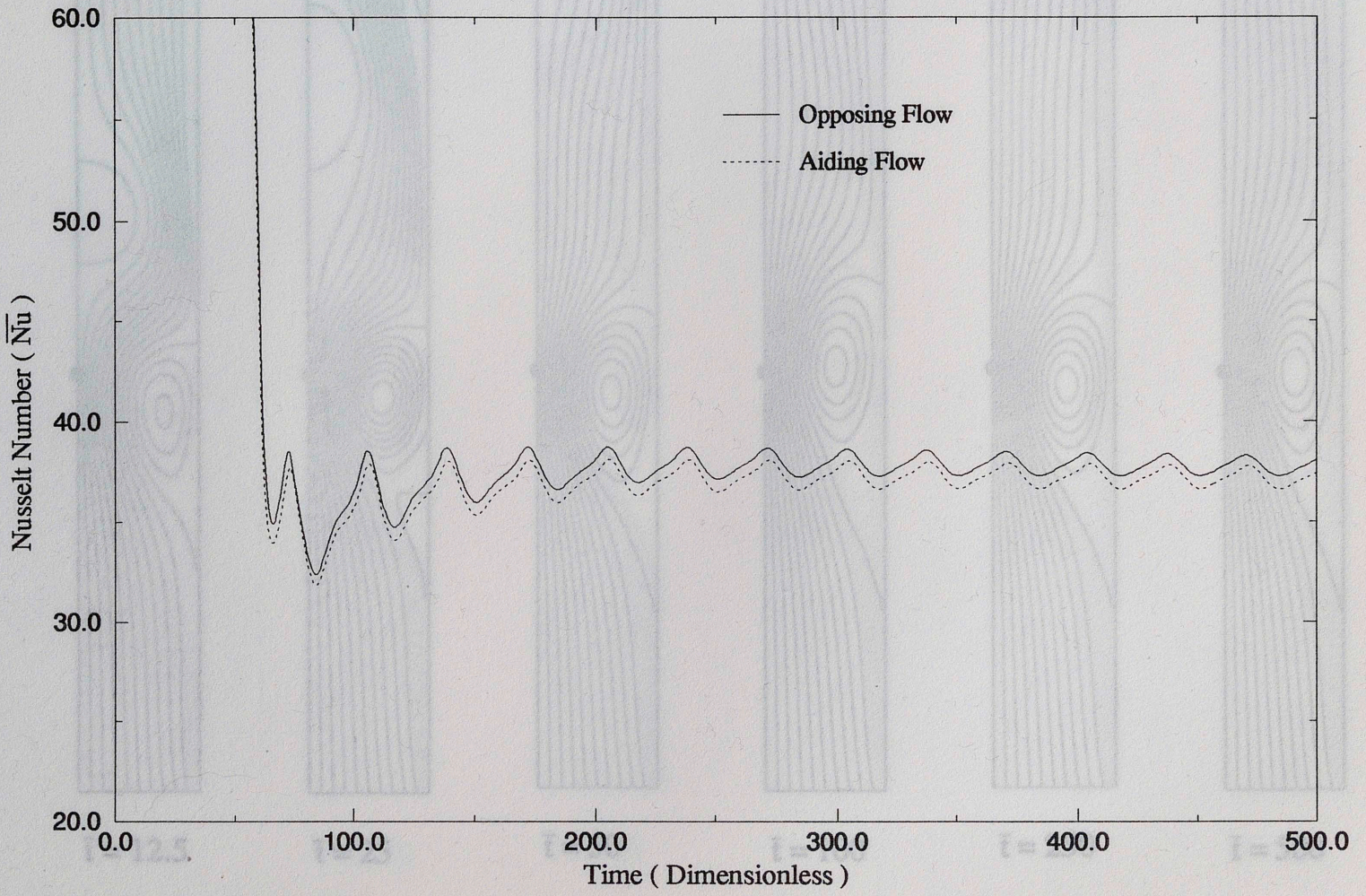

Figure 4.14 Variation of Nusselt Number with Time (Re=1200, Gr=10^4)

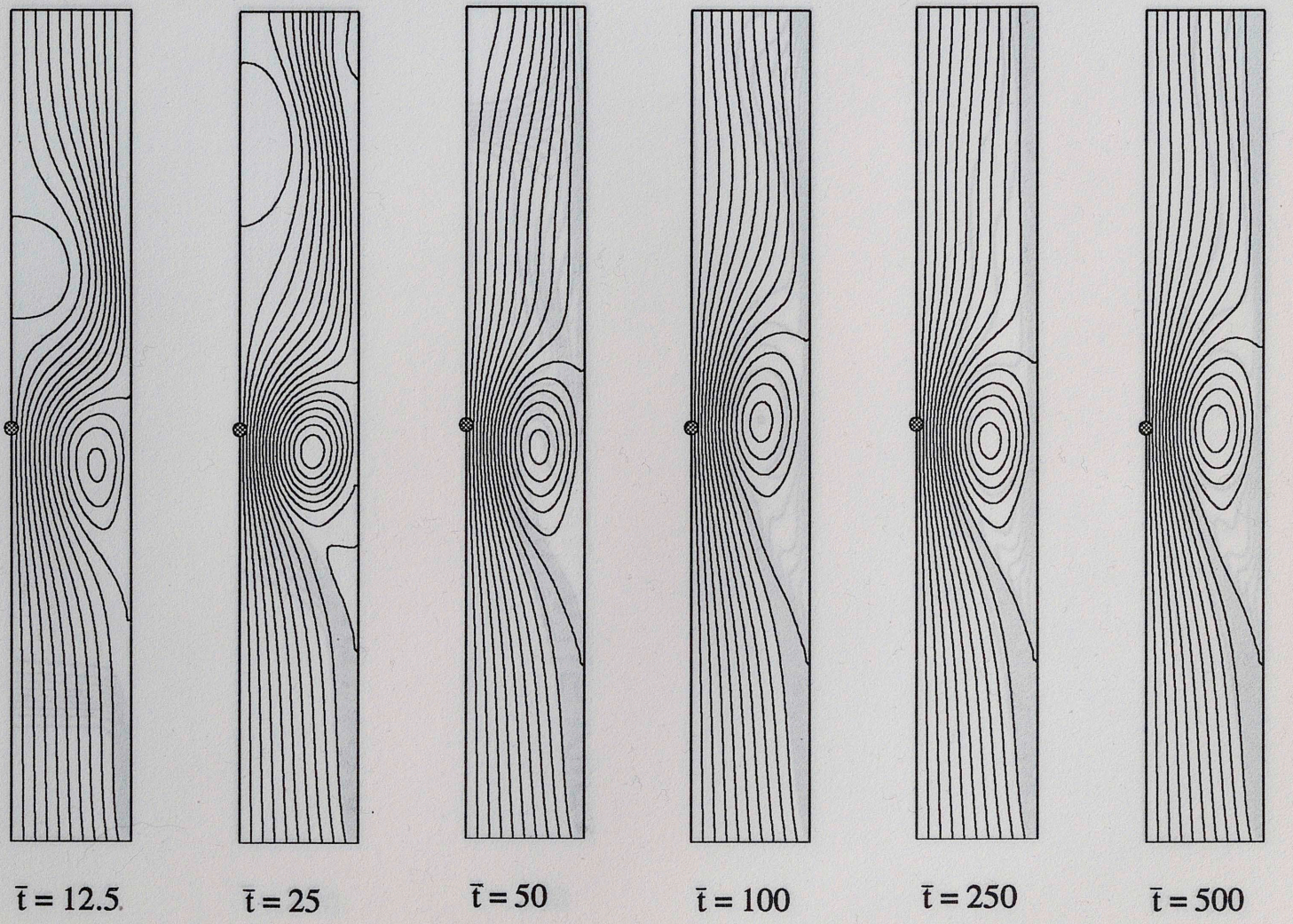

Figure 4.15a Development of Flow Field - Aiding Flow
Re=1200 Gr=10^4 $\Delta\psi$ = 0.009229

Figure 4.15b Development of Temperature Field - Aiding Flow
Re=1200 Gr=10^4

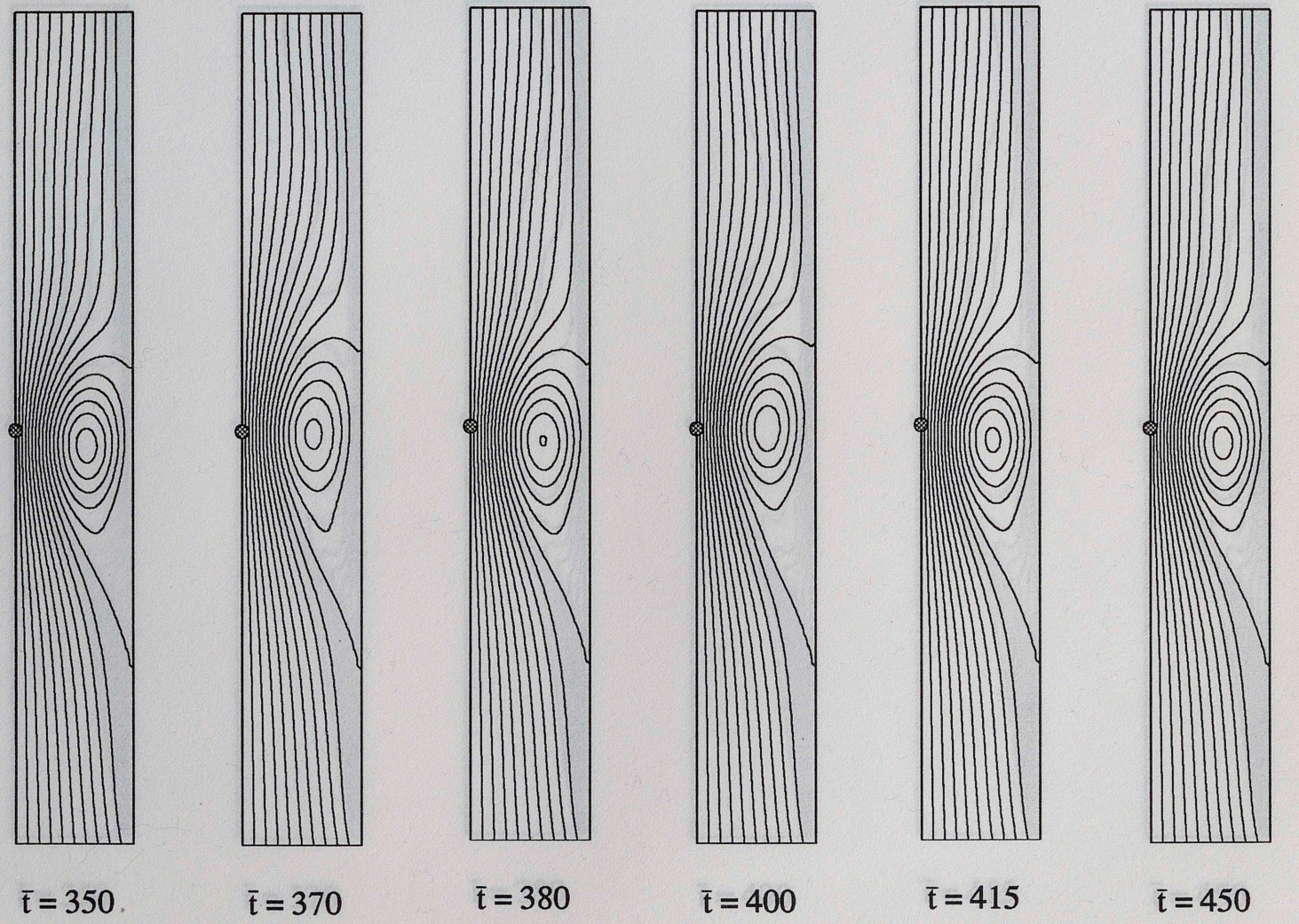

Figure 4.15c Development of Flow Field - Aiding Flow (Two Periods)
Re=1200 Gr=10^4 $\Delta\psi$ = 0.009229

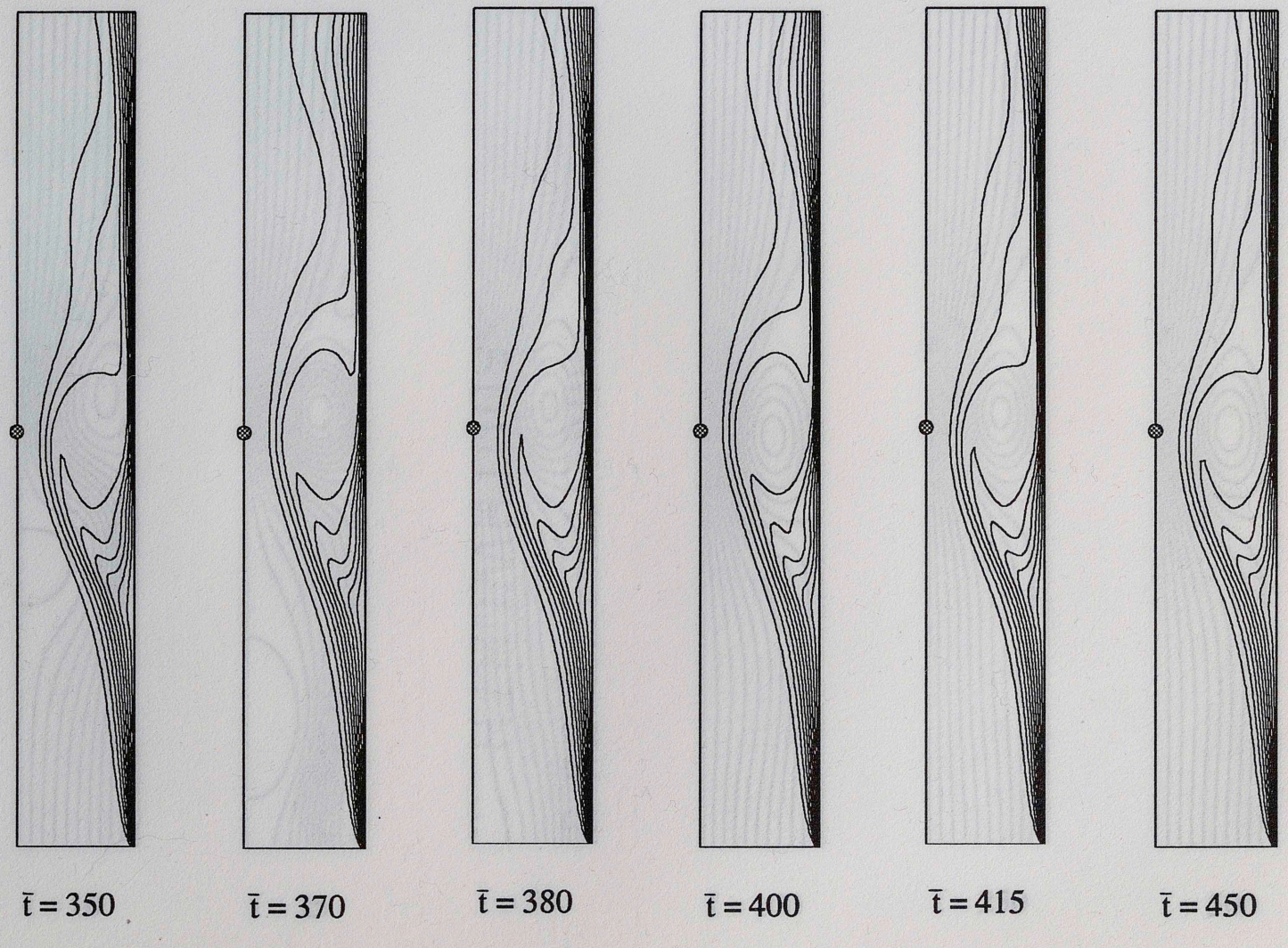

Figure 4.15d Development of Temperature Field - Aiding Flow (Two Periods)
Re=1200 Gr=10^4

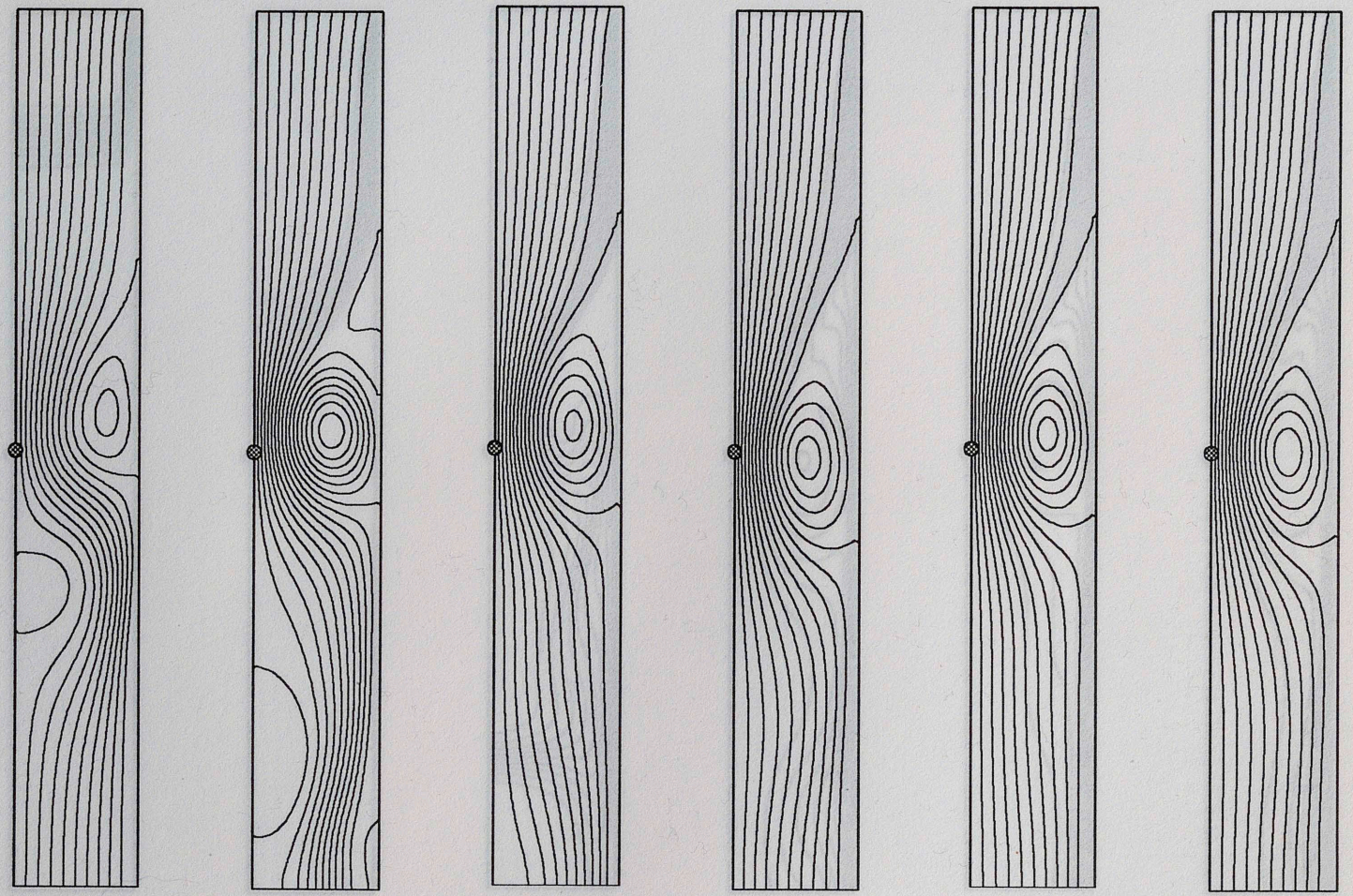

Figure 4.16a Development of Flow Field - Opposing Flow
Re=1200 Gr=10^4 $\Delta\psi = 0.009229$

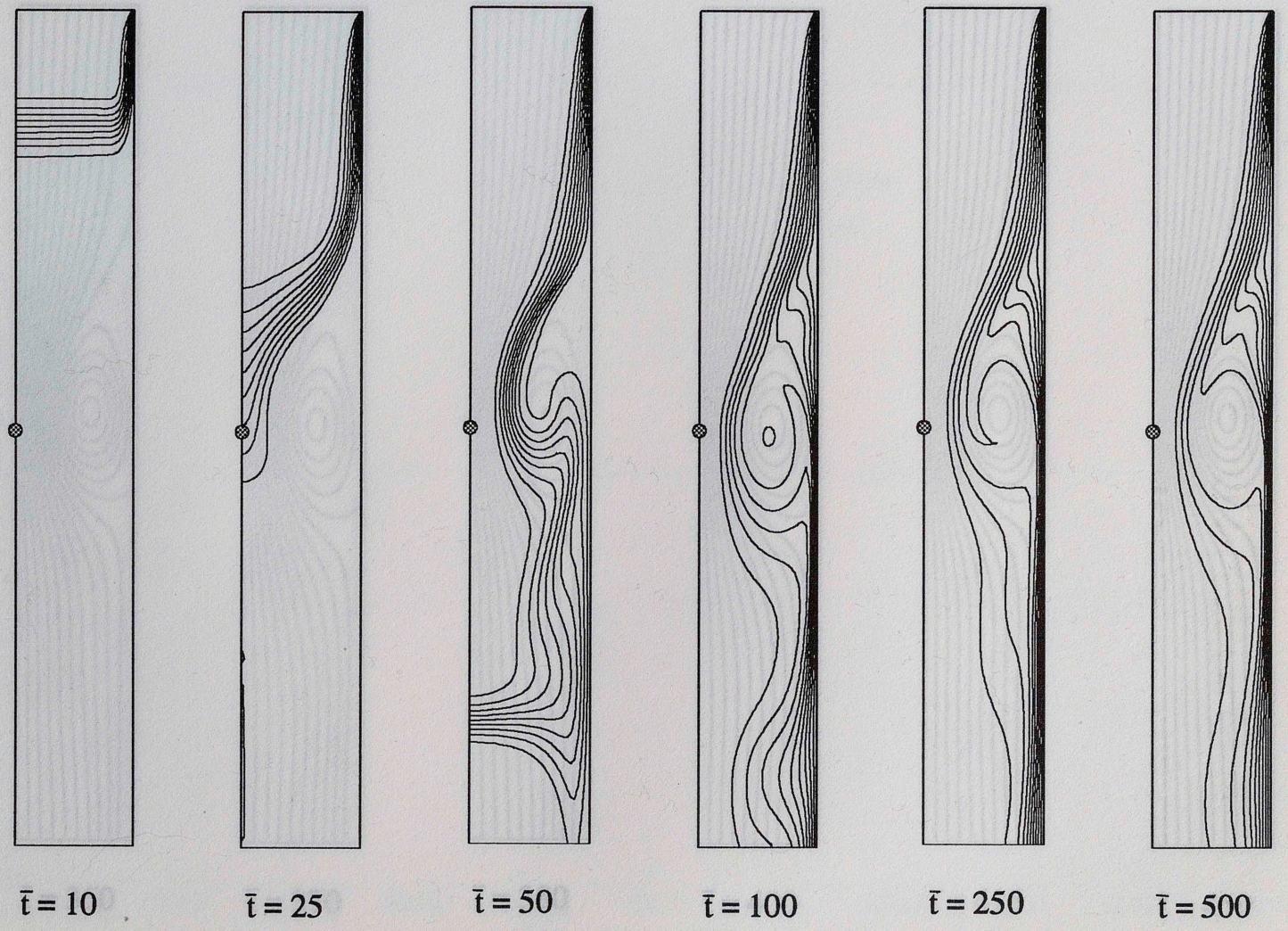

Figure 4.16b Development of Temperature Field - Opposing Flow
Re=1200 Gr=10^4

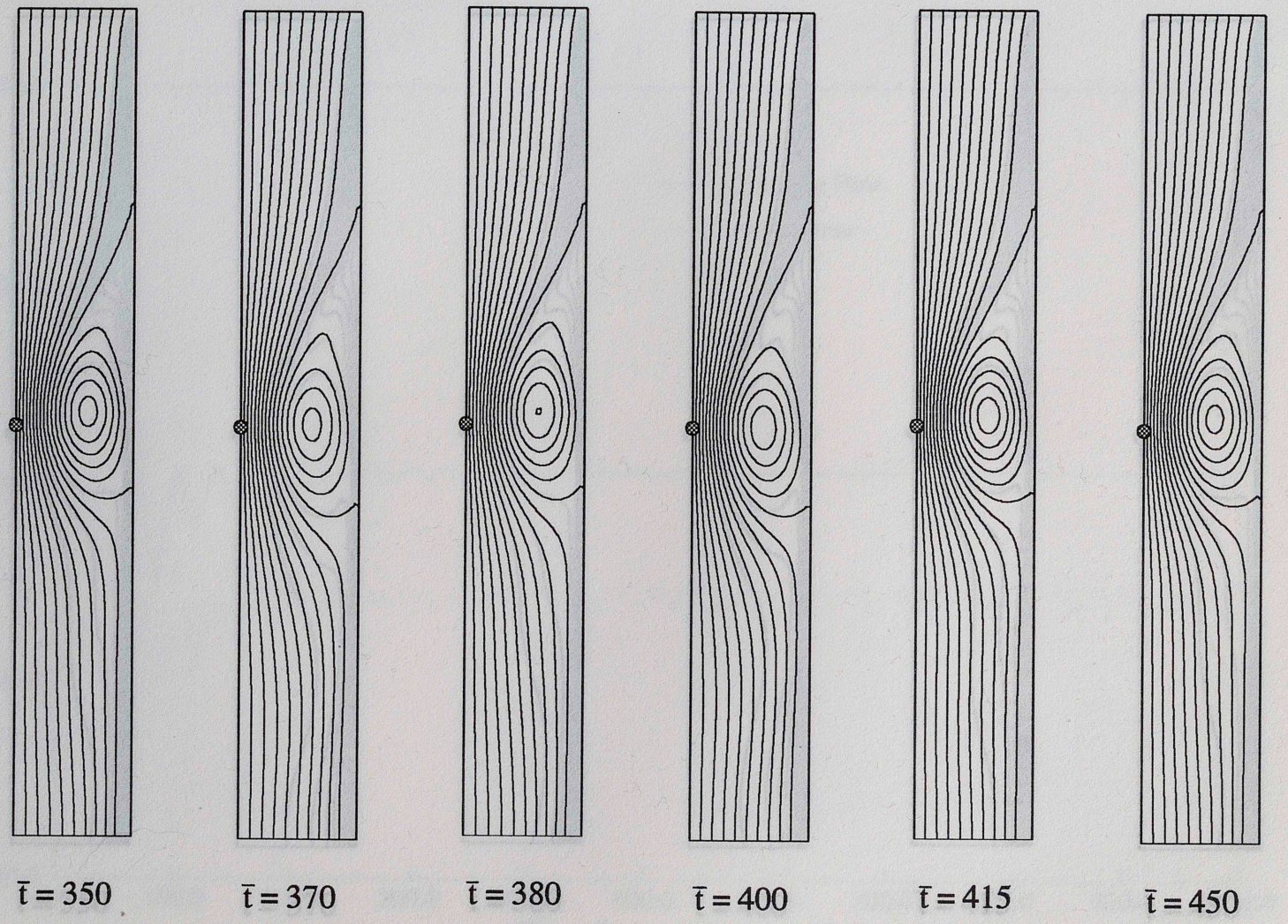

Figure 4.16c Development of Flow Field - Opposing Flow (Two Periods)
Re=1200 Gr=10^4 $\Delta\psi = 0.009229$

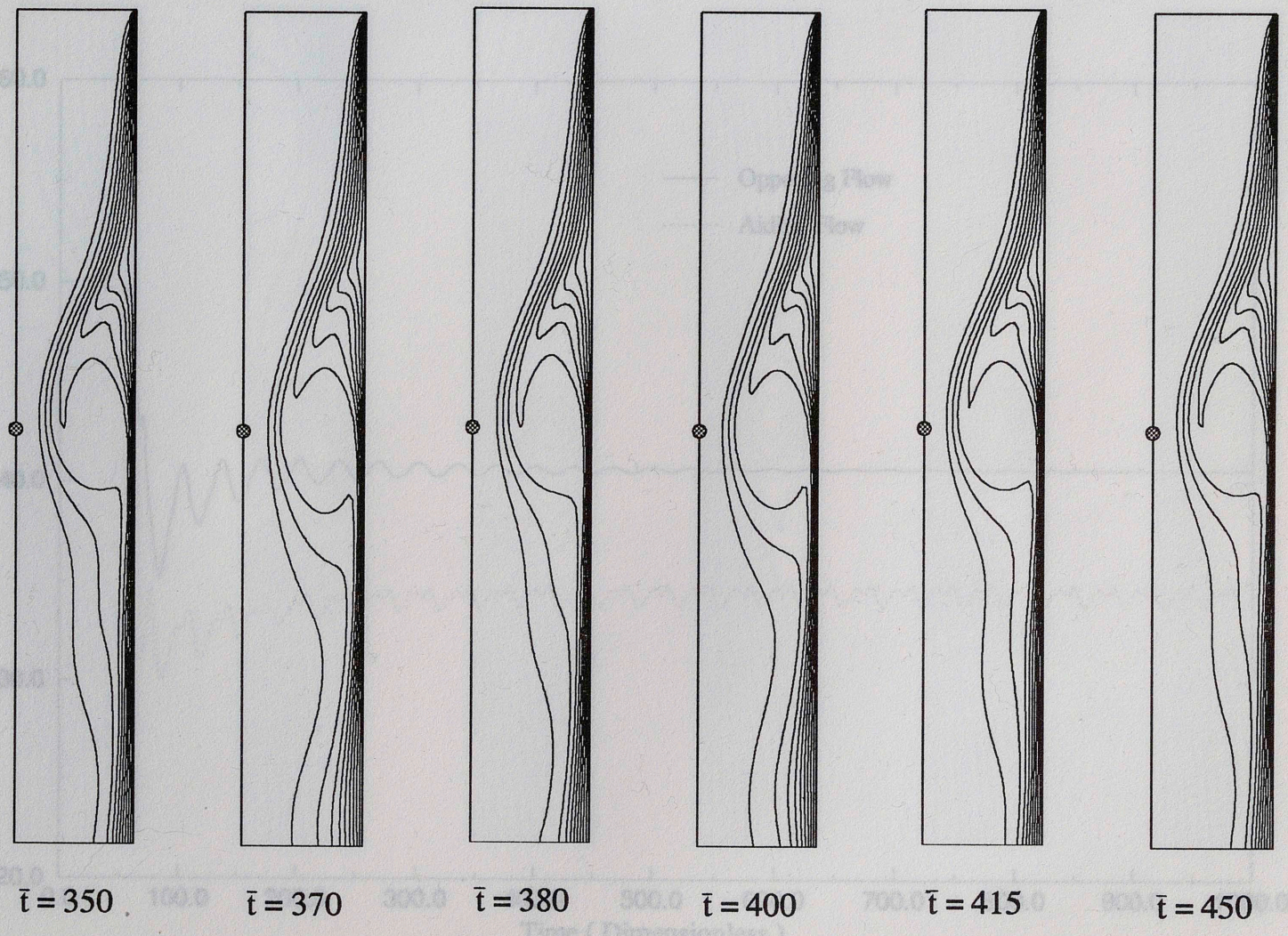

Figure 4.16d Development of Temperature Field - Opposing Flow (Two Periods)
Re=1200 Gr=10^4

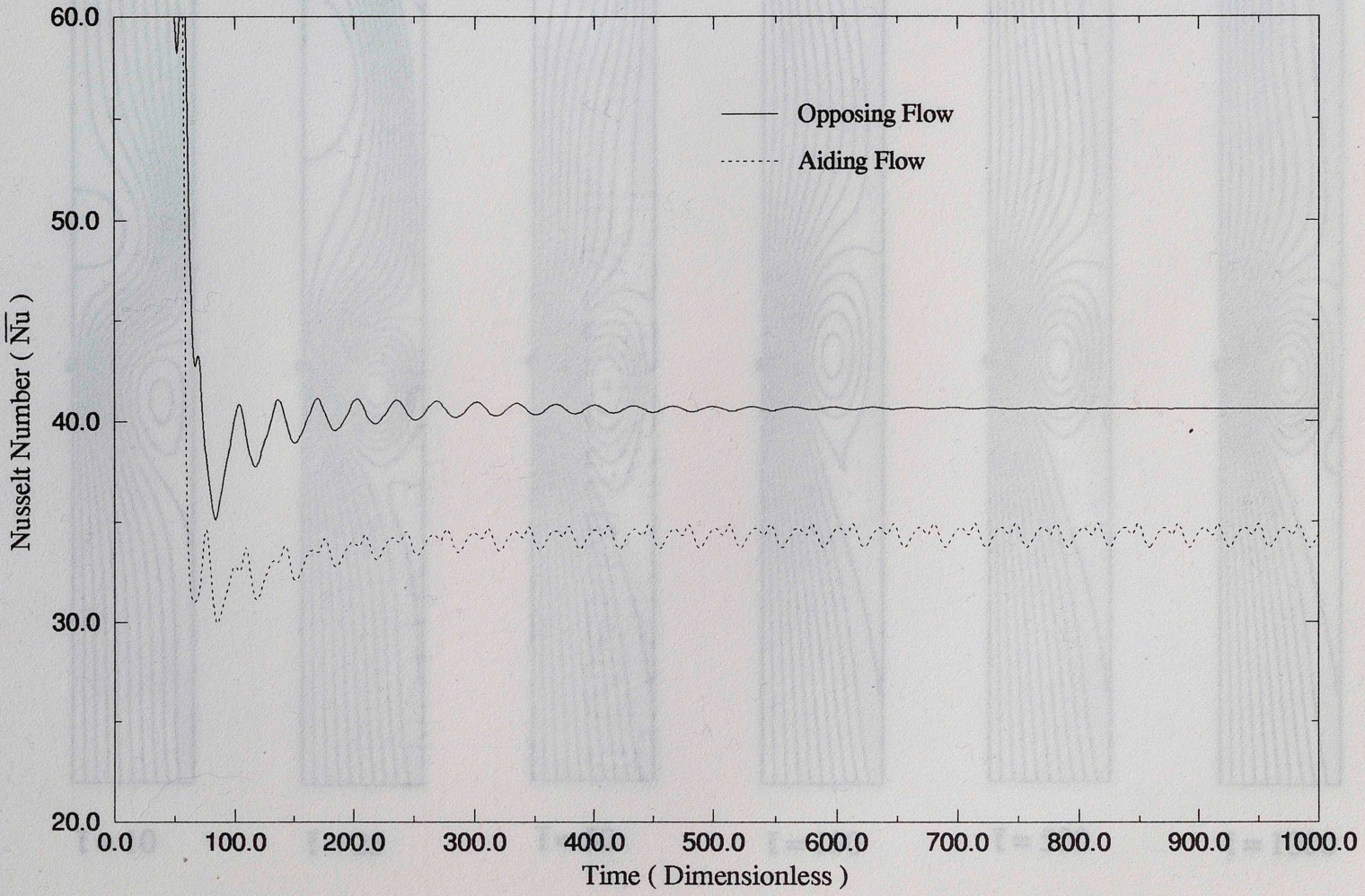

Figure 4.17 Variation of Average Nusselt Number with Time (Re=1200, Gr=10^5)

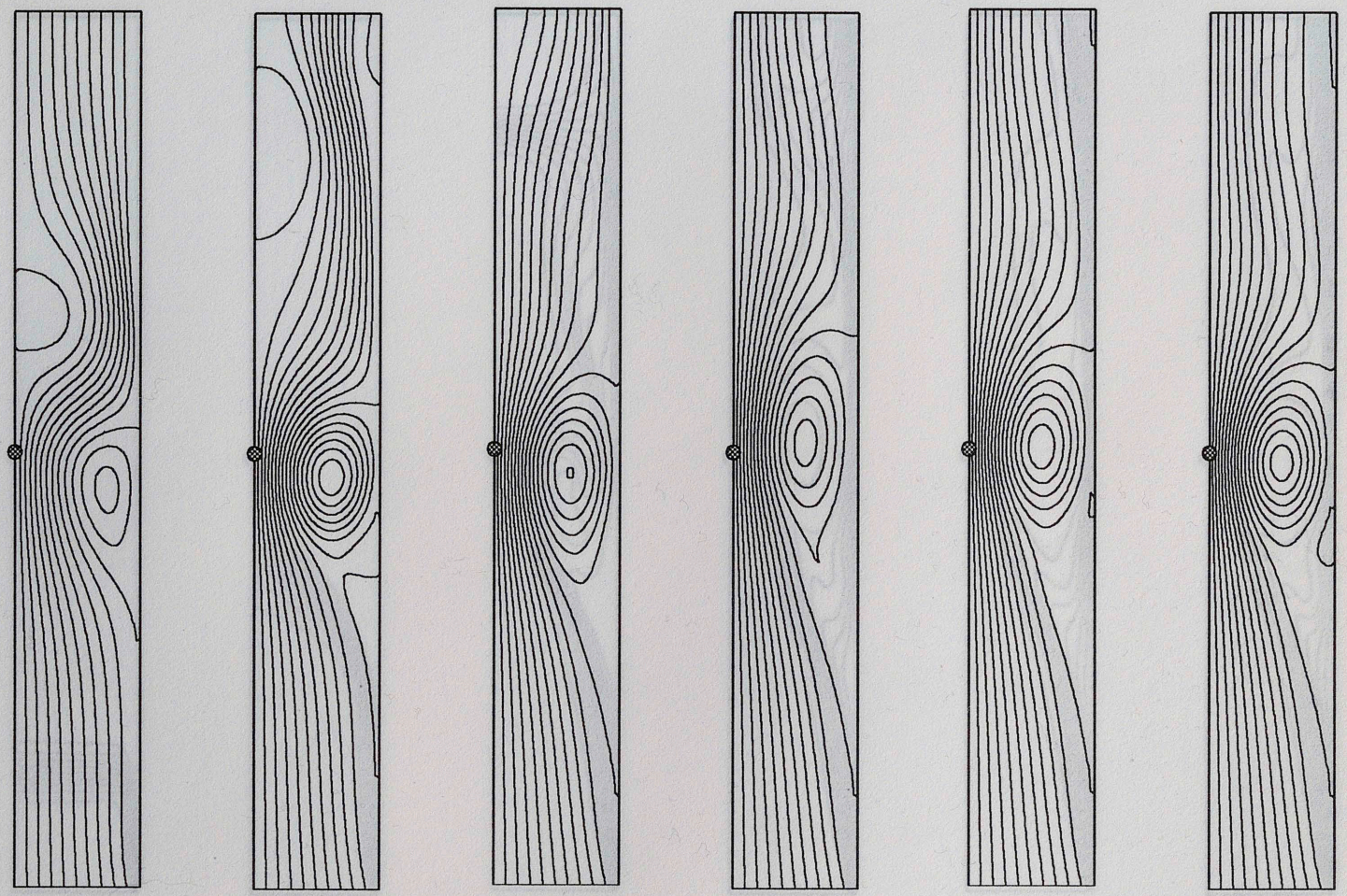

Figure 4.18a Development of Flow Field - Aiding Flow
Re=1200 $Gr=10^5$ $\Delta\psi = 0.009229$

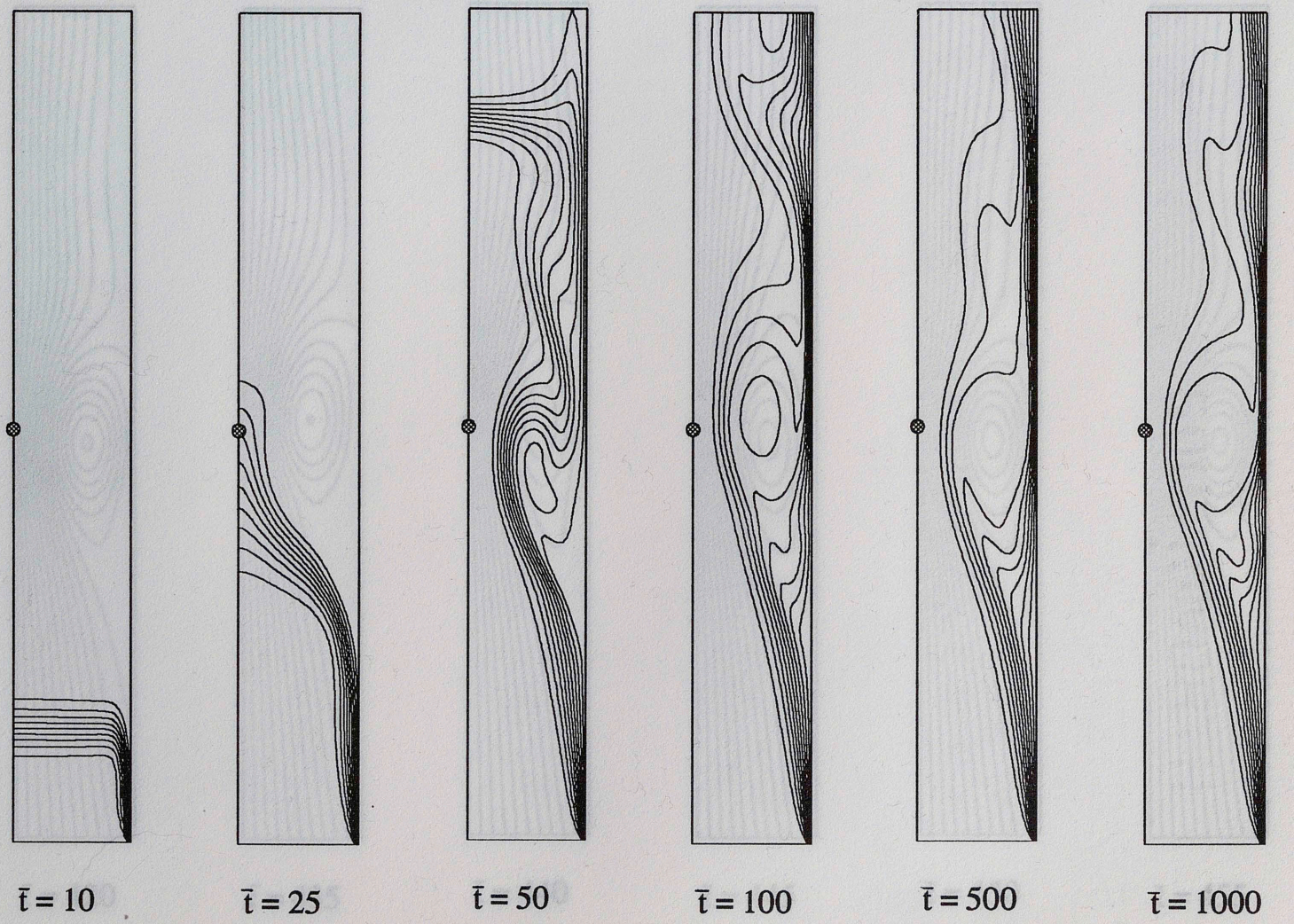

Figure 4.18b Development of Temperature Field - Aiding Flow
Re=1200 Gr=10^5

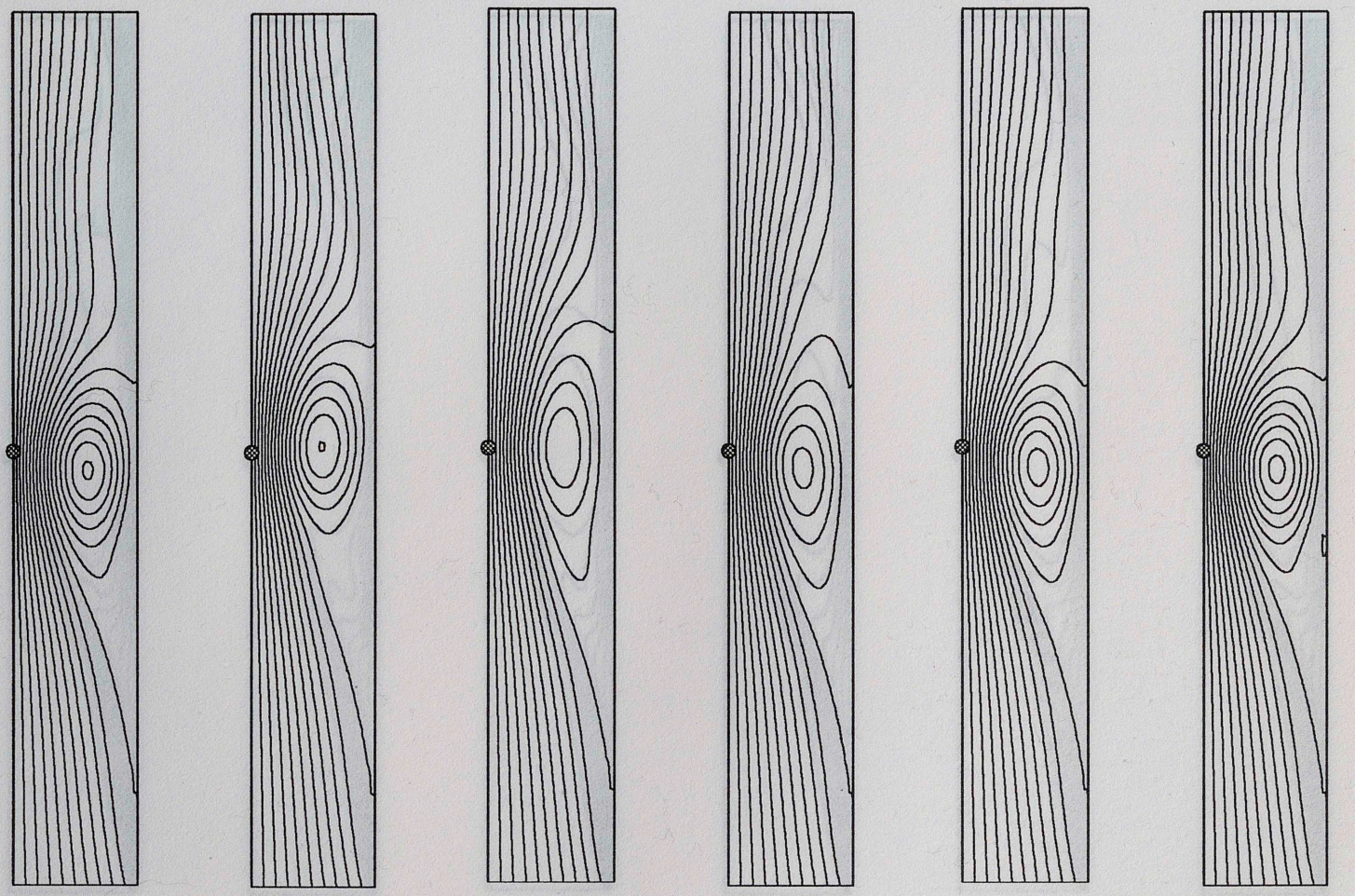

Figure 4.18c Development of Flow Field - Aiding Flow (One Period)
Re=1200 Gr=10^5 $\Delta\psi$ = 0.009229

Figure 4.18d Development of Temperature Field - Aiding Flow (One Period)
Re=1200 $Gr=10^5$

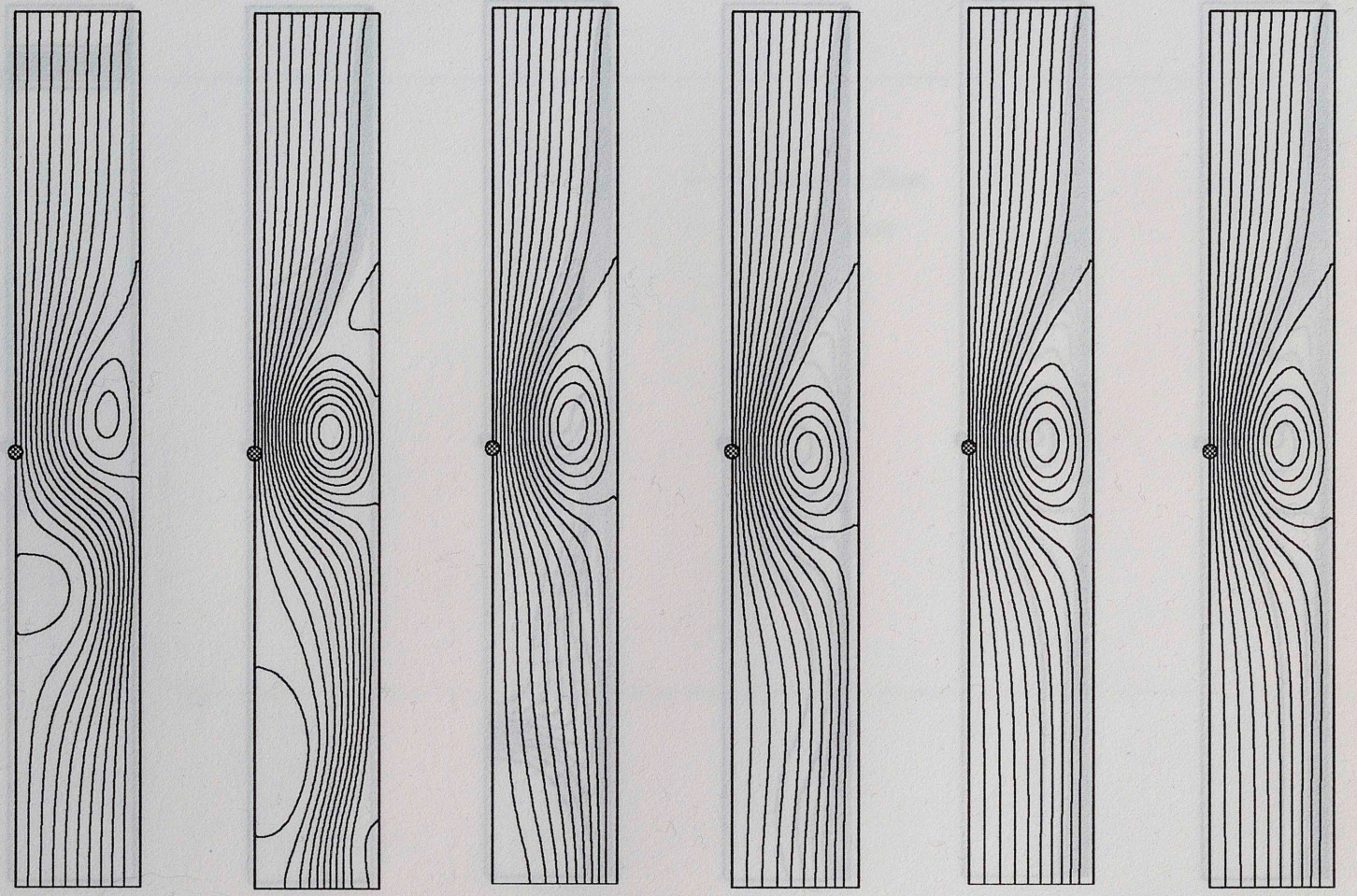

Figure 4.19a Development of Flow Field - Opposing Flow
Re=1200 Gr=10^5 $\Delta\psi$ = 0.009229

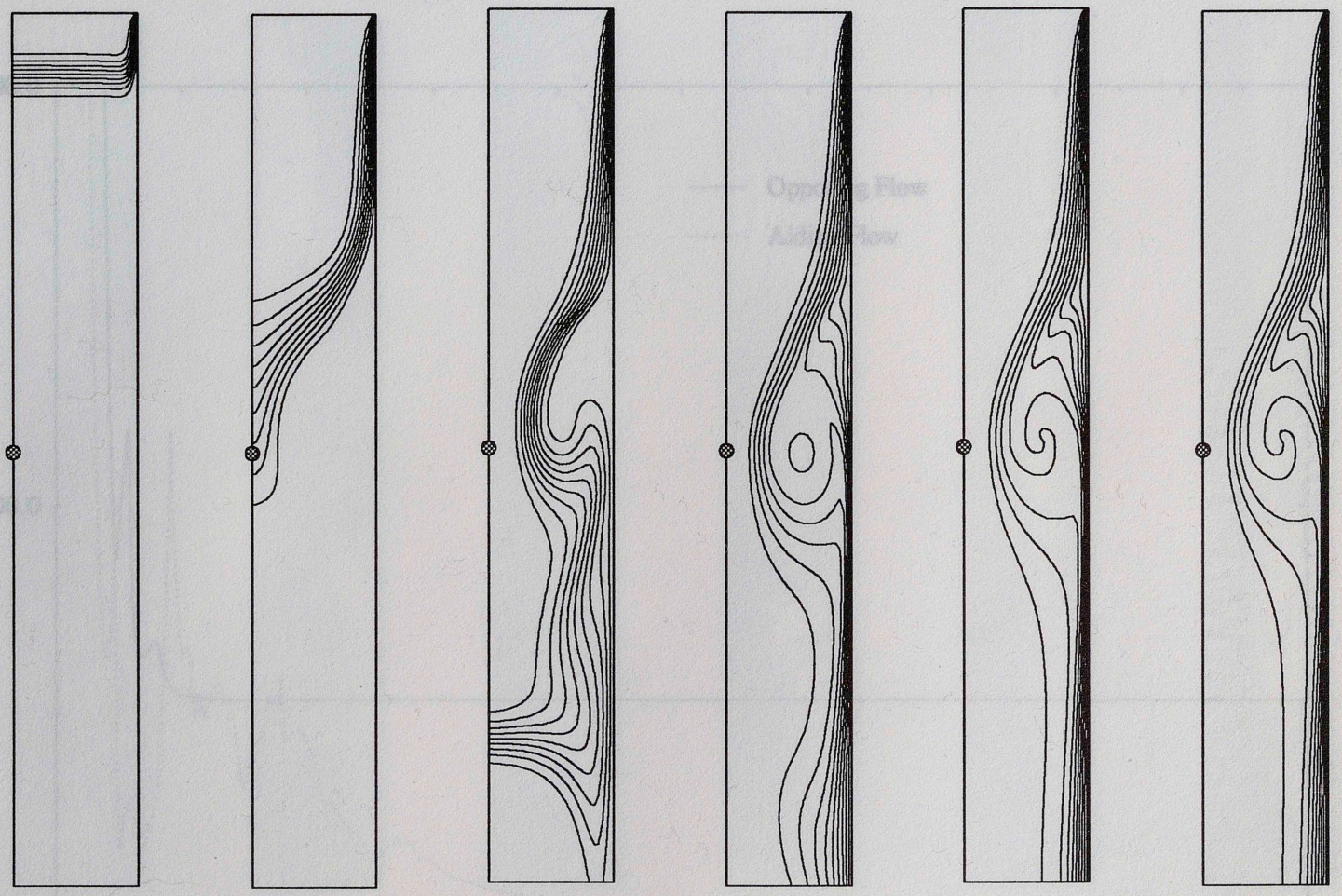

Figure 4.19b Development of Temperature Field - Opposing Flow
Re=1200 $Gr=10^5$

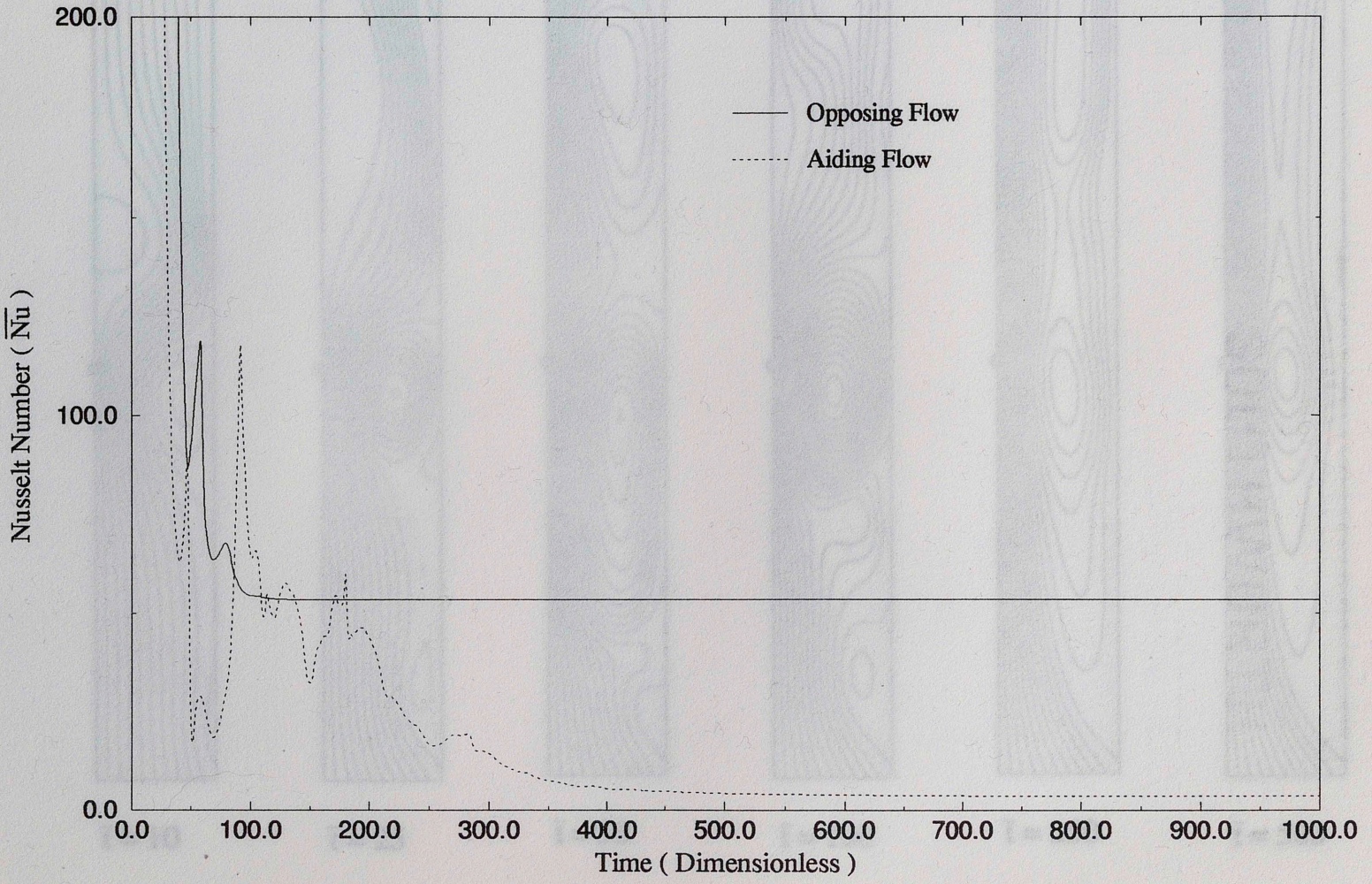

Figure 4.20 Variation of Average Nusselt Number with Time (Re=1200, $Gr=10^6$)

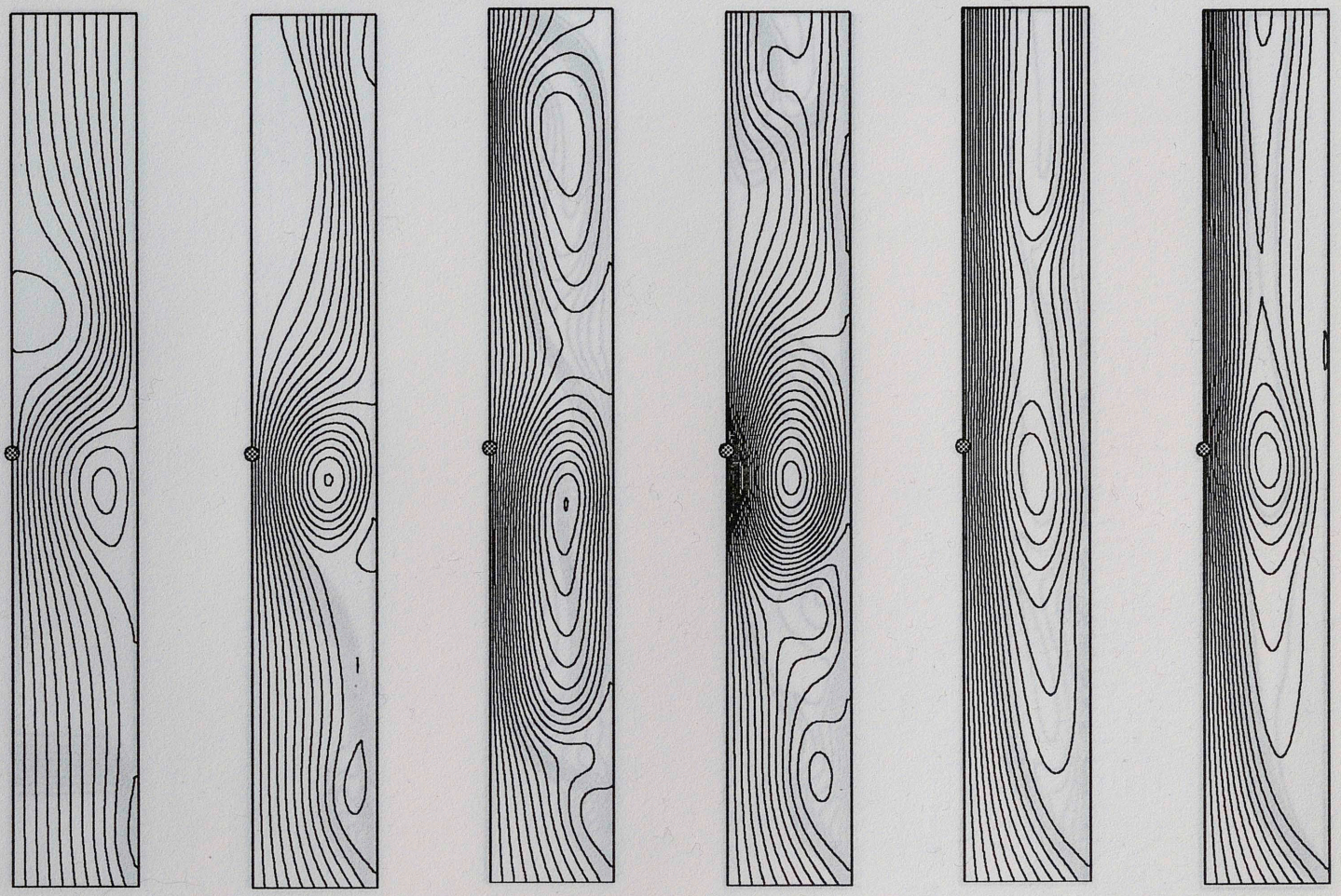

Figure 4.21a Development of Flow Field - Aiding Flow
Re=1200 Gr=10^6 $\Delta\psi$ = 0.009229

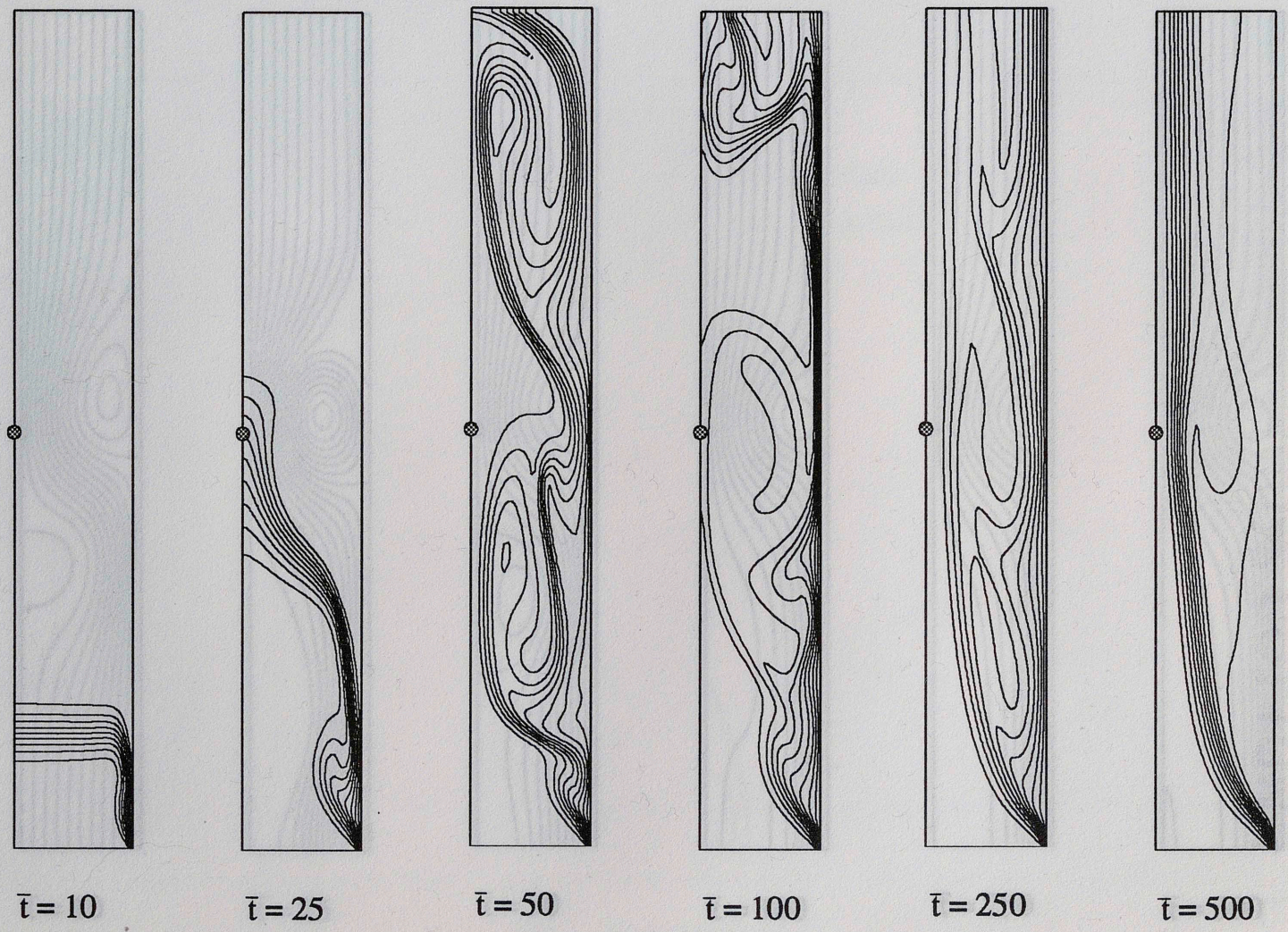

Figure 4.21b Development of Temperature Field - Aiding Flow
Re=1200 Gr=10^6

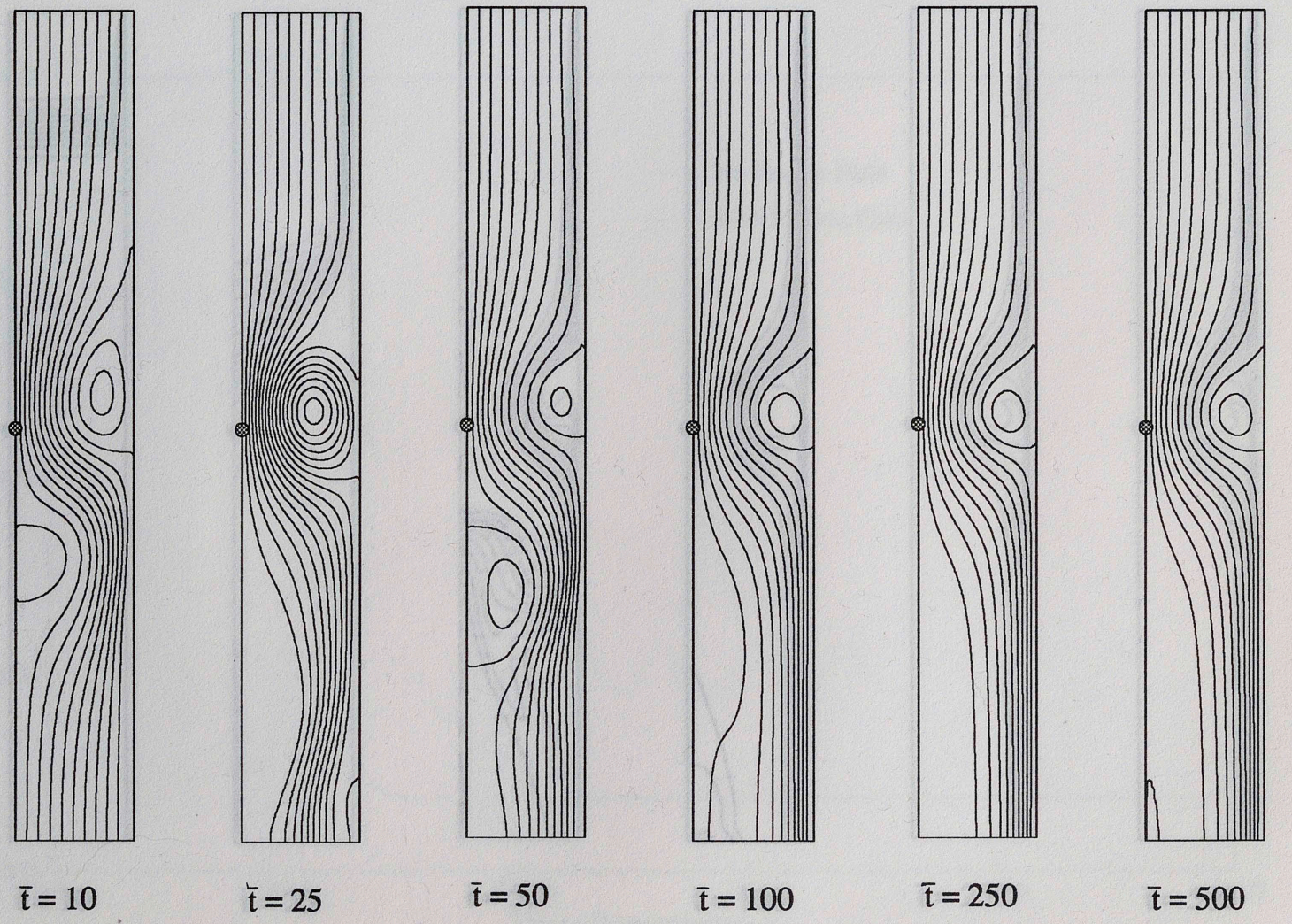

Figure 4.22a Development of Flow Field - Opposing Flow
Re=1200 Gr=10^6 $\Delta\psi = 0.009229$

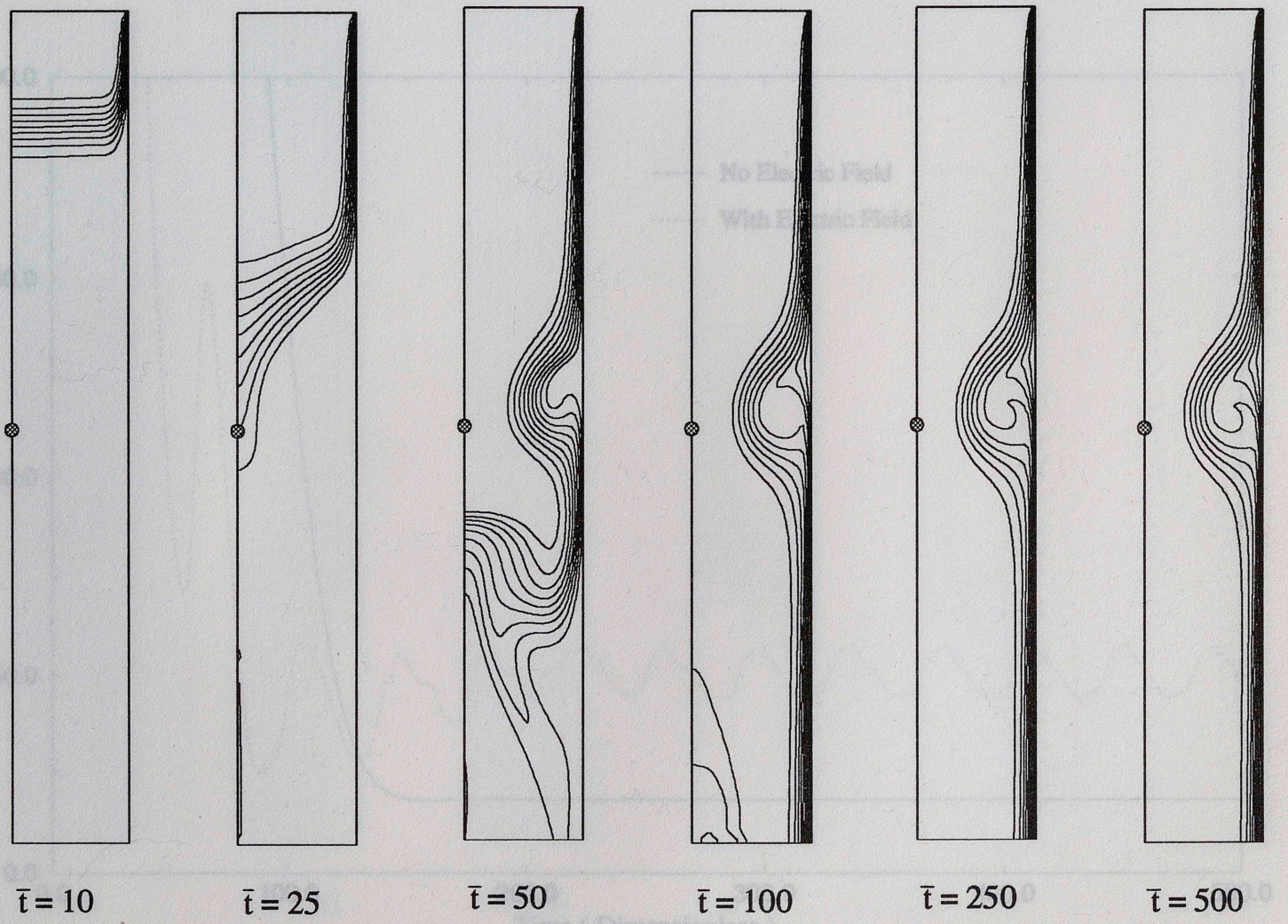

Figure 4.22b Development of Temperature Field - Opposing Flow
Re=1200 $Gr=10^6$

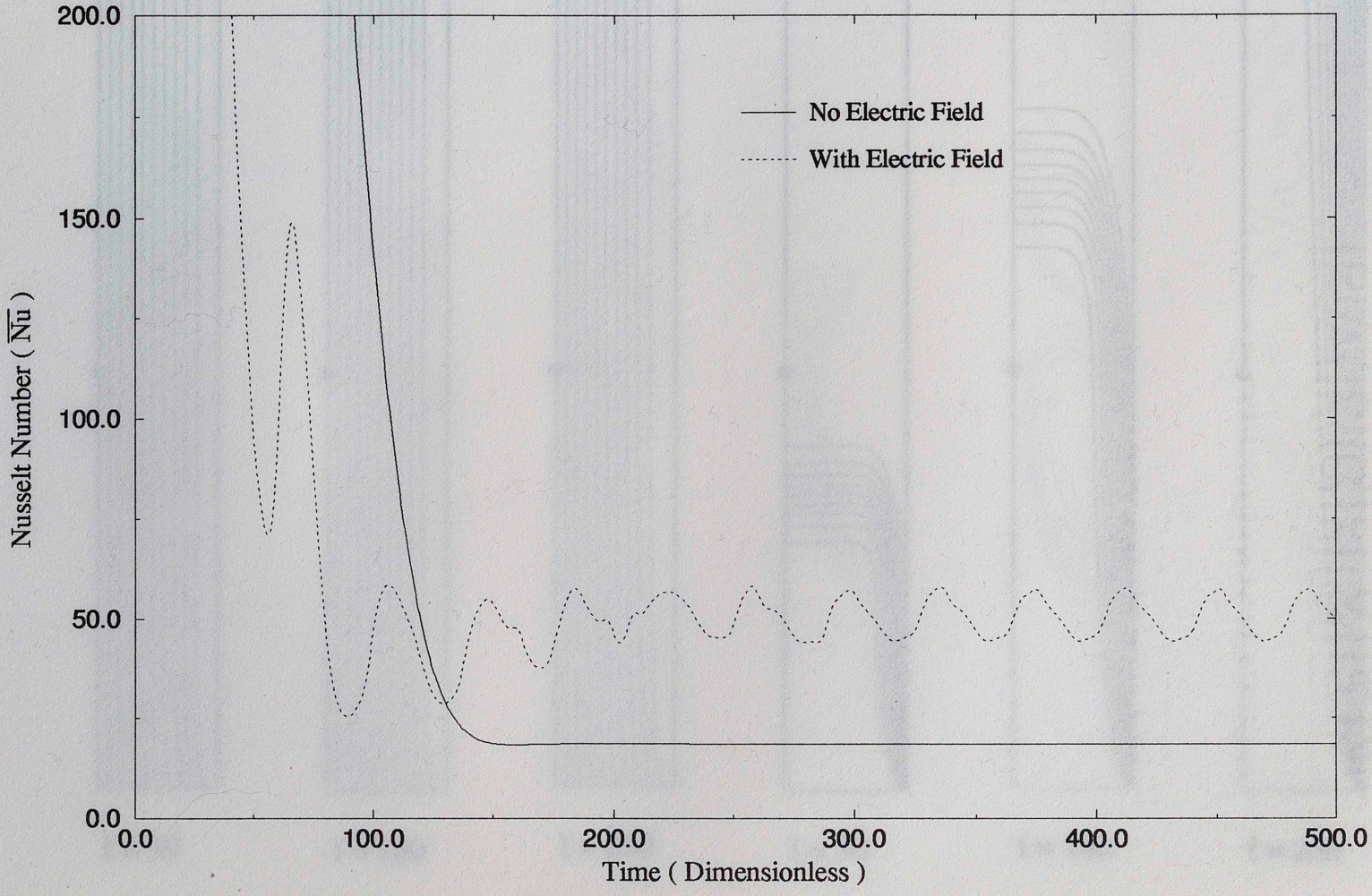

Figure 4.23 Variation of Average Nusselt Number with Time for Forced Convection (Re=600)

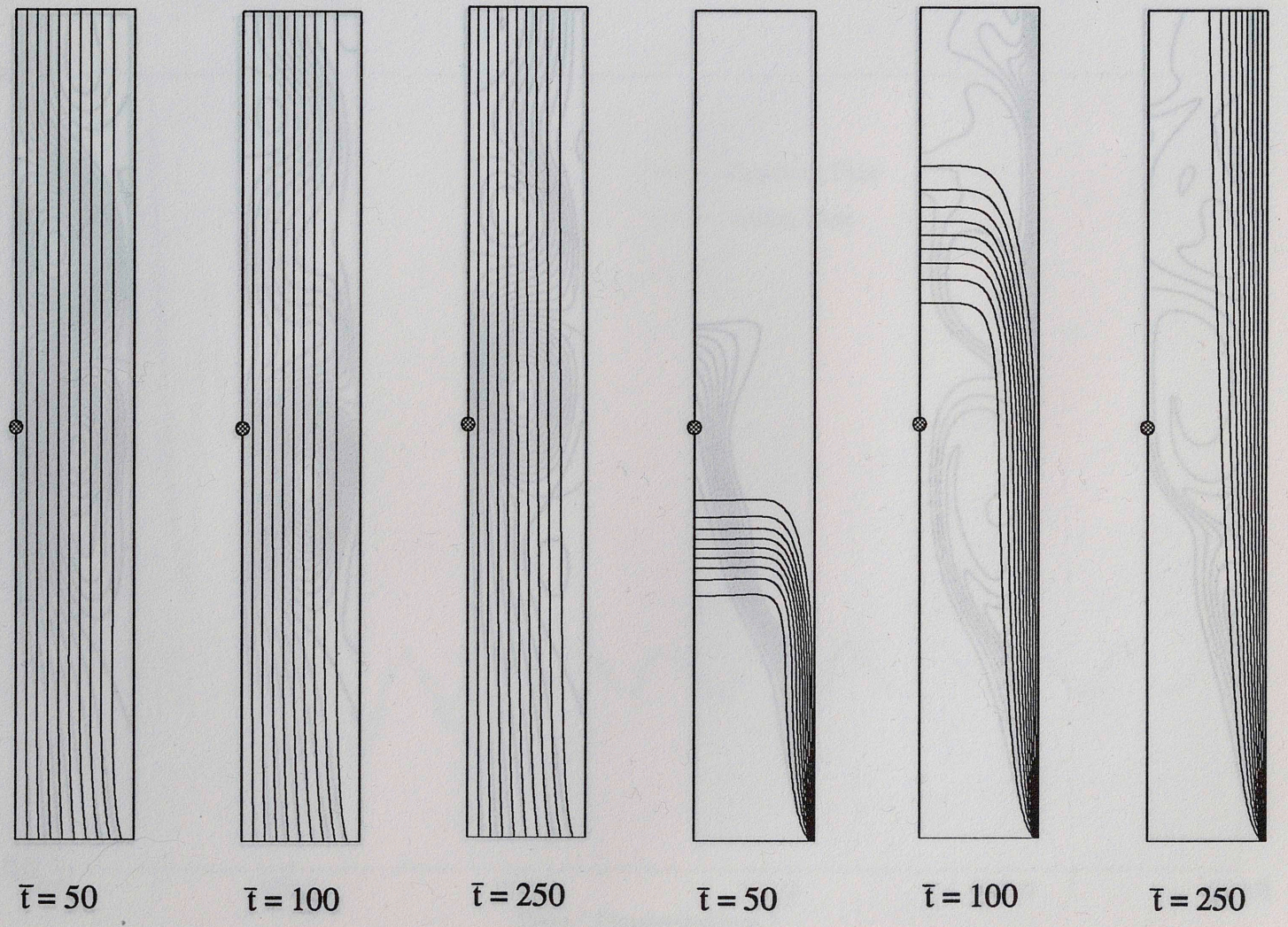

Figure 4.24a Development of Flow and Temperature Field for Forced Convection
(Without Electric Field Re = 600)

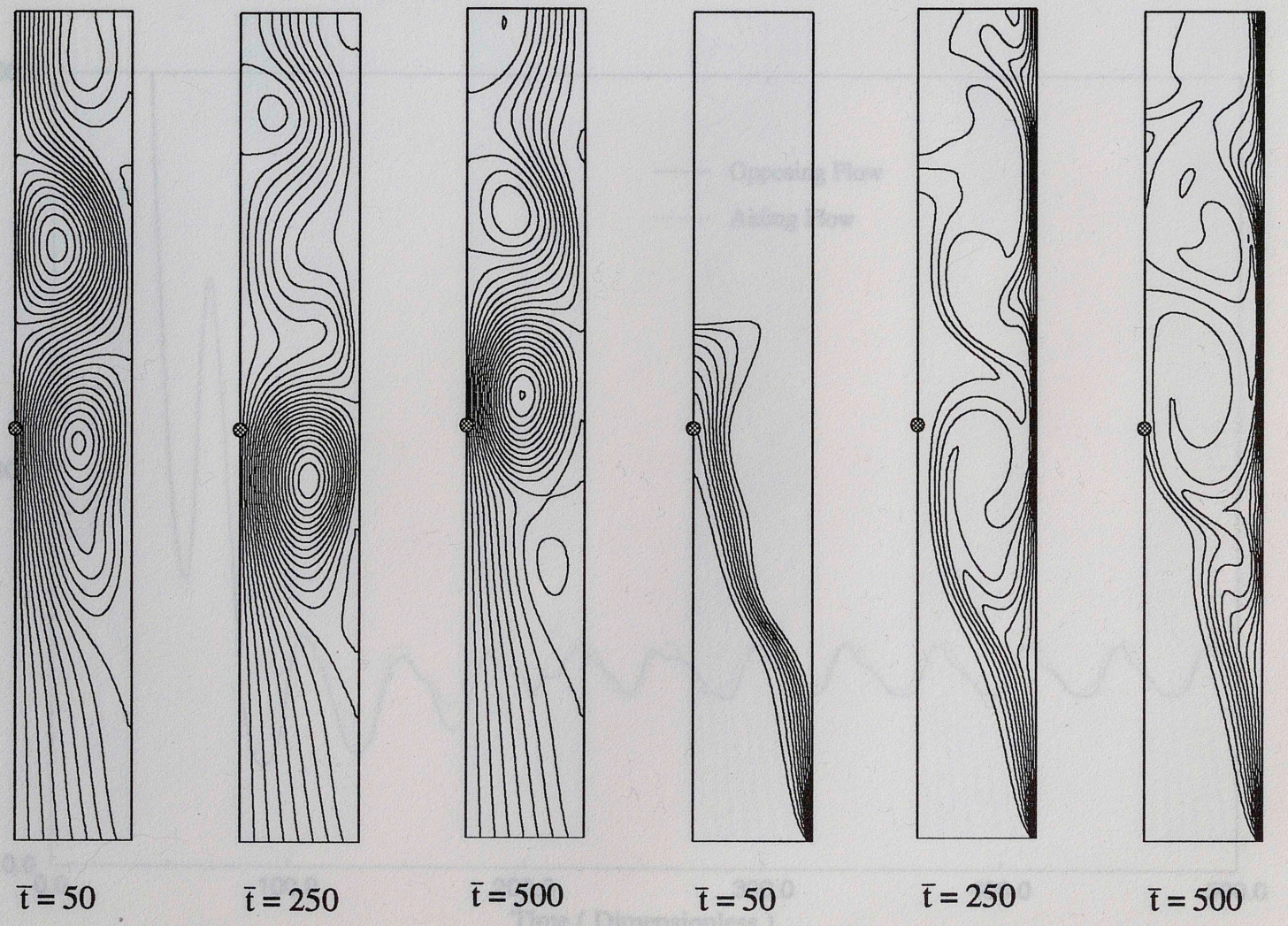

Figure 4.24b Development of Flow and Temperature Field for Forced Convection
(With Electric Field Re = 1200)

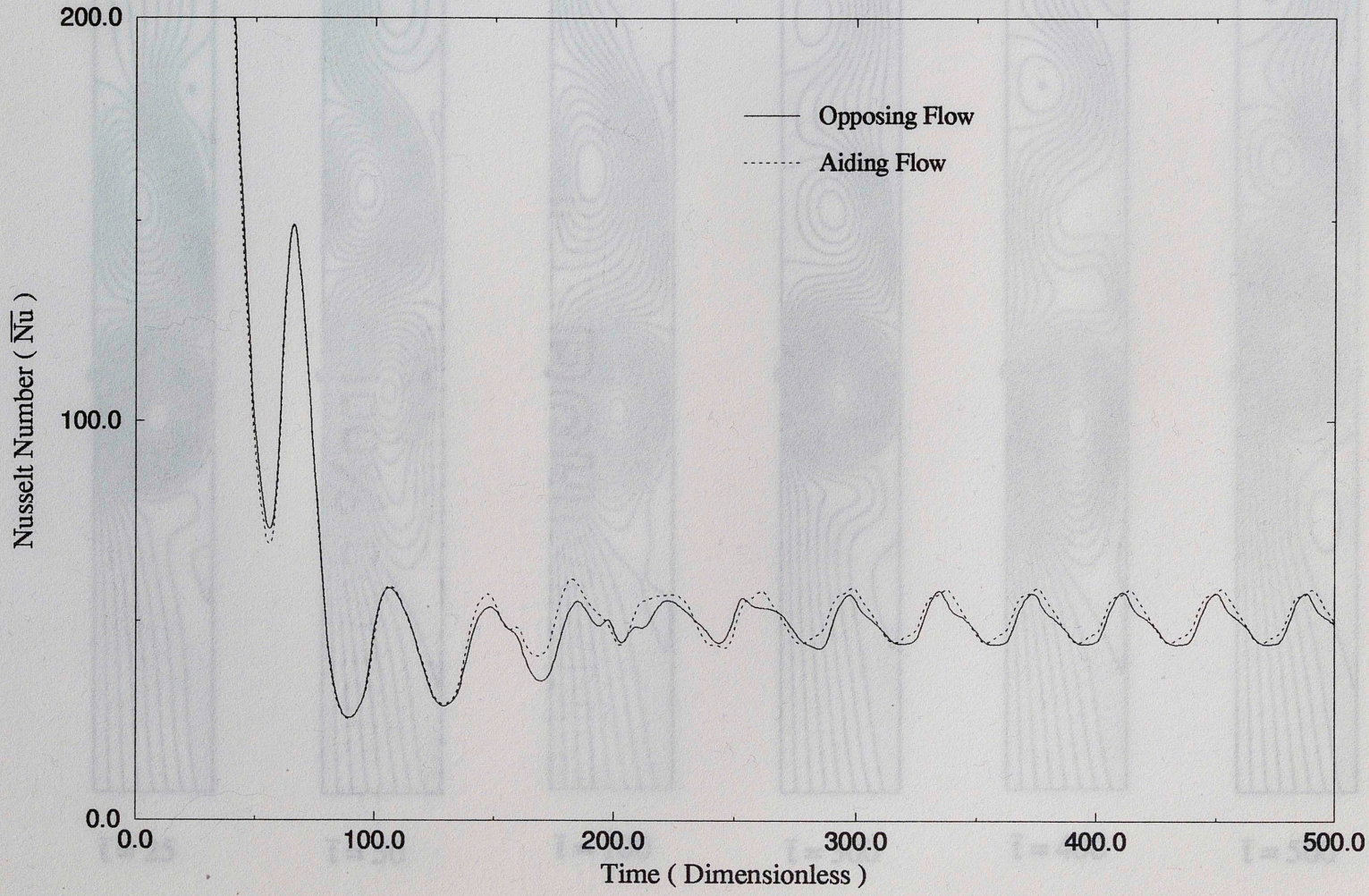

Figure 4.25 Variation of Average Nusselt Number with Time (Re=600, Gr=10^4)

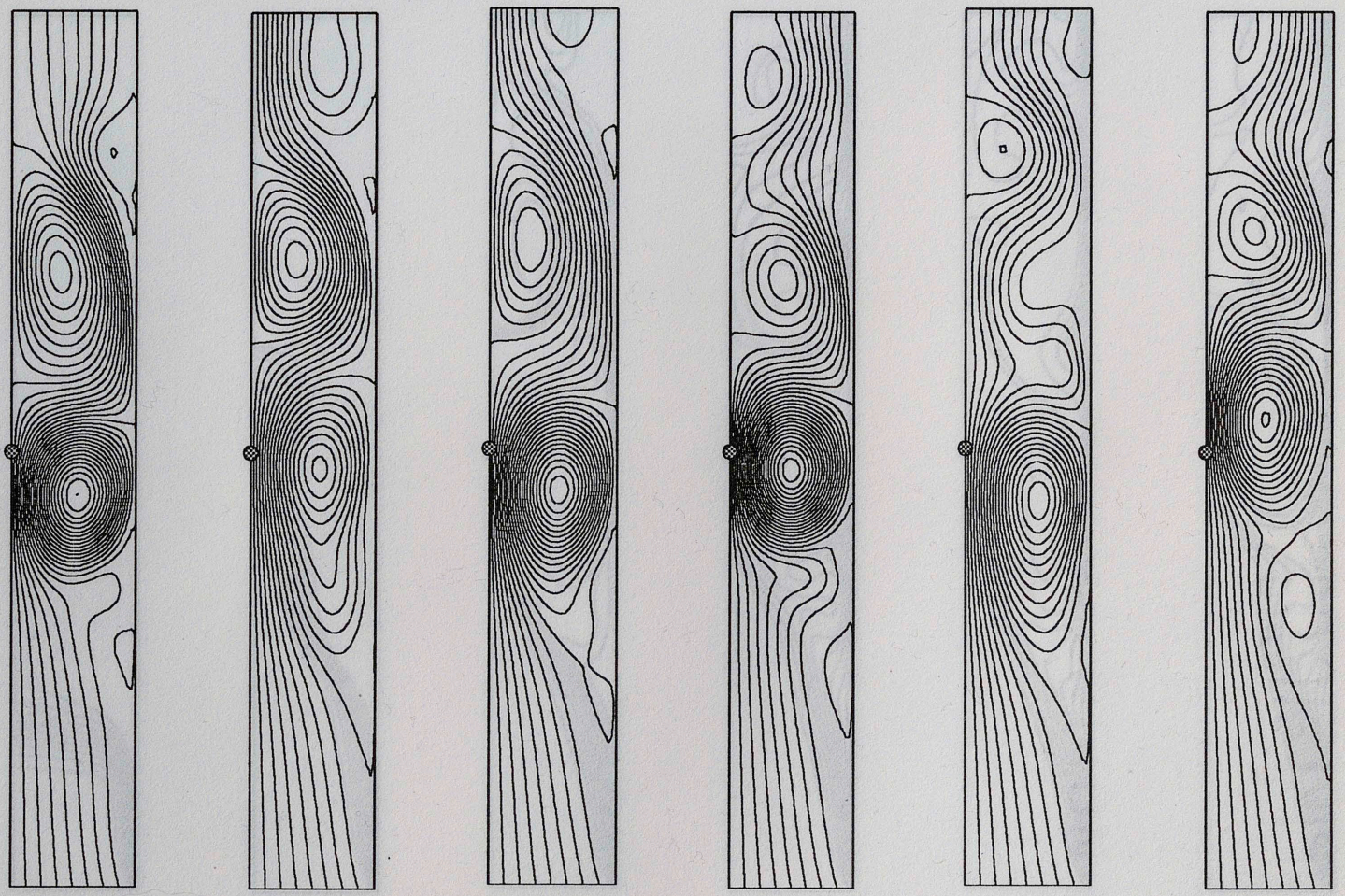

Figure 4.26a Development of Flow Field - Aiding Flow
Re=600 $Gr=10^4$ $\Delta\psi = 0.00577$

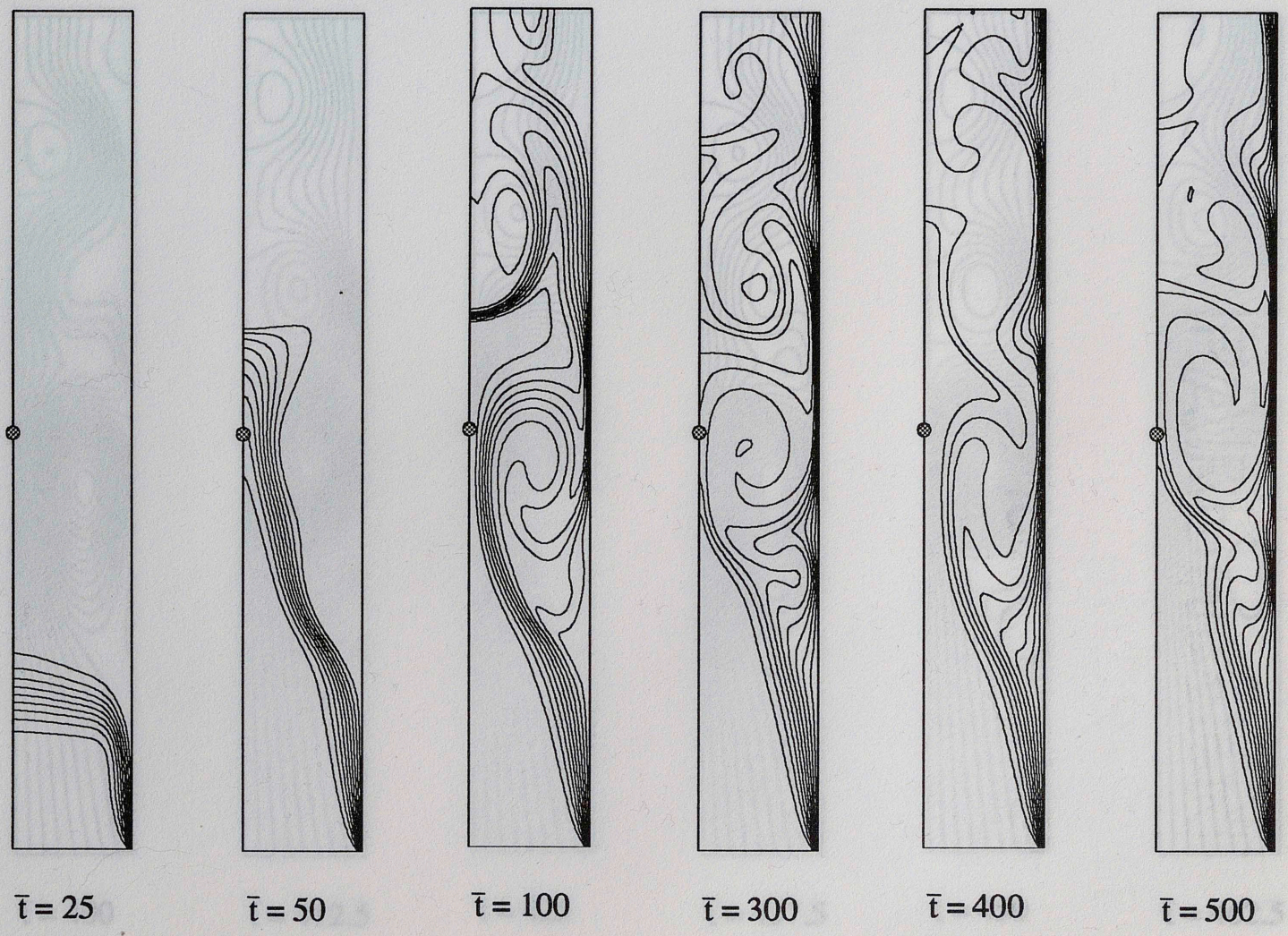

Figure 4.26b Development of Temperature Field - Aiding Flow
Re=600 Gr=10^4

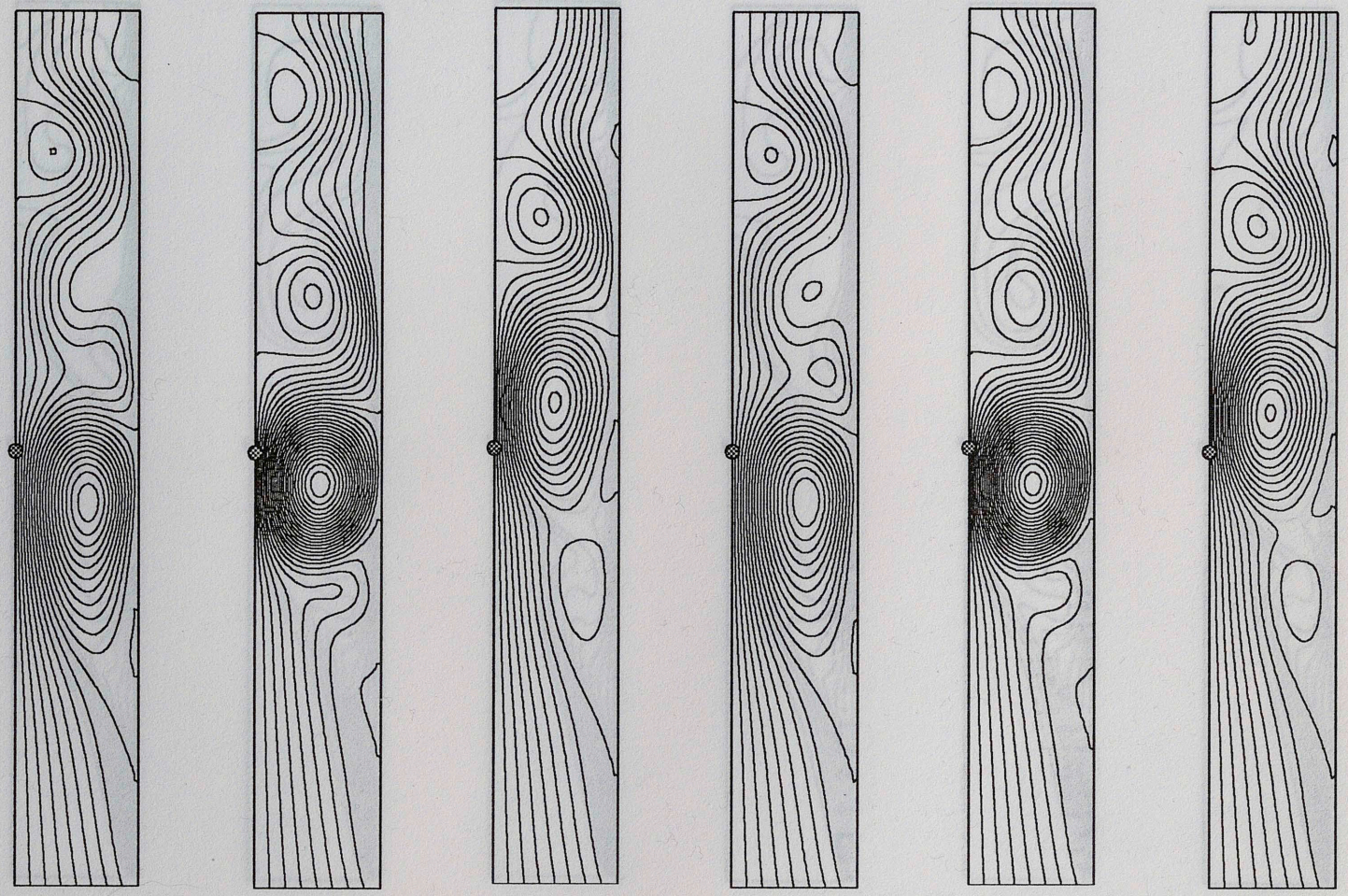

Figure 4.26c Development of Flow Field - Aiding Flow (One and Half Period)
Re=600 Gr=10^4 $\Delta\psi$ = 0.00577

Figure 4.26d Development of Temperature Field - Aiding Flow (One and Half Period)
Re=600 Gr=10^4

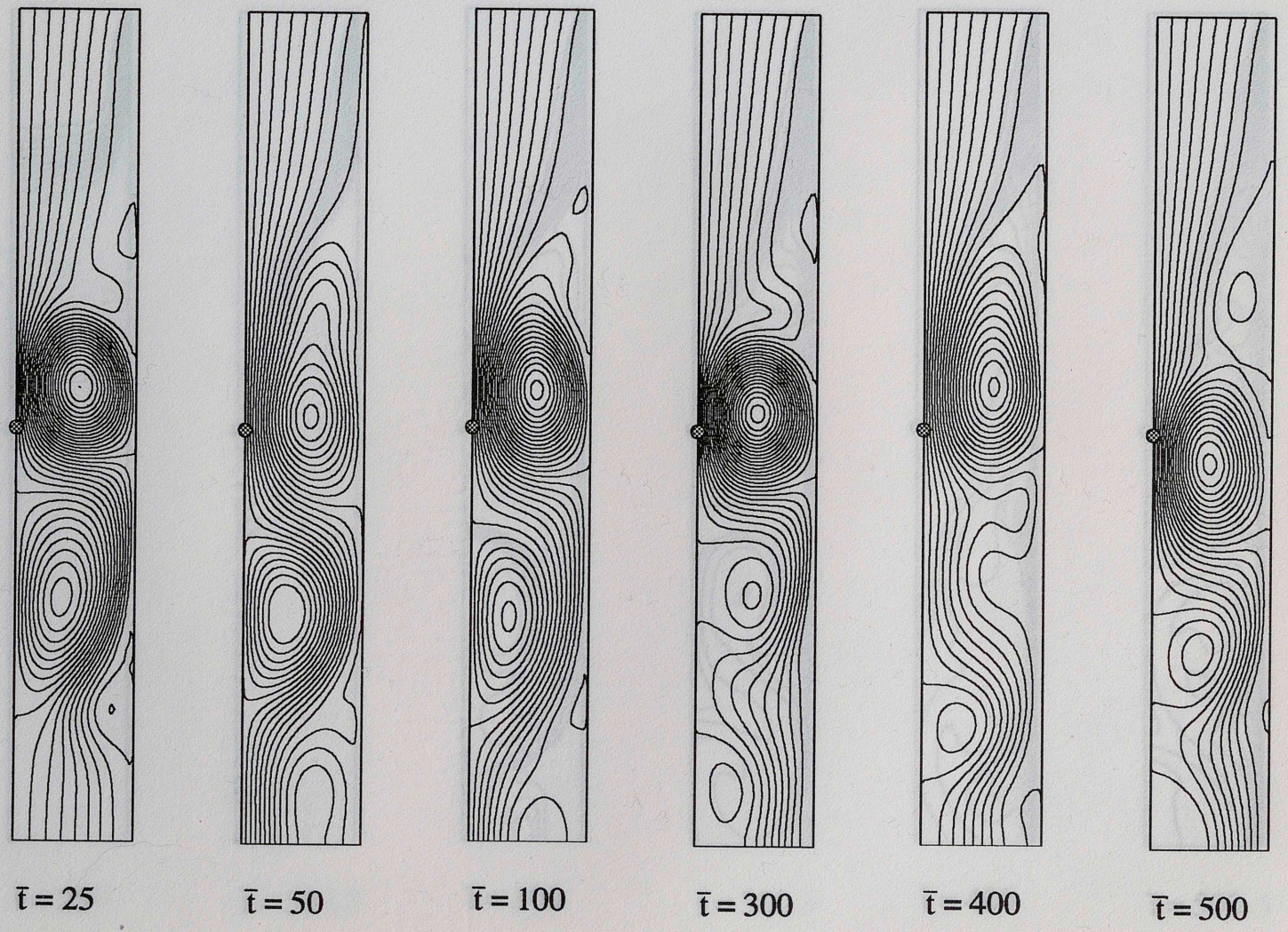

Figure 4.27a Development of Flow Field - Opposing Flow
Re=600 $Gr=10^4$ $\Delta\psi = 0.00577$

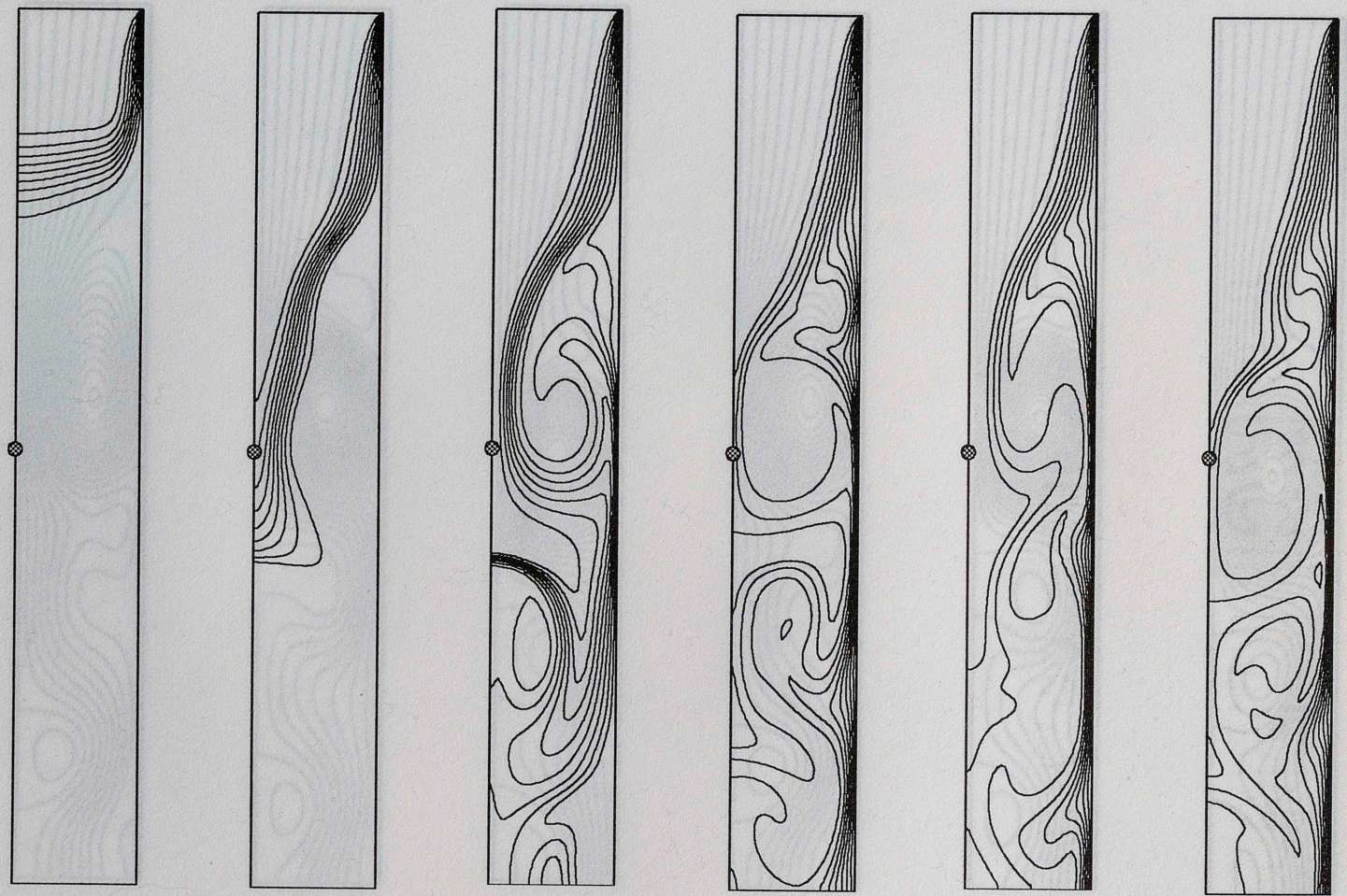

Figure 4.27b Development of Temperature Field - Opposing Flow
Re=600 Gr=10^4

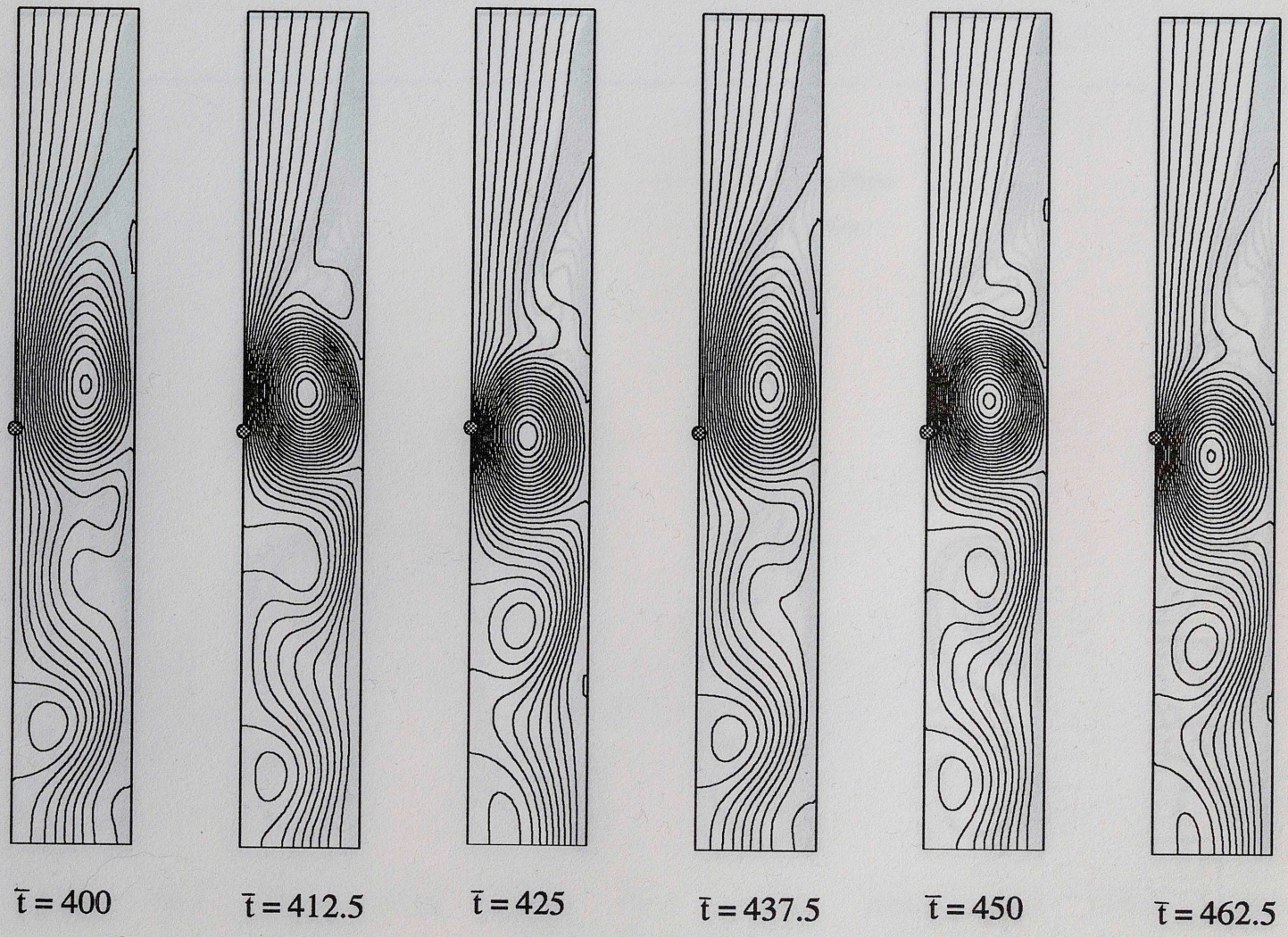

Figure 4.27c Development of Flow Field - Opposing Flow (One and Half Period)
Re=600 $Gr=10^4$ $\Delta\psi = 0.00577$

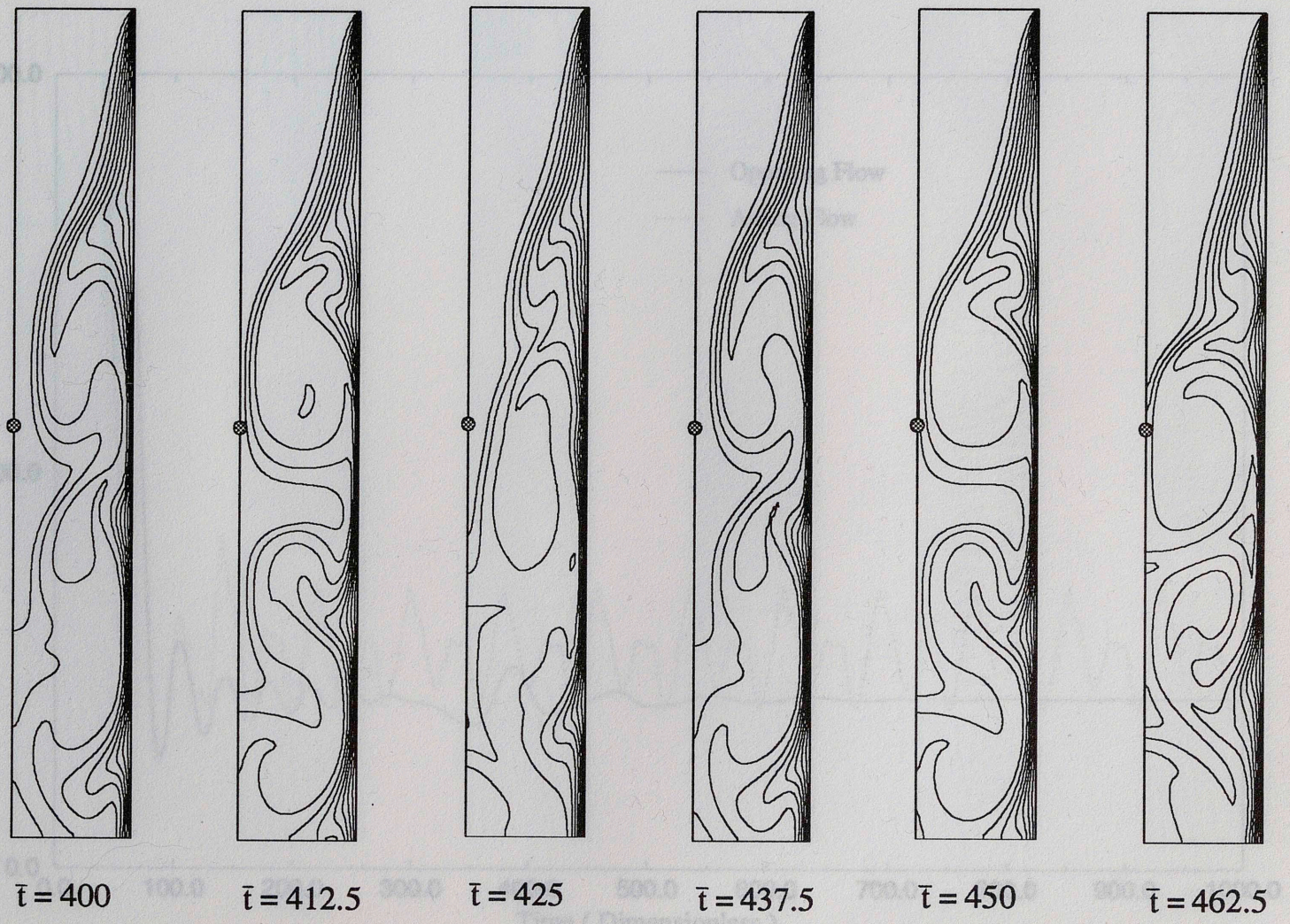

Figure 4.27d Development of Temperature Field - Opposing Flow (One and Half Period)
Re=600 Gr=10^4

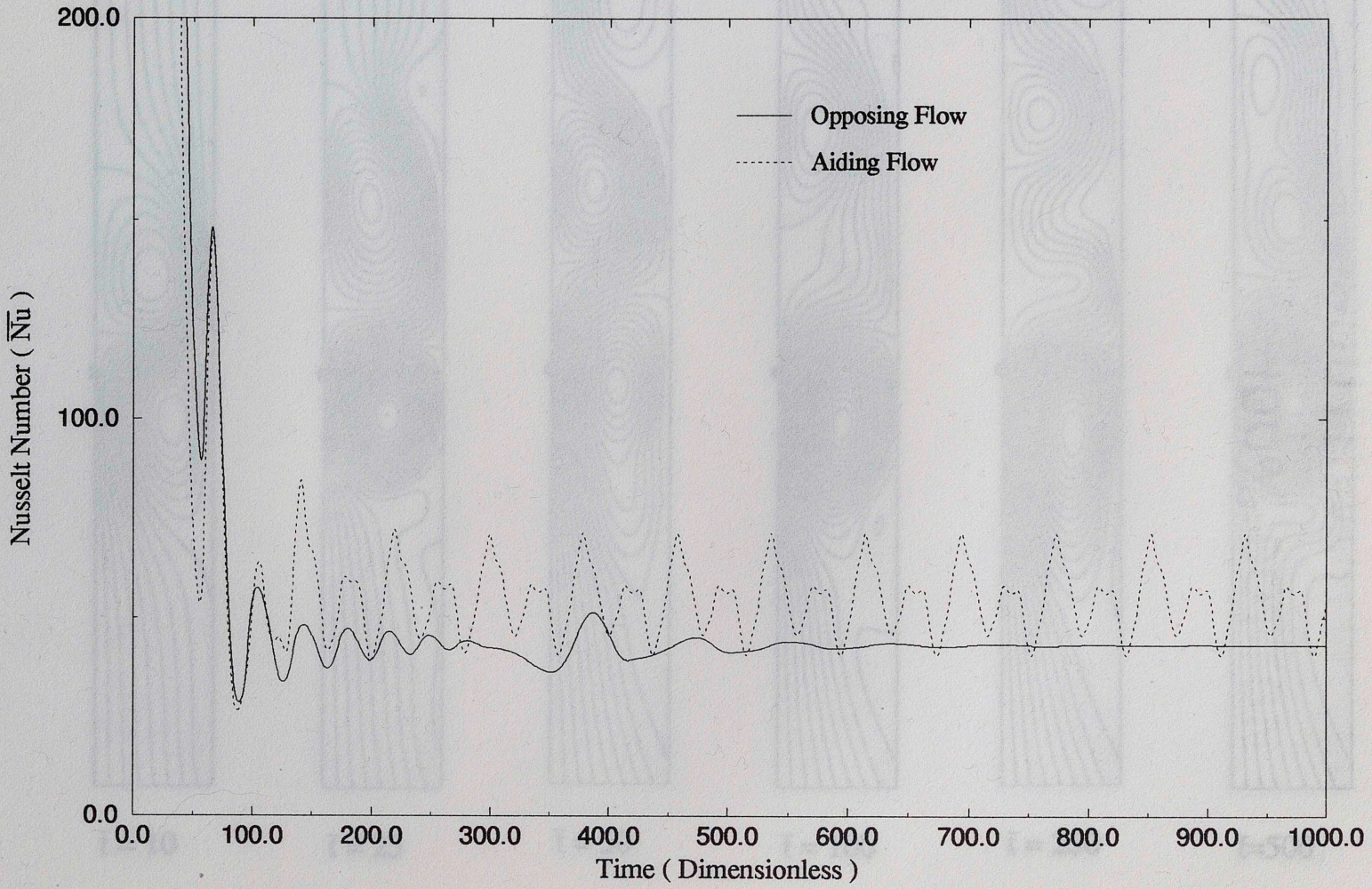

Figure 4.28 Variation of Average Nusselt Number with Time (Re=600, Gr=10^5)

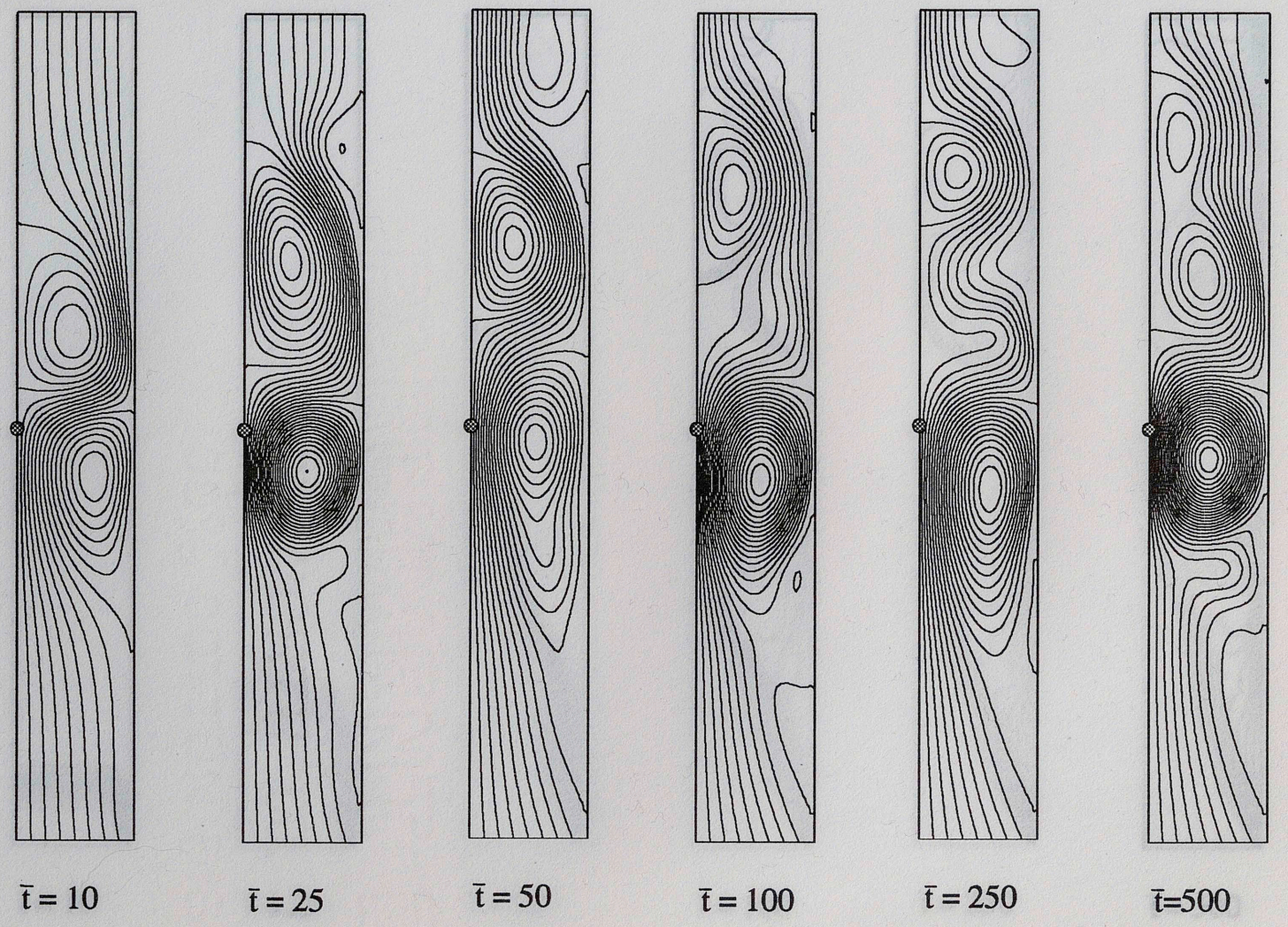

Figure 4.29a Development of Flow Field - Aiding Flow
Re=600 Gr=10^5 $\Delta\psi$ = 0.00577

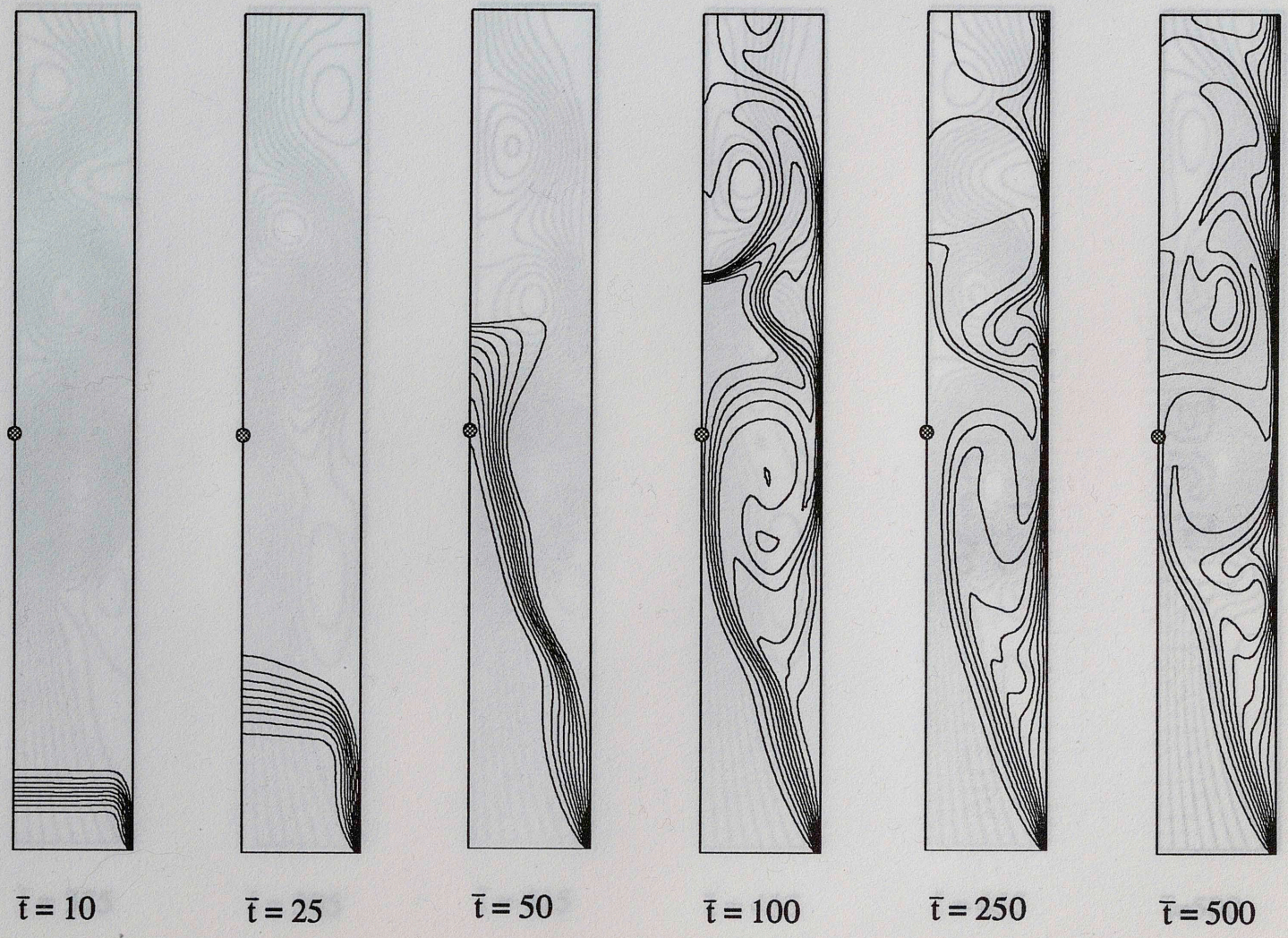

Figure 4.29b Development of Temperature Field - Aiding Flow
Re=600 Gr=10^5

Figure 4.29c Development of Flow Field - Aiding Flow (One Period)

Re=600 Gr=10^5 $\Delta\psi$ = 0.00577

Figure 4.29d Development of Temperature Field - Aiding Flow (One Period)
Re=600 Gr=10^5

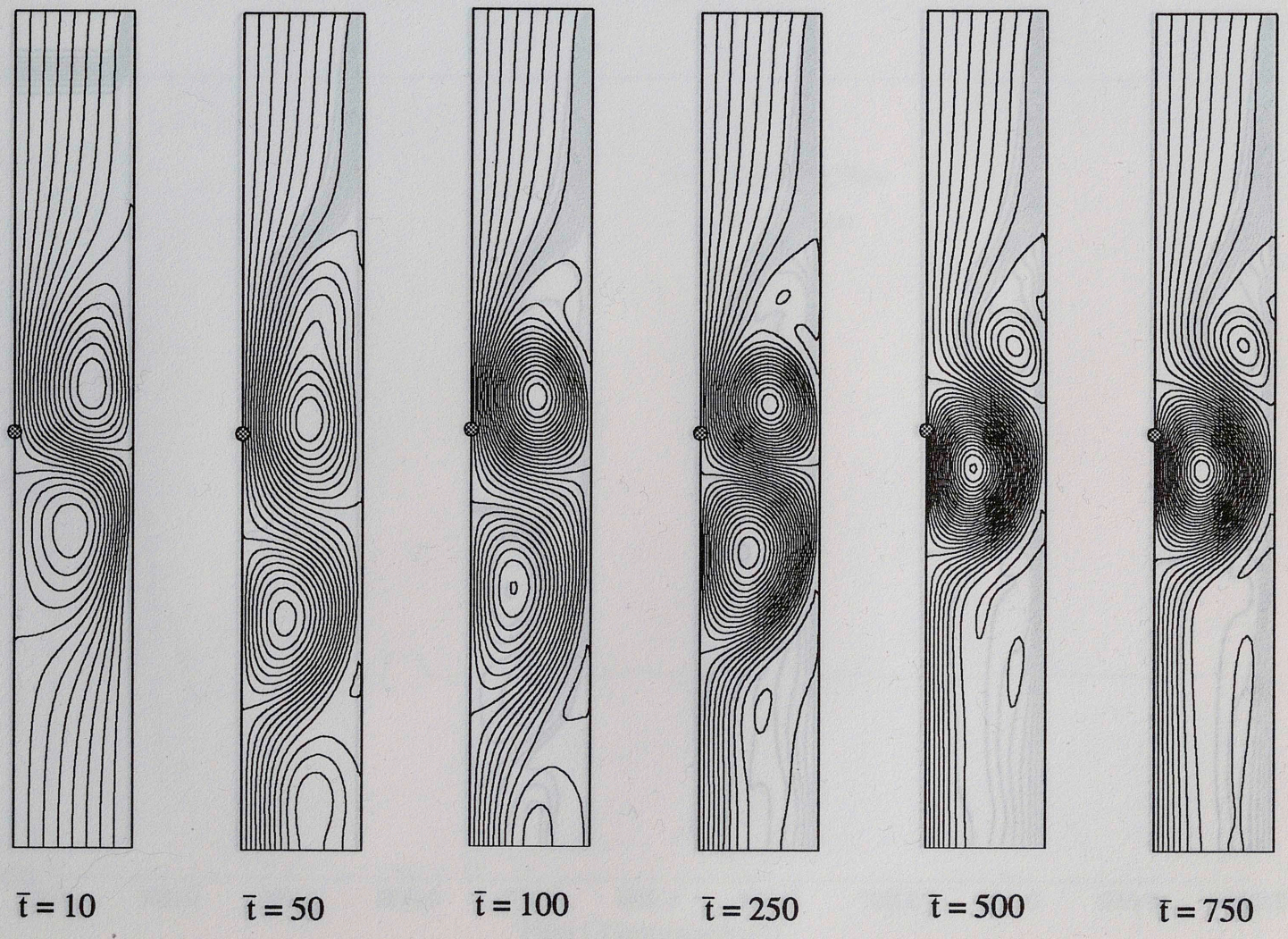

Figure 4.30a Development of Flow Field - Opposing Flow
Re=600 $Gr=10^5$ $\Delta\psi = 0.00577$

UNIVERSITY OF OKLAHOMA
LIBRARIES

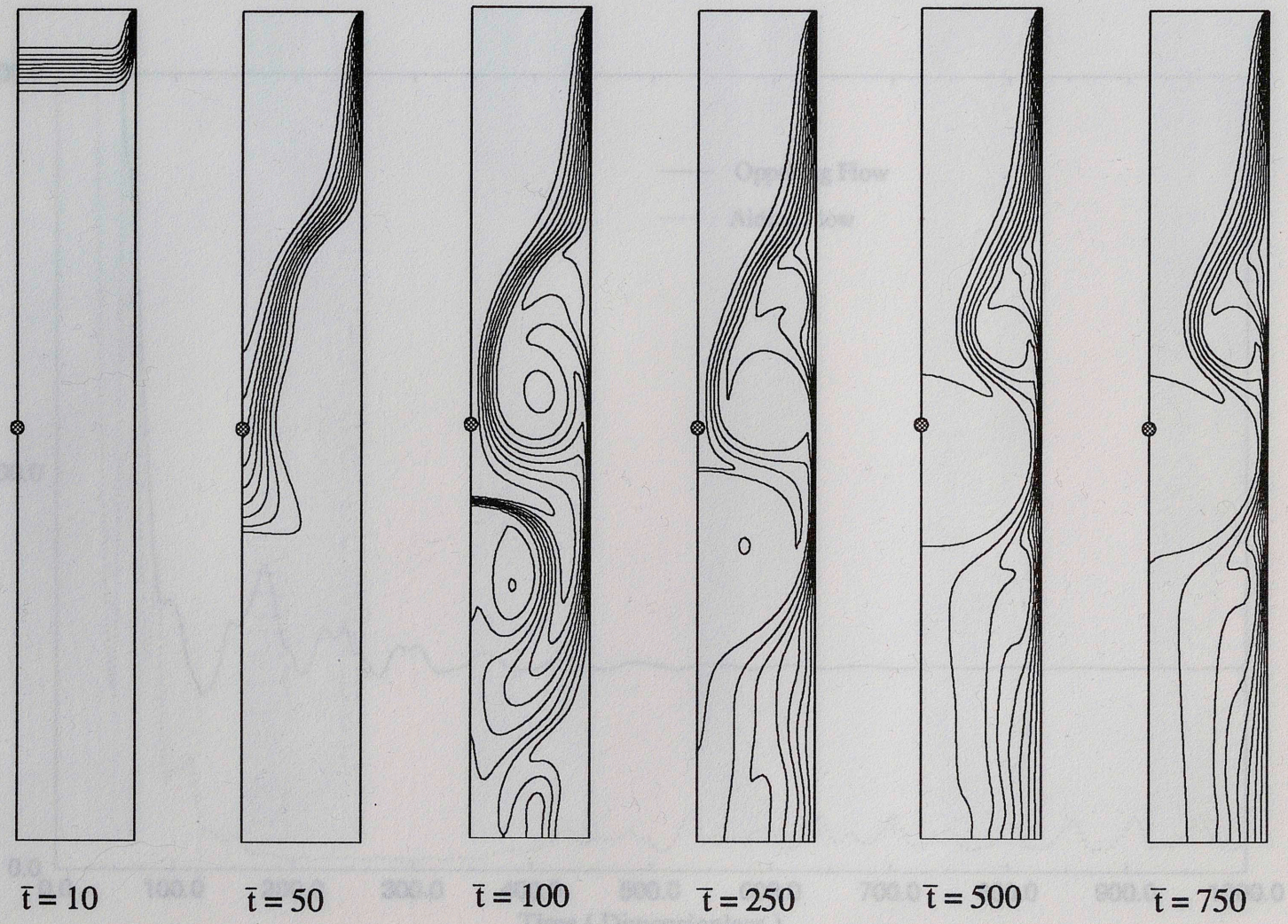

Figure 4.30b Development of Temperature Field - Opposing Flow
Re=600 $Gr=10^5$

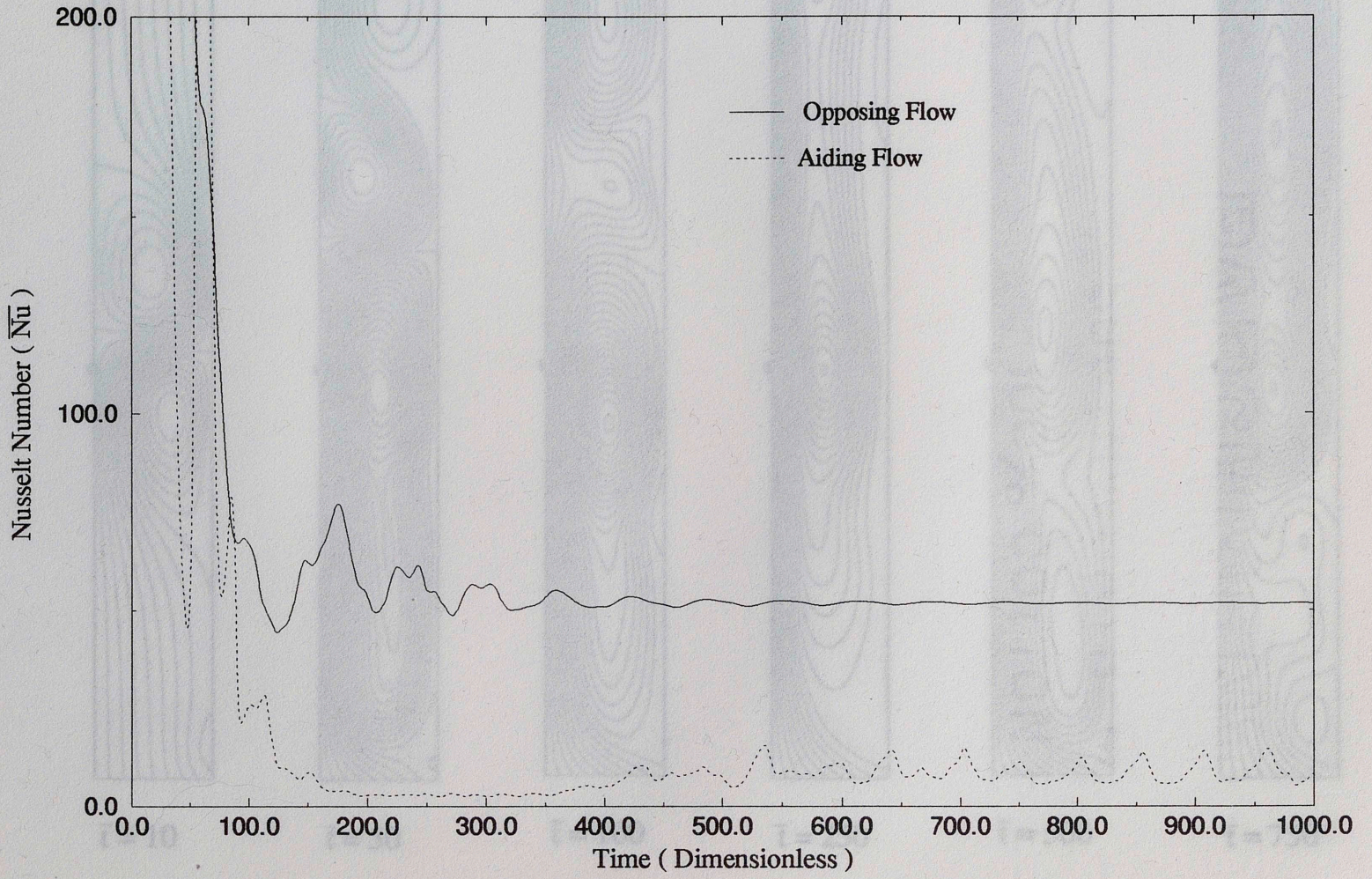

Figure : 4.31 Variation of Average Nusselts Number with Time (Re=600 Gr=10^6)

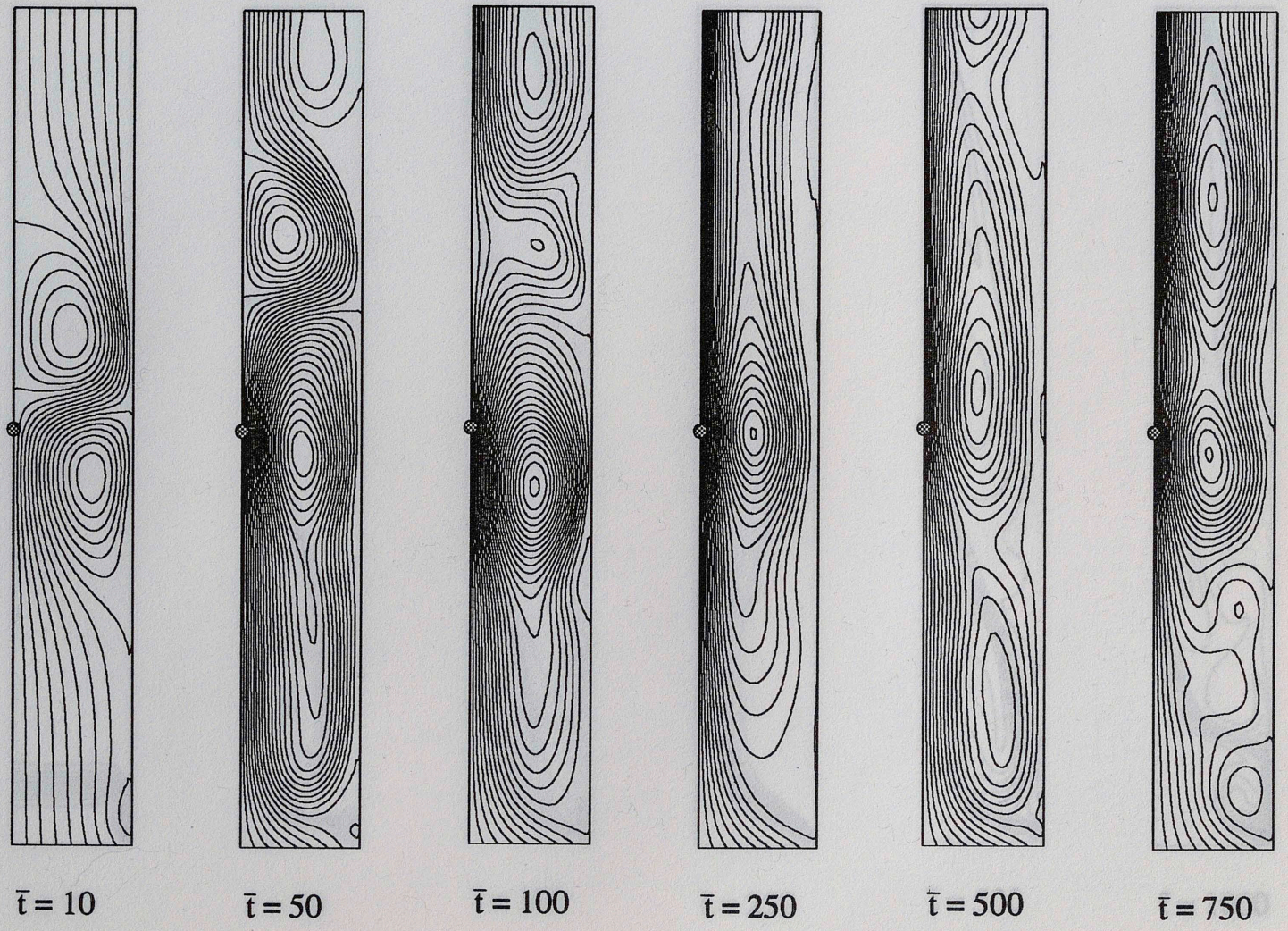

Figure 4.32a Development of Flow Field - Aiding Flow
Re=600 Gr=10^6 $\Delta\psi$ = 0.00577

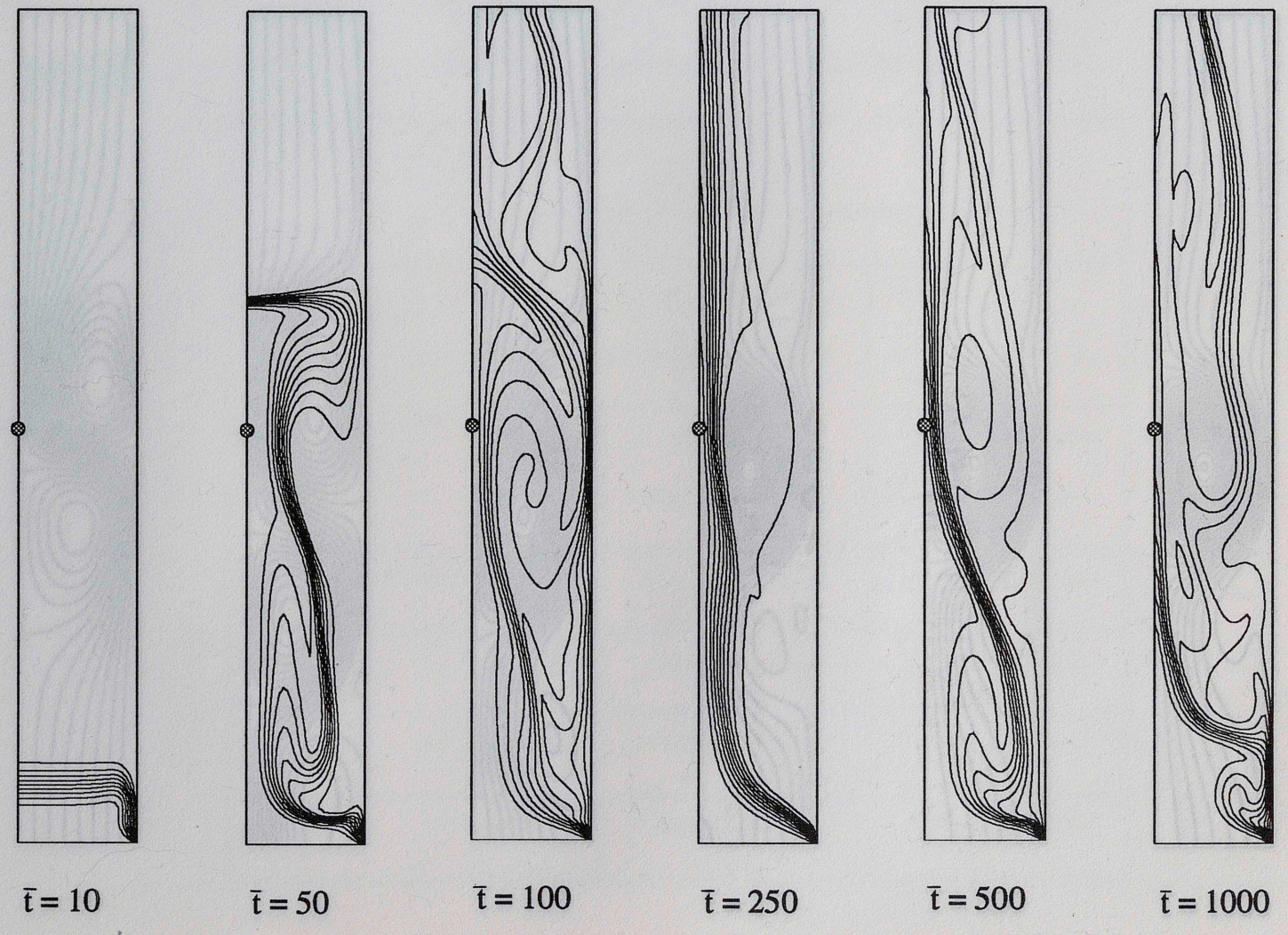

Figure 4.32b Development of Temperature Field - Aiding Flow
Re=600 Gr=10^6

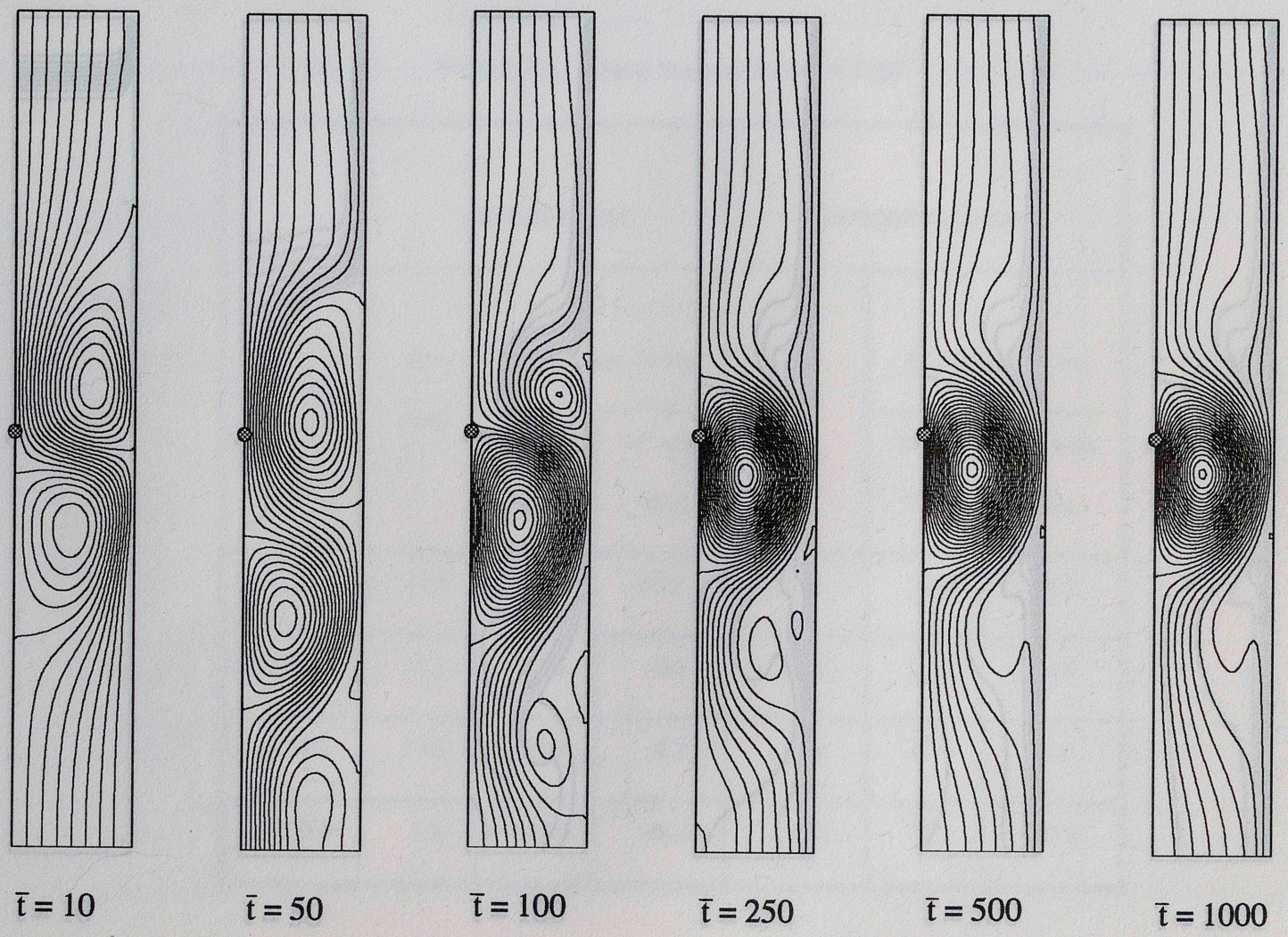

Figure 4.33a Development of Flow Field - Opposing Flow

Re=600 $Gr=10^6$ $\Delta\psi = 0.00577$

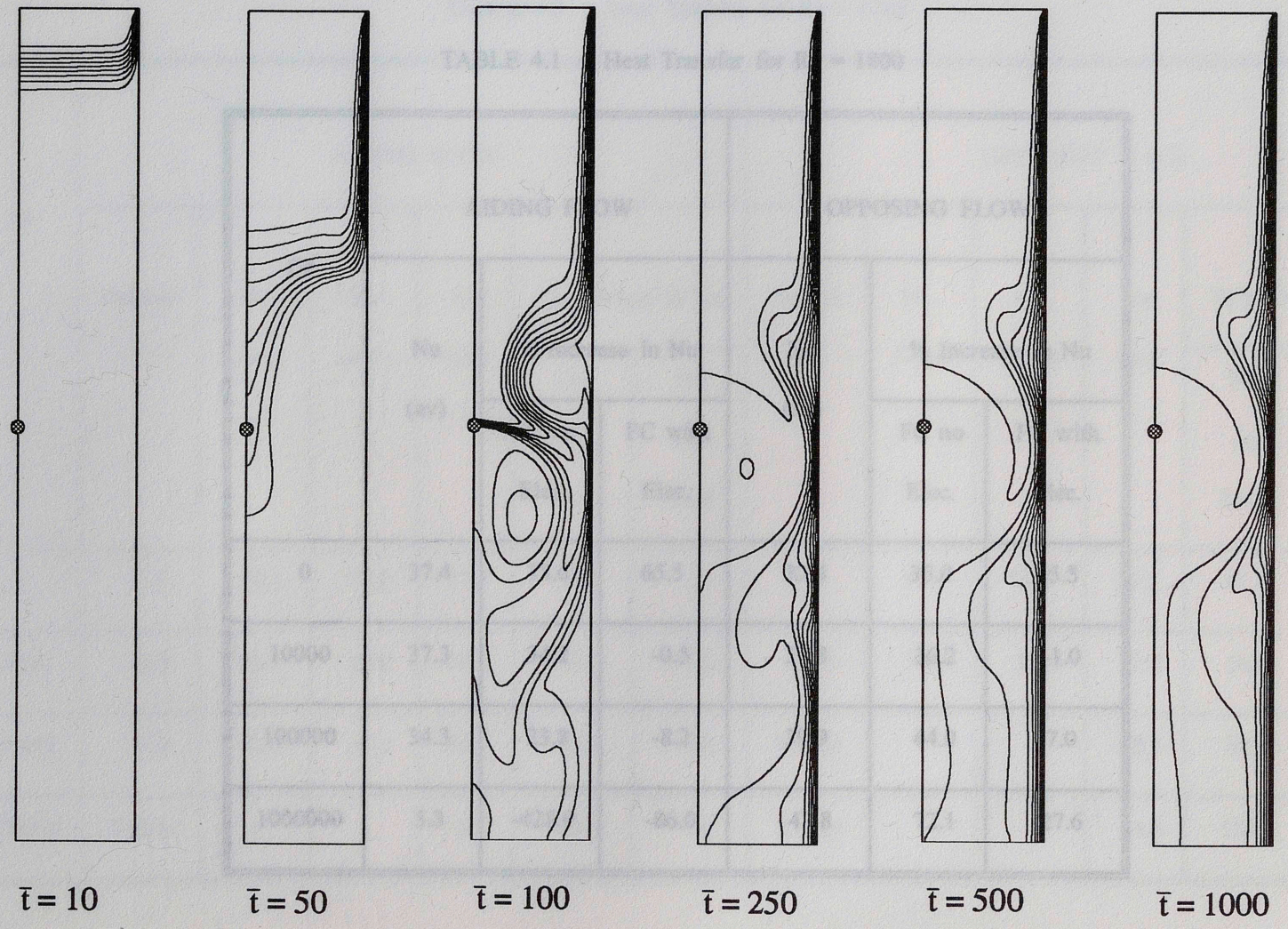

Figure 4.33b Development of Temperature Field - Opposing Flow

Re=600 $Gr=10^6$

TABLE 4.1 : Heat Transfer for Re = 1800

Gr	AIDING FLOW			OPPOSING FLOW		
	Nu (av)	% Increase in Nu		Nu (av)	% Increase in Nu	
		FC no Elec.	FC with Elec.		FC no Elec.	FC with Elec.
0	37.4	35.0	65.5	37.4	35.0	65.5
10000	37.3	34.2	-0.5	37.8	36.2	-1.0
100000	34.3	23.8	-8.2	39.9	44.0	7.0
1000000	5.3	-428.0	-86.0	47.8	72.1	27.6

$\overline{Nu}$ for Forced Convection without Electric Field = 27.7

TABLE 4.2 : Heat Transfer for Re = 1200

Gr	AIDING FLOW						OPPOSING FLOW					
	Period	Nu (max)	Nu (min)	Nu (av)	% Increase in Nu		Period	Nu (max)	Nu (min)	Nu (av)	% Increase in Nu	
					FC no Elec.	FC with Elec					FC no Elec.	FC with Elec.
0	33.5	38.3	36.9	37.5	55.1	-	33.5	38.3	36.9	37.5	55.1	-
10000	33.5	66.1	64.0	65.0	53.5	-1.0	33.5	38.3	37.3	37.8	56.0	0.5
100000	34.0	61.0	59.0	60.1	42.0	-9.0	Steady	-	-	40.6	68.0	8.2
1000000	Steady	-	-	6.3	-85.0	-9.0	Steady	-	-	53.4	121.0	42.0

$\overline{Nu}$ for Forced Convection without Electric Field = 24.2

TABLE 4.3 : Heat Transfer for Re = 600

Gr	AIDING FLOW						OPPOSING FLOW					
	Period	Nu (max)	Nu (min)	Nu (av)	% Increase in Nu		Period	Nu (max)	Nu (min)	Nu (av)	% Increase in Nu	
					FC no Elec.	FC with Elec.					FC no Elec.	FC with Elec.
0	38.5	57.2	44.2	50.1	168.0	-	38.5	57.2	44.2	50.1	168.0	-
10000	38.5	57.8	44.6	51.0	173.0	2.0	38.5	57.1	44.1	49.4	165.0	-1.3
100000	79.5	71.1	40.3	54.5	192.0	9.0	Steady	-	-	42.8	130.0	-1.4
1000000	None	-	-	8.6	-54.0	-83.0	Steady	-	-	51.5	176.0	2.8

$\overline{Nu}$ for Forced Convection without Electric Field = 21.7

CHAPTER 5

CONCLUSIONS

Numerical study has been carried out to examine the effect of electrostatic field on mixed convection in a single-wire vertical channel. Following are the major conclusions emerging from the present study.

1. The results obtained from Yamamoto's and Kallio's model agree well with each other for the prediction of electrostatic field and space charge density distribution in one-wire and two-wire channels. A close examination on the Kallio's results, however, shows that the distribution of E_x and E_y in the channel is not symmetrical. Hence Yamamoto's model is adopted for the solution of electrostatic field and charge density distribution, which are then used in the calculation of the body force term in the flow equations.
2. For simultaneously developing flows, a single-wire channel in the transient mixed convection analysis shows that the flow transition will lead to either a steady-state or a periodic oscillation for both aiding and opposing flows.
3. An enhancement of 130% to 170% in heat transfer is observed for the case of forced convection due to the presence of electric field. The increase in the Reynolds number show a declination in the heat transfer enhancement due to the suppression of the secondary flow.

4 For aiding flows at Re = 600, heat transfer increases with the thermal buoyancy while it decreases with the thermal buoyancy when Re = 1200 and 1800. A reduction in heat transfer is due to the expansion of the secondary flow region, which significantly minimize the contact area between the primary flow and the wall.

5 Oscillation in the flow field is observed for aiding flows at Re = 600 and 1200. For Re = 1800 no oscillation is noticed. The period of average Nusselt number gradually increases with an increase in the thermal buoyancy. For Re = 1200, the flow field restabilizes at Gr = 10^6.

6. For opposing flows, heat transfer is increased for all flow and buoyancy strength considered. Except for Re = 600, the heat transfer increases consistently with an increase in the thermal buoyancy since the secondary flow is suppressed which allows more contact between the primary flow and the wall.

7. For opposing flows, the thermal buoyancy seems to play a major role in the suppression of flow oscillation for lower Reynolds number flows. The flow field stabilizes with an increase in the Grashoff number.

8. The flow field reaches a steady state in short time for opposing flows as compared to that for aiding flows at a high Grashoff number (Gr = 10^6).

9. It is observed that $\overline{Nu}$ for opposing flow remains approximately constant with respect to the mixed convection parameter Gr/Re^2. However, the trend is observed only at lower values of Gr/Re^2 (less than 1.0) for aiding flows.

Due to the domination of the inertial forces, the mixed convection heat transfer in opposing flows remains unchanged as it approaches the forced convection asymptote. This is true for aiding flows only at higher Re numbers indicating the transition from mixed convection to forced convection. This is shown in Figs. 5.1 a and b.

In summary, the present results show that, for opposing flows, an increase in heat transfer is possible with the application of electrostatic field. The heat transfer increases with the thermal buoyancy, i.e., the Grashoff number. Although aiding flows also show an increase in the heat transfer for flows at Re = 600, the heat transfer is actually reduced for flows at Re = 1200 and 1800, especially at a higher Grashoff number ($Gr = 10^6$). The dramatical reduction in heat transfer is believed to be a combined effect resulted from the thermal buoyancy and electric body force. The mechanism involved in this complicated interaction is still not clear at this time and await further investigation.

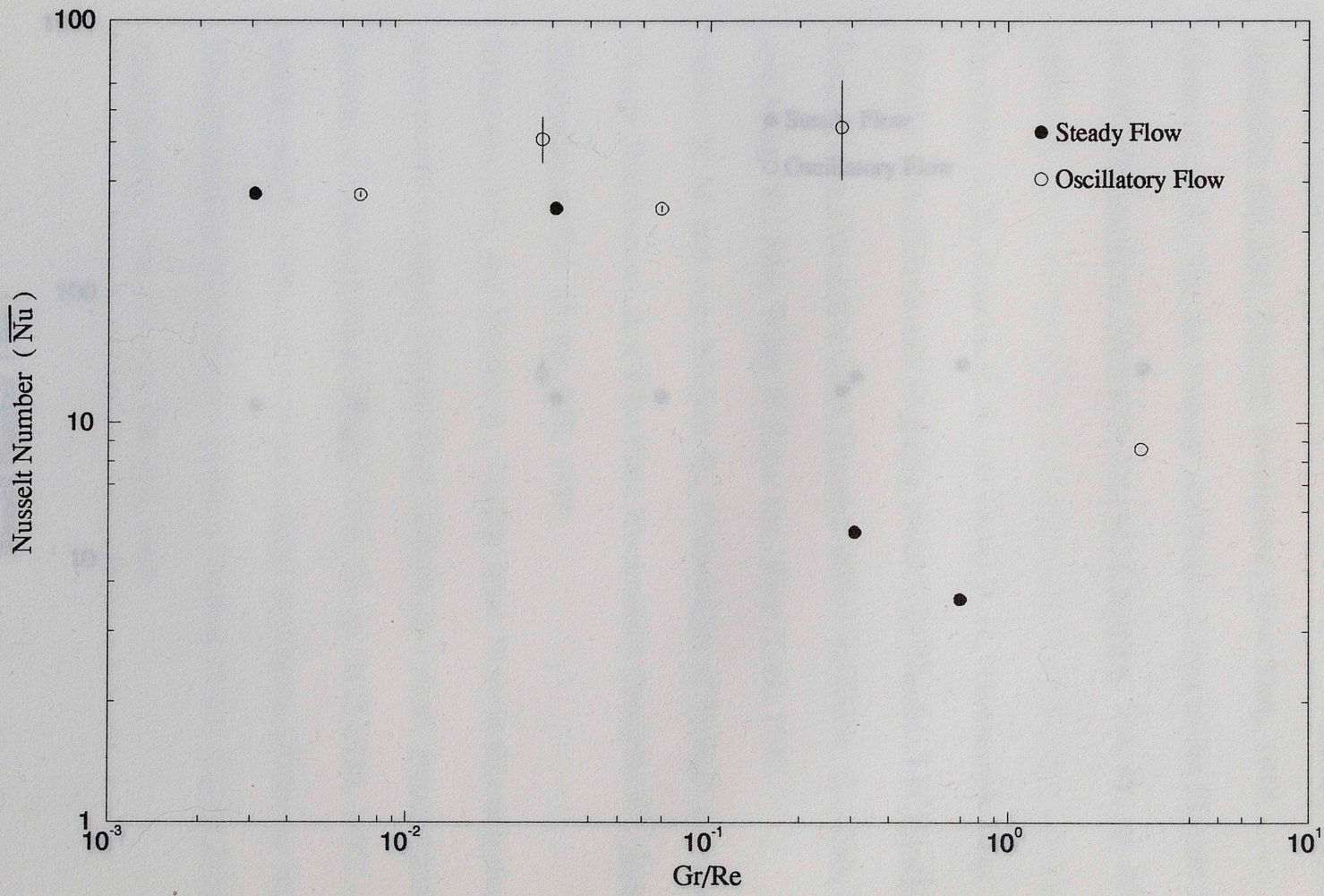

Figure 5.1a Variation of Average Nusselt Number with Gr/Re^2 - Aiding Flow

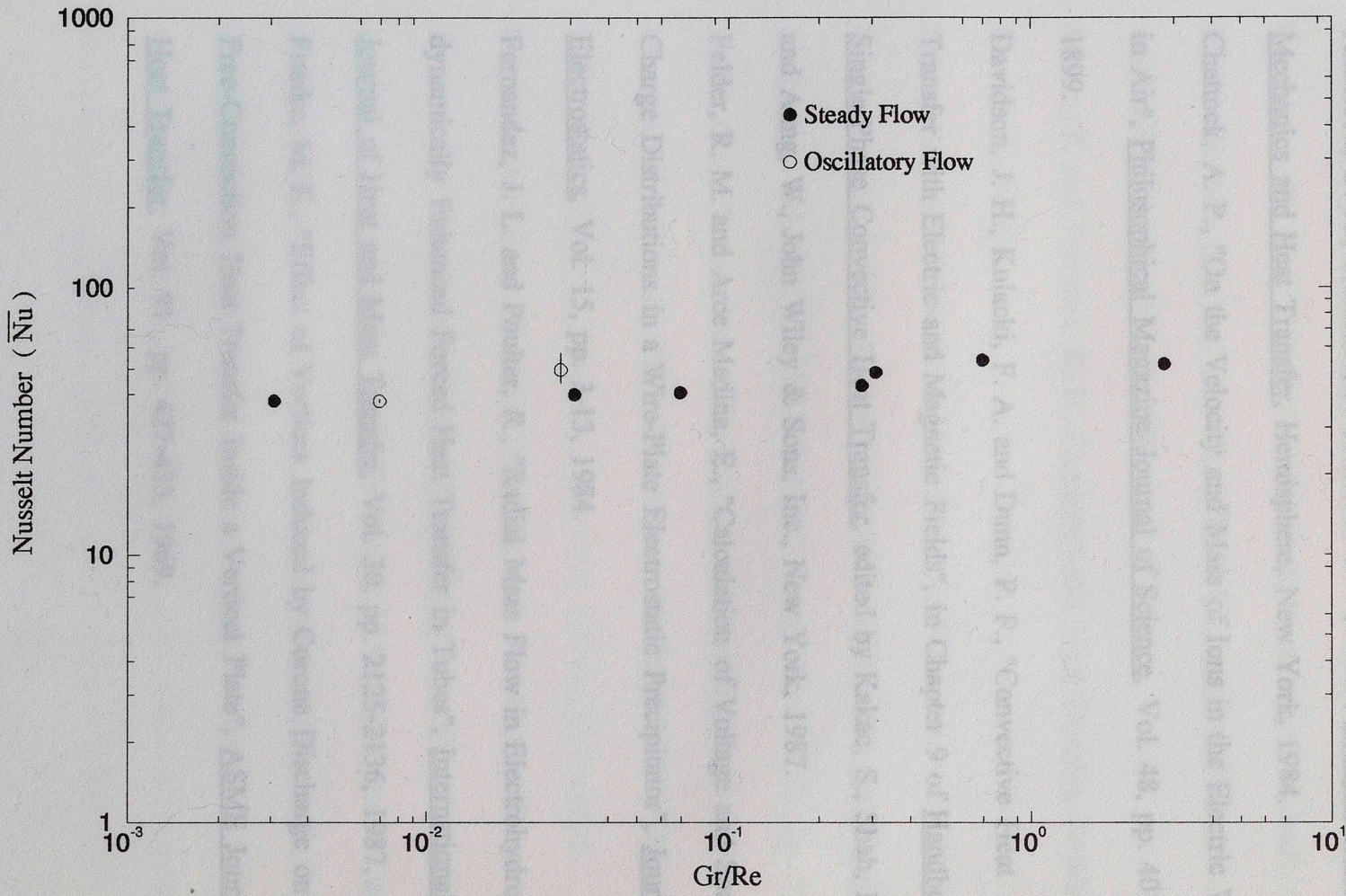

Figure 5.1b Variation of Average Nusselt Number with Gr/Re^2 - Opposing Flow

REFERENCES

1 Anderson, D. A., Tannehill, J. C. and Pletcher, R. H., Computational Fluid Mechanics and Heat Transfer, Hemisphere, New York, 1984.

2 Chattock, A. P., "On the Velocity and Mass of Ions in the Electric Wind in Air", Philosophical Magazine Journal of Science, Vol. 48, pp. 401-402, 1899.

3 Davidson, J. H., Kulacki, F. A. and Dunn, P. F., "Convective Heat Transfer with Electric and Magnetic Fields", in Chapter 9 of Handbook of Single-Phase Convective Heat Transfer, edited by Kakac, S., Shah, R. K. and Aung, W., John Wiley & Sons, Inc., New York, 1987.

4 Felder, R. M. and Arce Medina, E., "Calculation of Voltage and Space Charge Distributions in a Wire-Plate Electrostatic Precipitator", Journal of Electrostatics, Vol. 15, pp. 3-13, 1984.

5 Fernandez, J. L. and Poulter, R., "Radial Mass Flow in Electrohydrodynamically Enhanced Forced Heat Transfer in Tubes", International Journal of Heat and Mass Transfer, Vol. 30, pp. 2125-2136, 1987.

6 Franke, M. E., "Effect of Vortices Induced by Corona Discharge on the Free-Convection Heat Transfer Inside a Vertical Plate", ASME Journal of Heat Transfer, Vol. 91 , pp. 427-433, 1969.

7 Fujino, T., Yokoyama, Y. and Mori, Y. H., "Augmentation of Laminar Forced-Convection Heat Transfer by the Application of a Transverse Electric Field", Journal of Heat Transfer, Vol. 111, pp. 345-351, 1988.

8 Gosman, A. D., Pun, W. M., Runcahl, A. K., Spalding, D. B. and Wolfshtein, M., Heat and Mass Transfer in Recirculating Flows, Academic Press, New York, 1969.

9 Jaluria, Y. and Torrance, K. E., Computational Heat Transfer, Hemisphere, New York, 1986.

10 Kallio, G. A. and Stock, D. E., "Interaction of Electrostatic and Fluid Dynamic Fields in Wire-Plate Electrostatic Precipitators", Journal of Fluid Mechanics, Vol. 240, pp. 133-166, 1992.

11 Kallio, G. A. "Interaction of Electrostatic and Fluid Dynamic Fields in Wire-plate Precipitator", Ph.D. Dissertation, Washington State University, 1987.

12 Lai, F. C., McKinney, P. J. and Davidson, J. H.,"Oscillatory Electrohydrodynamic Gas Flows", ASME Journal of Fluids Engineering (in press).

13 Lawless, P. A. and Sparks, L. E., "Prediction of Voltage-Current Curves for Novel Electrodes", Proceedings of the 6th Symposium on the Transfer and Utilization of Particulate Control Technology, Kansas City, MO, pp. 4.4-4.14, 1984.

14 Leonard, G. L., Mitchner, M. and Self, S. A., "An Experimental Study of the Electrohydrodynamic Flow in Electrostatic Precipitators", Journal of Fluid Mechanics, Vol. 127, pp. 123-140, 1983.

15 Leutert, G. and Bohlen, B., "The Spatial Trend of Electric Field Strength and Space Charge Density in Plate Type Electrostatic Precipitator", Staub-Reinhalt, Luft., Vol. 32, pp. 27-33, 1972.

16 McDonald, J. R. ,"A Mathematical Model of Electrostatic Precipitation", US Environmental Protection Agency Report, EPA-500/7-78/111A, Vol. 1, 1978.

17 McKinney, P. J., " Electrohydrodynamic Flow in a Barbed Plate Electrostatic Precipitator", M.S. Thesis, Colorado State University, 1988.

18 Patankar, S. V., Numerical Heat Transfer and Fluid Flow, Hemisphere, New York, 1980.

19 Peek, F. W., Dielectric Phenomenon in High Voltage Engineering, McGraw-Hill, New York, 1966.

20 Ramadan, O. E. and Soo, S. L., "Electrohydrodynamic Secondary Flow", Physics of Fluids, Vol. 12, pp. 1943-1945, 1959.

21 Roache, P. J., Computational Fluid Dynamics, Hermosa Publishers, Albuquerque, N.M., 1976.

22 Robinson, M., "A Modified Deutsch Efficiency Equation of Electrostatic Precipitation", Atmospheric Environment, Vol. 1, pp. 193-204, 1967.

23 Sadek, S. E., Fax, R. G. and Hurwitz, M., "The Influence of Electric Fields on Convective Heat and Mass Transfer from a Horizontal Surface under Forced Convection", Journal of Heat Transfer, Vol. 94, pp. 144-148, 1972.

24 Shah, R. K. and London, A. L., "Laminar Flow Forced Convection in Ducts", Supplement 1 to Advances in Heat Transfer, Academic Press, New York, 1978.

25 Stock, D. E. and Crowe, C. T., "The Effect of Electrohydrodynamic Secondary Flow in the Performance of Electrostatic Precipitators", Proceedings 1974 Heat transfer and Fluid Mechanics Institute Meeting, Stanford University Press, pp. 254-265, 1974.

26 Takimoto, A., Tada, Y. and Hayashi, Y., "Convective Heat Transfer Enhancement by a Corona Discharge", Heat Transfer - Japanese Research, Vol. 20, pp. 18-35, 1991.

27 Velkoff, H. R. and Miller, J. H., "Condensation of Vapor on a Vertical Plate with a Transverse Electrostatic Field", Journal of Heat Transfer, Vol. 87, pp. 197-201, 1965.

28 Webb, R. L., "Enhancement of Single Phase Heat Transfer", in Chapter 1 of Handbook of Single-Phase Convective Heat Transfer, edited by Kakac, S., Shah, R. K. and Aung, W., John Wiley & Sons, Inc., New York, 1987.

29 Yabe, A., Mori, Y. and Hijikata, K., "EHD Study of the Corona Wind between Wire and Plate Electrodes", AIAA Journal, Vol. 4, pp. 340-345, 1978.

30 Yamamoto, T., "Electrohydrodynamic Secondary Flow Interaction in an Electrostatic Precipitator", Ph.D. Dissertation, Ohio State University, 1979.

31 Yamamoto, T. and Velkoff, H. R., "Electrohydrodynamics in an Electrostatic Precipitators", Journal of Fluid Mechanics, Vol. 108, pp. 1-8, 1981.

This volume is the property of the University of Oklahoma, but the literary rights of the author are a separate property and must be respected. Passages must not be copied or closely paraphrased without the previous written consent of the author. If the reader obtains any assistance from this volume, he must give proper credit in his own work.

I grant the University of Oklahoma Libraries permission to make a copy of my thesis upon the request of individuals or libraries. This permission is granted with the understanding that a copy will be provided for research purposes only, and that requestors will be informed of these restrictions.

[redacted]

A library which borrows this thesis for use by its patrons is expected to secure the signature of each user.

This thesis by _____ has been used by the following persons, whose signatures attest their acceptance of the above restrictions.

NAME AND ADDRESS	DATE

OU–138